Department of Pure and Applied Chemistry

RAMAN SPECTROSCOPY AND DIP-PEN NANOLITHOGRAPHY FOR DETECTION AND CONTROL OF BIOLOGICAL INTERACTIONS

by

Stacey Laing

A thesis submitted to the Department of Pure and Applied Chemistry, University of Strathclyde, in fulfilment of the regulations for the degree of Doctor of Philosophy.

2013

This thesis is the result of the author’s original research. It has been composed by the author and has not been previously submitted for examination which has led to the award of a degree.

Signed:
Date:

Acknowledgments

I would like to take this opportunity to thank Professor Duncan Graham and Dr. Karen Faulds for their supervision, advice and for the opportunity to be a part of their group.

For the helpful discussions, I would like to thank Professor Ewen Smith. I would also like to say a huge thank you to Dr. Aaron Hernandez-Santana and Dr. Eleanore Irvine for their technical support and helpful advice which was invaluable throughout my project; to Kristy for the lengthy chats, both work-related and non-, and to the rest of the Ramanators for the helpful input and for the fun times.

To Dr. Raffaella Suriano, thanks for a great collaboration, your help and advice has been excellent and it's been an absolute pleasure working with you.

Thanks to Dr. Dimitrios Lamprou for his help in providing the liquid AFM, Dr. Laura McNamara for carrying out the cell experiments, Dr. Samuel Mabbott for the data analysis, to Dr. Darren Lee Asquith for supplying the blood serum samples and Dr. Jörg Saβmannshausen for carrying out the Raman calculations.

Finally, a special thanks to my friends and family mostly for just being there and for their understanding, especially my best friend and big sis' who's always so proud, and Kevin for surviving the emotional rollercoaster and helping me through the tough times. The biggest thank you of all is to my mum and dad for their support and encouragement in everything I do, for pushing me in the right direction, and for always believing in me.

Abstract

The ability to monitor, control and manipulate the behaviour of biomolecules is invaluable for the understanding of biological processes. Sensitive and high-throughput detection of proteins in biological fluids can allow the development of biomarkers for early disease diagnosis, an understanding of disease processes, and improvement in drug development. Furthermore, the ability to control cellular interactions on a surface can be applied for the development of medical devices and technology.

The research presented herein shows that by introducing resonance Raman scattering (RRS) as the detection method in a conventional enzyme-linked immunosorbent assay (ELISA), we can detect biomarkers with a detection limit up to fifty times lower than that of the traditional colorimetric detection. Human blood serum samples were analysed using this method, proving that it would be suitable for use in a clinical environment. The detection method is also easily applied to alternative ELISA systems and for the detection of any number of target analytes.

Dip-pen nanolithography (DPN) was used to fabricate prostate-specific antigen (PSA) immunoassay arrays with low end micron scale feature sizes, which were subsequently detected using RRS. The combination of the advantages of DPN with the RRS detection method introduces a sensitive, robust and high-throughput platform for the detection of biomarkers, which should be easily developed into a multiple target assay.

For the control of cellular interactions, polymer arrays were fabricated which were shown to undergo changes in response to varying temperature. Characterisation of the thermoresponsive substrates by atomic force microscopy (AFM) and Raman scattering showed changes in the topography and hydration state, respectively. Preliminary cell experiments indicated that the surfaces were biocompatible and that the behaviour of cells could potentially be controlled by altering properties of the arrays.

Overall, this thesis highlights the strengths of Raman spectroscopy and DPN, individually and as complementary techniques, for use in biomedical applications.

Abbreviations

2D PAGE - two-dimensional polyacrylamide gel electrophoresis
ABTS - 2,2′-azino-bis-(3-ethylbenzthiazoline-6-sulfonic acid)
AFM - atomic force microscopy
ALP - alkaline phosphatase
ATRP - atom transfer radical polymerisation
BPH - benign prostate hyperplasia
BSA - bovine serum albumin
BSA-NHS - BSA-*N*-hydroxysuccinimide
CCD - charge coupled device
CDR - complementarity determining regions
CTC - charge transfer complex
DAPI - 4′,6-diamidino-2-phenylindole
dddH$_2$O - doubly distilled deionised water
DEAAm - N, N-diethylacrylamide
DMARD - disease-modifying anti-rheumatic drugs
DNA - deoxyribonucleic acid
DPN - dip-pen nanolithography
DT - dwell time
ECM - extracellular matrix
E-DPN - electrochemical dip-pen nanolithography
ELISA - enzyme-linked immunosorbent assay
ELP - elastin-like polypeptide
EPC - endothelial progenitor cells
F$_{ab}$ - antibody binding fragment
FBS - foetal bovine serum
F$_c$ - crystallisable fragment
FITC - fluorescein isothiocyanate
GPTMS - (3-glycidyloxypropyl)trimethoxysilane
HIV - human immunodeficiency virus

HRP	- horseradish peroxidase
Ig	- immunoglobins
IL-6	- interleukin-6
IPA	- *iso*-propyl alcohol
ITS	- insulin-transferrin-selenium
Jeff	- Jeffamine ED-600
Jeff/DEAAm	- Jeffamine ED-600/N,N-Diethylacrylamide
KHD	- Kramer Heisenberg Dirac
LCST	- lower critical solution temperature
LOD	- limit of detection
MHA	- 16-mercaptohexadecanoic acid
MPTMS	- (3-mercaptopropyl)trimethoxysilane
MS	- mass spectrometry
MSC	- mesenchymal stem cell
NIL	- nanoimprint lithography
NIPAAm	- N-isopropylacrylamide
NLP	- nanolithography platform
ODT	- 1-octadecanethiol
OPD	- o-phenylenediamine
PAP	- prostatic acid phosphatase
PAPP	- *p*-aminophenyl phosphate
PBS	- phosphate buffered saline
PCR	- polymerase chain reaction
PECAM-1	- platelet/endothelial cell adhesion molecule-1
PEG-DMA	- poly(ethylene glycol) dimethacrylate
PNIPAAm	- poly(N-isopropylacrylamide)
PSA	- prostate specific antigen
RA	- rheumatoid arthritis
RRS	- resonance Raman scattering
RS	- Raman scattering
RT	- room temperature

SAM	- self-assembled monolayer
SDS	- sodium dodecyl sulfate
SERRS	- surface enhanced resonance Raman scattering
SERS	- surface enhanced Raman scattering
SIPGP	- self-initiated photografting and photopolymersation
SPR	- surface plasmon resonance
SPRi	- surface plasmon resonance imaging
STM	- scanning tunnelling microscopy
TACE	- TNF-α-converting enzyme
TCPS	- tissue culture polystyrene
tDPN	- thermal dip-pen nanolithography
TMB	- 3,3′,5,5′-tetramethylbenzidine
TMSPM	- 3-(trimethoxysilyl)propyl methacrylate
TNF-α	- tumour necrosis factor alpha
TRITC	- tetramethyl rhodamine isothiocyanate
UCST	- upper critical solution temperature
UV	- ultraviolet
UV/Vis	- ultraviolet/visible
v/v	- volume by volume
VEcad	- vascular endothelial cadherin
w.r.t	- with respect to
w/v	- weight by volume
μCP	- microcontact printing

Contents

Acknowledgments **i**

Abstract **ii**

Abbreviations **iii**

1. General Introduction **1**

1.1 Introduction to Proteomics 1
  1.1.1 Protein Structure and Function 2
  1.1.2 Protein Interactions 5
  1.1.3 Protein Biomarkers 6
  1.1.4 Immunoassays 7
1.2 Surface Patterns for Detection and Control of Biomolecules 11
  1.2.1 Surface Patterning for Protein Applications 11
  1.2.2 Surface Patterning for Cellular Interactions 13
  1.2.3 Patterning Methods for Biomolecular Control 14
1.3 Dip-Pen Nanolithography 16
  1.3.1 Basic Concept 16
  1.3.2 DPN Process Development 18
  1.3.3 Applications of DPN 19
1.4 Techniques for Biomolecule Detection 22
  1.4.1 Label-Free Detection 23
  1.4.2 Label-Dependent Methods 24
1.5 Raman Spectroscopy 26
  1.5.1 Raman Scattering (RS) 26
  1.5.2 Resonance Raman Scattering (RRS) 28
  1.5.3 Surface Enhanced Raman Scattering (SERS) 30
  1.5.4 Surface Enhanced Resonance Raman Scattering (SERRS) 31
  1.5.5 Raman Mapping 32
1.6 Project Aims 33

2. Experimental **35**

2.1 Development of a Resonance Raman ELISA 35
  2.1.1 Materials and Instrumentation 35
  2.1.2 Monitoring the Reaction over Time by UV/Vis Spectroscopy 36
  2.1.3 Studying Spectral Changes using Raman Spectroscopy 37
  2.1.4 Quantification of TNF-α by Resonance Raman Spectroscopy 38
  2.1.5 Quantification of PSA by a Resonance Raman ELISA 39
  2.1.6 Further Enhancement by SERRS 40
2.2 PSA Immunoassay Arrays with RRS Detection 41
  2.2.1 Materials and Instrumentation 41
  2.2.2 Bulk Spotting Capture Antibody 42
  2.2.3 Fabrication of PSA Capture Antibody Arrays 42
  2.2.4 PSA Immunoassay 43
  2.2.5 Detection by RRS 44
2.3 Thermoresponsive Polymer Arrays 44
  2.3.1 Materials and Instrumentation 44

2.3.2 Preparation of Surfaces 46
2.3.3 Fabrication of Polymer Arrays 46
2.3.4 Characterisation of Polymer Arrays 47
2.3.5 Analysis of Cellular Interactions 48

3. Detection of Protein Biomarkers using a Resonance Raman ELISA 50
3.1 Introduction 50
3.1.1 ELISAs for Biomarker Detection 50
3.2 HRP Catalysed Oxidation of TMB in Solution 53
3.2.1 Monitoring the Reaction by UV/Visible Absorption Spectroscopy 53
3.2.2 Resonance Raman Study of TMB Oxidation 55
3.3 Quantification of TNF-α by Resonance Raman Spectroscopy 57
3.3.1 Analysis of Human Blood Samples 64
3.3.2 Further Enhancement by SERRS 66
3.4 Adaptability of the Detection Method for Alternative ELISAs 67
3.4.1 Detection of Prostate-Specific Antigen by a Resonance Raman ELISA 68
3.4.2 Detection Using Alternative Chromogenic Substrates 71
3.5 Concluding Remarks 75

4. Immunoassay Arrays Fabricated by Dip-Pen Nanolithography 76
4.1 Introduction 76
4.2 Selection of a Suitable Surface for Immunoassay Arrays 77
4.2.1 Epoxysilane Coated Glass 78
4.2.2 3D Nitrocellulose Substrates 84
4.2.3 Nitrocellulose PATH® Slides 87
4.3 Quantification of PSA using Immunoassay Arrays with RRS Detection 89
4.4 Concluding Remarks 93

5. Thermoresponsive Polymer Arrays for Potential Control of Cellular Interactions 95
5.1 Introduction 95
5.1.1 Thermoresponsive Polymer Hydrogels 95
5.1.2 Applications of Thermoresponsive Polymers 97
5.1.3 Thermoresponsive Polymer Patterns 99
5.2 Fabrication of Thermoresponsive Polymer Arrays 100
5.2.1 Poly(N-isopropylacrylamide) 100
5.2.2. N,N-Diethylacrylamide 105
5.2.3 Jeffamine ED-600 109
5.2.4 Mixed System: Jeffamine ED-600 and N,N-Diethylacrylamide 113
5.3 Characterisation of Thermoresponsive Behaviour 118
5.4 Control of Cellular Interactions 122
5.5 Concluding Remarks 126

6. Conclusions 128

7. References 130

8. Appendix: Publications 144

1. General Introduction

1.1 Introduction to Proteomics

In order to understand biological processes, such as those associated with disease, it is essential to understand the functional network of the cell. Such elucidation is best gained at the protein level which has led to the concept of the proteome and the relatively new field of proteomics. Proteome was a term introduced by Mark Wilkins, initially at a conference[1] and subsequently in publications,[2-3] to describe the protein complement of the genome; or the total proteins expressed in a cell, tissue or organism. Since then proteomics has become a field of vast interest and consequently much publication.

Where nucleic acids vary little in their physicochemical properties and are easily recognisable through complementary base pairing, proteins are much more diverse and undergo complex biochemical modifications. The concentration of proteins is usually very low and, contrary to deoxyribonucleic acid (DNA) analysis, amplification techniques such as the polymerase chain reaction (PCR) do not exist. This, as well as the vast number of proteins, their network functioning and their dynamic nature, makes the study of the proteome much more challenging than its gene equivalent. However, without the previous achievements of genomics, proteomics would not be possible.[4]

The main areas of interest in proteomics are the identification of proteins in cells, tissues, sub-cellular protein complexes and biological samples; their expression as a function of a particular state; the interaction of proteins with each other and with other molecules to control processes; and the identification of how proteins are modified and how these modifications affect other proteins.[5]

On attainment of such knowledge and understanding, many important applications arise, some of which have sparked great medical interest. For example, the development of novel biomarkers for diagnosis and early disease detection, identification of new medical targets, and improved drug development through better understanding of disease mechanisms.[6] Accordingly, many new techniques and technologies have emerged to aid proteomic research.

Early proteomics relied heavily on two-dimensional polyacrylamide gel electrophoresis (2D PAGE) and mass spectrometry for the profiling of protein expression. Although the methods had their limitations, 2D PAGE was utilised for important profiling of disease tissues and was successful in, for example, the classification of leukaemias into their sub-types.[7] It was also used with mass spectrometry to identify disease related changes in the study of heart disease.[8]

Over the years since the introduction of proteomics, mass spectrometry has undergone astonishing advances and has yielded abundant information about individual proteins. However, the long term hope is to gain an understanding of complete biological systems by studying how proteins interact with each other, as well as with non-protein molecules, to control processes within cells, tissues and even whole organisms. This has led to the evolution of more sensitive and high-throughput technologies that can enable a thorough appreciation of the dynamic proteome by providing snap shots of cellular responses.[4]

1.1.1 Protein Structure and Function[9,10]

Proteins are macromolecular polymers composed of amino acids linked by peptide bonds. Making up more than 50% of the dry weight of most cells, they are active in almost everything an organism does. Many different types of protein exist, each with a specific biological function. Some examples of these are:

- Structural proteins such as keratin in hair and skin;

- Storage proteins like casein in milk which stores the amino acids required for baby mammals;
- Transport proteins, for instance haemoglobin that transports oxygen around the body;
- Hormones which regulate processes e.g. insulin;
- Contractile proteins i.e. actin and myosin which are responsible for muscle movement;
- Defensive proteins such as antibodies which protect against disease;
- Enzymes which regulate metabolism by selectively catalysing chemical reactions.

This diverse functionality depends on the unique three-dimensional (3D) shape and the amino acid conformation of each protein. Consequently, they are the most structurally sophisticated molecules known. The structure of proteins can be thought of in four main levels: primary, secondary, tertiary and quaternary; each level reflecting the complexity of the interactions involved in determining the unique structure.

The primary structure is the linear sequence of amino acids in the peptide chain. The polypeptide chains are formed via a condensation reaction between the amino groups and carboxyl groups of individual amino acids (Figure 1.1). Each of the 20 amino acids has varying properties which depend on the nature of the side group, R. The amino acid sequence determines the higher levels of molecular structure and thus a single change in the sequence can have an extreme effect on the overall biological structure and function of the protein.

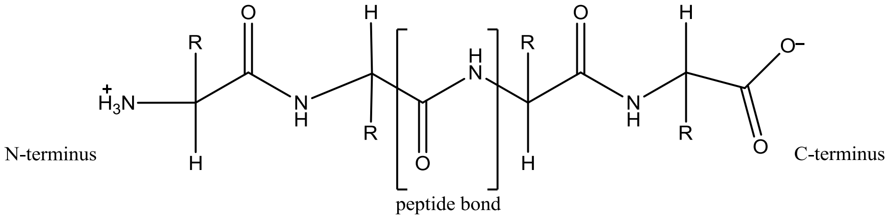

Figure 1.1. *A polypeptide chain with repeating peptide bonds connecting amino acids to form the unique primary structure of a protein.*

The secondary structure arises from the hydrogen-bond stabilised interactions between peptide carbonyl oxygens and amide hydrogens along the polymer backbone (Figure 1.2). These interactions lead to stabilisation of structures such as α-helices and β-sheets, first described by Pauling and Corey in a series of pioneering revelations.[11-12]

In an α-helix, the backbone adopts a coiled structure similar to that of DNA. In a β-sheet however, the backbone has a linear structure where the polypeptide chains lay either parallel or anti-parallel to one another in a pleated arrangement. In this conformation, as opposed to that of the α-helix, the plane formed by the hydrogen bonds is perpendicular to the plane of the sheet.

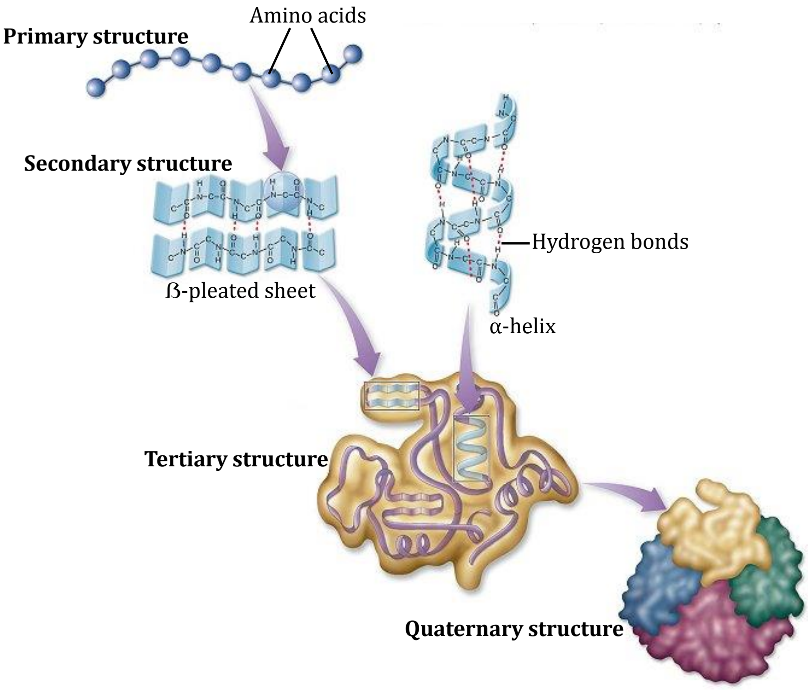

Figure 1.2. *The primary, secondary, tertiary and quaternary structure within a protein.*[13]

The tertiary structure describes the association between different portions of the protein to give it a unique 3D conformation. It describes how, for example, the α-helices and β-sheets fold in relation to one another and is stabilised by forces such as ionic bonds, hydrogen bonds and hydrophobic interactions.

These interactions, though weak, accumulate to give the protein a specific shape. This is further reinforced by strong, covalent disulfide bridges which constrain the movement of the molecule (Figure 1.3).

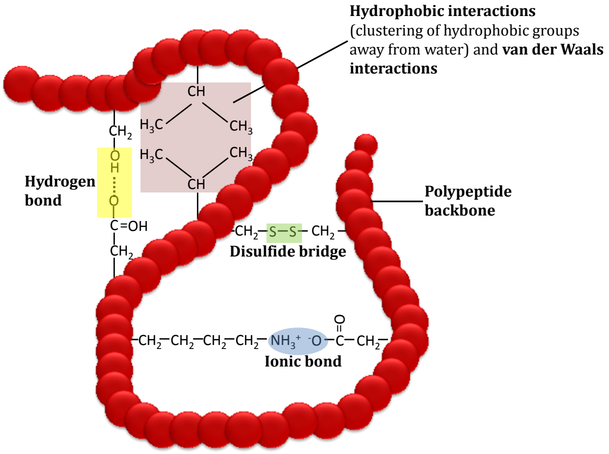

Figure 1.3. *The bonding contributions to the tertiary structure of a protein.*

The quaternary structure is defined by the non-covalent association between more than one polypeptide chain to form a functional macromolecule, in which the individual subunits may or may not be active when dissociated from the larger unit. The quaternary structure of proteins supports their biological function; for example, proteins such as collagen are fibrous and proteins like haemoglobin exhibit a globular structure.

With such specific 3D structures linking inextricably to their functions, proteins can become denatured upon change in their environmental conditions. Such change in surroundings causes a change in the secondary and tertiary structure of the protein into a less ordered arrangement, which subsequently renders the protein biologically inactive.

1.1.2 Protein Interactions

Not only do proteins exhibit distinct structures but they also work in functional networks rather than as individual units. It is therefore vital in studying the macromolecules, not only to gain an understanding in their structures, but also on how they interact with one another as well as with other molecules during cellular processes. Detection of such protein interactions aids the understanding of disease expression and progression thus providing a means for early detection and consequent treatment of certain conditions.

Furthermore, an understanding of how biomolecules and cells interact at solid interfaces can allow their behaviour to be controlled which is an appealing prospect for a range of applications from biosensing to drug delivery and tissue engineering.[14]

When studying the interaction of molecules with a surface, it is important to consider the properties of the molecules which will influence these interactions. For proteins, these properties are the size and structure and ultimately the sequence of amino acids. Aside from covalent bonding via end functional groups, the main interactions of proteins at a surface are hydrophobic and electrostatic interactions arising from the polar/non-polar and anionic/cationic properties of the amino acids. The relative strength of the contributions depend on the properties of the surface, the type of protein and surrounding conditions such as pH and salt concentration.[14]

Protein interactions are fundamental to a wide variety of biological processes; as such, an understanding of these interactions is of interest for a variety of medical applications including the discovery and detection of biomarkers for the diagnosis and treatment of disease.

1.1.3 Protein Biomarkers

A biomarker is a measurable ‘biological marker’ that correlates with a specific outcome or state, particularly one relevant to the risk of contraction, the presence, or the stage of a disease.[15] Biomarkers of various types can be used in a clinical situation to detect, diagnose or monitor the progression of a particular disease state and thus to guide treatment or to observe the therapeutic response.

The proteomic focus on discovery and development of biomarkers is largely due to the ubiquitous role of proteins in disease. Being most often affected by disease, protein molecules form the basis of most drug targets and therefore the promise for biomarkers lies largely in the protein domain.

Some biomarkers are particularly suitable for detection as part of multiple target assays. For example, cytokines and chemokines, or chemotactic cytokines, are structurally similar proteins which share overlapping functions. They form part of a complex regulatory network within the innate immune system and are secreted during inflammatory responses. During such response, the chemokines function as regulatory molecules attracting leucocytes to the site of inflammation, whilst cytokines regulate the production of other inflammatory mediators.[16] Due to the incorporation of the immune system with other physiological systems such as the cardiovascular and gastrointestinal systems, cytokines often act as a signalling system throughout the body making them an ideal biomarker candidate for the diagnosis and understanding of disease.[17]

1.1.4 Immunoassays

Immunoassays are a fast-growing and widely utilised analytical technique for the detection and quantification of biomarkers. Since the first clinical use in 1959 for the detection of insulin in blood,[18] immunoassays have undergone major advances and are now a commonplace method in hospitals, medical laboratories and research facilities. This can be owed to the simplicity, specificity and high-throughput of the technique. Data generated using immunoassays allows for the identification and evaluation of disease progression and thus shortened hospital stays and improved treatment.

The basis of an immunoassay is that a measurable signal can be generated as a result of specific binding between an antibody and an antigen. By incorporating a label, immunoassays make use of the specificity and high affinity reactions of antibodies to detect and quantify specific biomarkers.

In an immune response, immunogens trigger the production of antibodies which they subsequently bind to in a specific manner to provide recovery from infection, immunity to possible subsequent infection, and susceptibility to certain microorganisms. This specific reaction has become an important tool in medicine and science forming the basis of immunisation treatments as well as analytical techniques such as the immunoassay.

1.1.4.1 Antibody Structure and Function

Antibodies, or immunoglobins (Ig), are a group of glycoproteins found in tissues and blood serum which are produced by B-cell lymphocytes. They can be divided into five classes (IgG, IgM, IgA, IgE and IgD) which can be further split into sub-classes (IgG_1, IgG_2 etc). The IgG class is predominant in animal serum, making up about 75% of the total immunoglobins.[19]

IgG's consist of four polypeptide chains, two light and two heavy, linked together by disulfide bridges to form an antigen-binding fragment (F_{ab}) and a crystallisable fragment (F_c). The two identical heavy chains have a molecular weight of about 50 kDa and the two light chains around 25 kDa, each has an N-terminal variable region and a C-terminal constant region.[20]

Within the variable regions of each chain there are segments of hypervariability (Figure 1.4) where the amino acid sequences vary extensively between antibodies. It is these regions which provide the specificity to react with a particular antigen and they are hence known as the complementarity determining regions (CDR). The highly specific antibody-antigen interaction occurs via the CDR of the antibody and a small fragment of the antigen called the antigenic determinant or epitope.

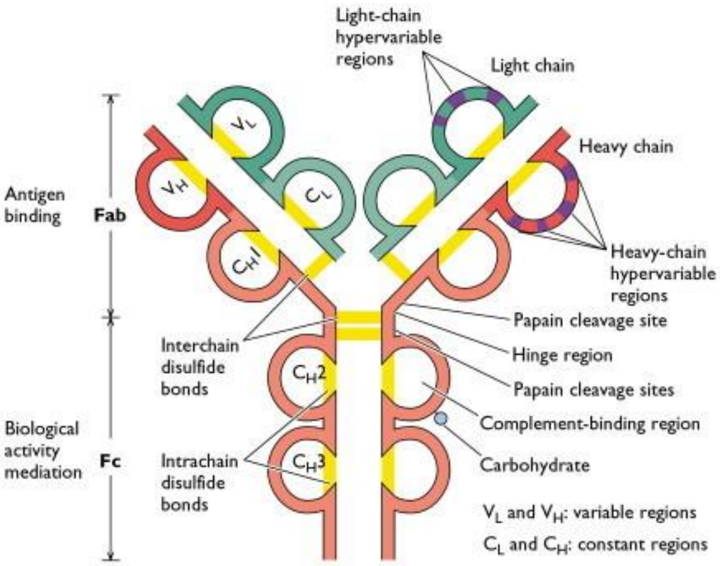

Figure 1.4. *Structure of an IgG antibody*[21]

The F_c region of the antibody is at the constant C-terminus. This region binds to F_c cell surface receptors and the complement proteins, and is thus responsible for triggering a specific biological response.

1.1.4.2 Monoclonal and Polyclonal Antibodies

By introducing an antigen into an animal it is possible to stimulate the production of antibodies specific to that antigen. Such administration *in vivo* will stimulate different cells of the immune system leading to a mixture of antibodies, produced from a number of B-cell lymphocytes. Such antibodies are so called polyclonal antibodies and are generally produced in rabbits, sheep or goats.

Monoclonal antibodies are those derived from a single clone of B-cells, they are therefore more specific than polyclonal antibodies and are consequently favourable in diagnostic and therapeutic applications.

The first production of specific monoclonal antibodies was by Köhler and Milstein in 1975.[22] They described the isolation of antibody-forming cells from the spleen of mice which had been immunised with a specific antigen. The isolated cells can be fused with immortal tumour cells to form hybridomas which are subsequently screened for antibody production. Those cells which are producing monoclonal antibodies of interest are then isolated, cloned and allowed to grow in culture (Figure 1.5). Cell culture lines can be kept alive for indefinite periods allowing for the mass production of highly specific monoclonal antibodies which can then be harvested for subsequent use as therapeutic agents or in immunoassays, allowing for the treatment of disease or detection of virtually any protein.

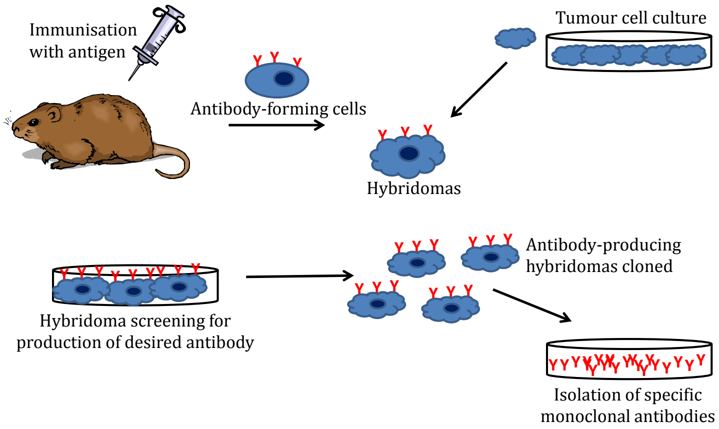

***Figure 1.5.** Schematic representation of the procedure for production of monoclonal antibodies.*

Immunoassays are based on the specific interactions between antibodies and antigens and thus, as mentioned previously, a thorough understanding of the interactions is desirable for the production of immunoassays. Additionally, an understanding of the protein-surface interactions is required so that proteins are adsorbed in the orientation and conformation required for retention of their activity and binding capacity.[23]

Moreover, the interaction of cells with surfaces is largely dependent on protein-surface interactions, since it is proteins which are involved in the adhesion of cells to tissues and other substrates. Therefore, an understanding of protein-surface interactions is essential in cell-surface interaction studies.

1.2 Surface Patterns for Detection and Control of Biomolecules

The patterning of surfaces can allow an even greater understanding and unprecedented control over the behaviour of biomolecules. By allowing the organisation of multiple biomolecules on a surface with high resolution, the development of biomedical devices and technology can be achieved.[24] It is therefore unsurprising that patterning of surfaces for biomolecular control is an area of considerable research.

1.2.1 Surface Patterning for Protein Applications

Contrary to traditional methods of protein analysis which provide information on individual proteins, protein arrays allow for the simultaneous processing of thousands of proteins in high-throughput to facilitate function studies for the whole cell, tissue or organism. Array-based methods can be utilised to scan for protein-protein interactions, identify substrates of protein kinases and identify protein targets of small molecules.[25]

Original protein patterning was intended for applications in bio-electronic devices.[26] However, since the functionality of proteins is so diverse, the patterning of proteins on a surface was soon applied to a variety of areas for the study of protein function,[25] protein-protein interactions,[27-29] antibody profiling[30-32] and immunoassay arrays for specific analyte detection.[33-35]

The concept of a protein detecting microarray was first coined by Ekins in 1989.[36] However, the idea wasn't fully fabricated until 1998 when Silzel *et al.* used a standard inkjet printer to make multianalyte arrays using 200 μm spots of monoclonal antibodies on a polystyrene film. Using a sandwich type assay, they demonstrated specific, concentration dependent recognition of human myeloma proteins with minimal cross-reactivity.[33] MacBeath and Schreiber printed over 10,000 spots of Protein G on half a slide, with a single spot of FKBP12-rapamycin binding (FRB) domain in the centre, and showed that the single spot of FRB could be isolated using a fluorescently labelled protein (Figure 1.6).[25] Moody *et al*. later developed an assay capable of detecting and quantifying seven human cytokines from a biological sample by printing in the wells of a microtitre plate.[37]

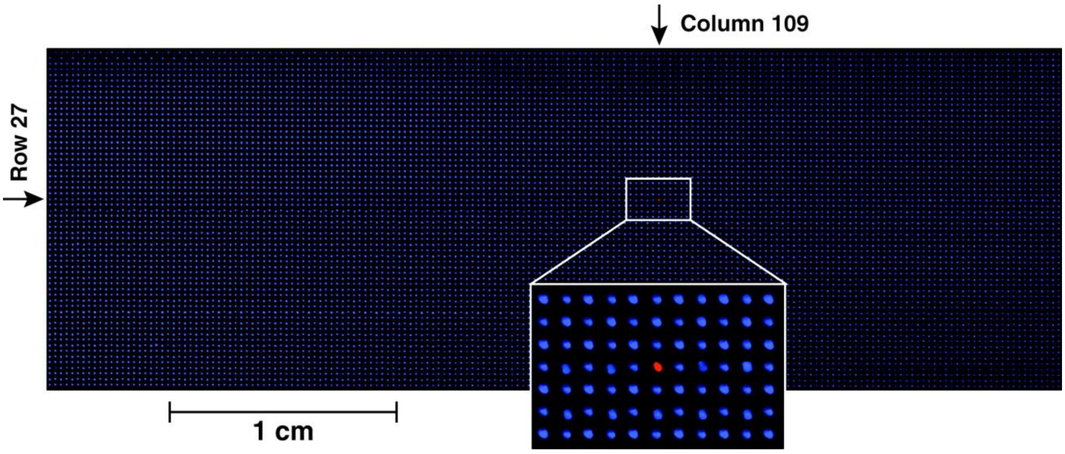

Figure 1.6. *A single slide holding 10,800 spots. Protein G was printed 10,799 times. A single spot of FRB was printed in row 27, column 109. The slide was probed with BODIPY-FL-IgG (0.5 µg/ml), Cy5-FKBP12 (0.5 µg/ml), and 100 nM rapamycin. BODIPY-FL and Cy5 fluorescence were false-coloured blue and red, respectively. The clear visibility of the single FRB spot indicated the ability to specifically detect the single interaction amongst the mass of protein G.[25] Reprinted with permission from AAAS.*

By offering the possibility of large scale analysis across the proteome as well as focused experiments on specific interactions, protein arrays provide development for protein-based diagnosis. With high throughput and less sample consumption they provide an invaluable tool in proteomics for diagnostics, disease progression studies and for the identification of disease associated biomarkers.[27]

Depending on the purpose of the array, different formats such as antibody or antigen arrays, functional arrays or capture arrays may be utilised. Each format differs in the type of protein which is immobilised on the surface i.e. in an antibody array, mono- or polyclonal antibodies are arrayed and used to detect and quantify specific proteins in a sample whereas in a functional array, purified proteins are immobilised and used to detect and characterise protein-protein, protein-DNA or protein-small molecule interactions.[38]

1.2.2 Surface Patterning for Cellular Interactions

Understanding cellular interactions gives an insight into the behaviour of cells in the natural environment which can be applied to various useful applications such as tissue engineering and implantable devices.

In nature, cells exist within the extracellular matrix (ECM), a network of biomolecules which provide support to cells whilst facilitating attachment and regulating cellular processes. The ECM is mainly composed of polysaccharides and a variety of proteins, some of which are used by the cells to attach to the ECM. Since proteins play an important role in the interactions of cells with surfaces, protein-surface interactions can be exploited for the control of cell-surface interactions. Therefore, protein arrays can also be applied for cell adhesion studies.[39]

Aside from protein arrays, cells are known to respond to other types of surface pattern which reflect the focal adhesion points of their natural environment. A significant example of this is cellular response to topographical changes which suggests that the ECM controls cellular behaviour via both chemical and topographical signalling. Chen *et al*. showed that patterns on a surface can affect cell spreading and even induce cell death.[40] Further studies have also shown that cells will respond to topographical changes by altering their growth to respond to grooves or patterns.[41-42]

Such responses of cells to changes in surface topography can be controlled and exploited for controlling stem cell differentiation,[43] generating complex multicellular structures[44] and for altering the gene expression of cells.[45] This control of stem cell differentiation and cellular structure is extremely useful for tissue engineering and developing implantable devices.[46-48] An example can be observed in Figure 1.7, where cells on a nanografted substrate formed well-defined multicellular structures, as opposed to the confluent monolayers formed on flat surfaces, and were shown to produce capillary tubes suitable for vascular engineering.[44]

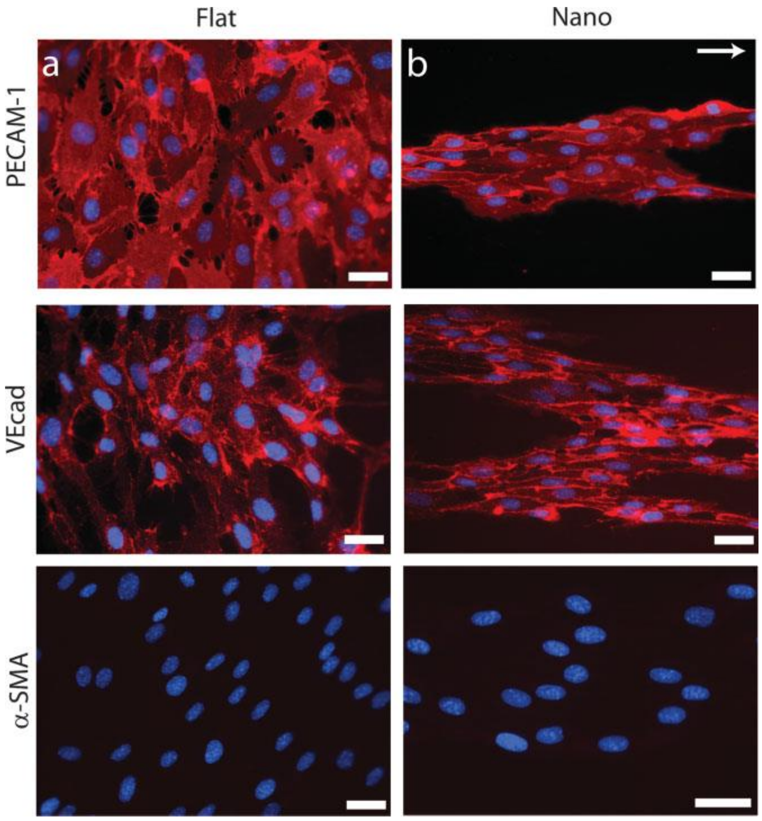

Figure 1.7. *Endothelial progenitor cells (EPCs) cultured on flat substrates formed confluent layers* ***(a)*** *whereas EPCs cultured on nanografted substrates began to form multicellular band structures aligned in the direction of the features* ***(b)****. These morphological differences are evident through staining of PECAM-1 and VEcad. The absence of α-SMA suggests that these cells maintain their endothelial cell phenotype. The protein-level expression of these endothelial-specific markers is similar in cells cultured on both nanotopographic and flat substrates. The direction of the linear nanotopographic features is indicated by the arrow. Scale bars are 50 μm.*[44] *Reprinted by permission of John Wiley and Sons. Copyright © 2008 WILEY-VCH Verlag GmbH & Co. KGaA, Weinheim.*

1.2.3 Patterning Methods for Biomolecular Control

The ability to produce miniaturised patterns is advantageous for the applications discussed herein. For protein arrays, miniaturisation allows denser arrays to be printed containing more information, as well as quicker reactions and lower sample consumption; and for controlling cell behaviour, the nanoscale changes in surface pattern reflect those which occur in the natural environment.

Advances in technology have led to a range of patterning techniques which are capable of nanoscale fabrication. The choice of technique depends to a certain extent on the application being investigated; however, some of the more common nanofabrication techniques are photolithography, e-beam lithography, dip-pen nanolithography (DPN), nanografting, nanoimprint lithography (NIL), microcontact printing (μCP) and scanning tunnelling microscopy (STM).

Techniques such as photolithography[49] and e-beam lithography[50] involve the patterning of surfaces through the use of a UV- or electron-sensitive resist layer. Photolithography is carried out through a mask and e-beam lithography works by the controlled movement of the electron-beam. Although capable of high-throughput fabrication, the use of a mask limits the precise patterns which can be achieved using photolithography. E-beam lithography is less limited and precise patterns can be achieved with extremely high-resolution.[51] However, patterning with e-beam lithography is slow and the required systems are expensive.

NIL[52] and μCP[53] are cheaper methods of nanofabrication but they are more limited in the molecules and substrates which can be utilised. They both use moulds or templates produced by other methods for the production of surface patterns.

DPN is a technique which can overcome the limitations of each of these aforementioned methods and is suitable for a wide variety of applications.

1.3 Dip-Pen Nanolithography

Of the techniques capable of nanoscale printing, DPN is desirable as it is relatively cheap to buy and run, has extremely high accuracy and resolution, and can function under ambient conditions.[54] DPN is also capable of directly printing a variety of different inks without the use of a mask or resist which allows excellent control over feature size, shape and position. Furthermore, modifications of the technique have also been designed to extend the applicability of DPN to a vast range of areas including biosensing, controlled assembly of materials and fabrication of electronic devices.[55]

1.3.1 Basic Concept

DPN is a direct-deposition technique developed by Mirkin's group in 1999[56] which utilises an AFM tip to "write" molecular substances on a solid substrate in a similar fashion to that of a dip pen. When the molecular coated tip comes into contact with the substrate, molecules with a chemical affinity to the surface diffuse onto the substrate via a meniscus and are chemically anchored to the surface to form well-ordered patterns (Figure 1.8).

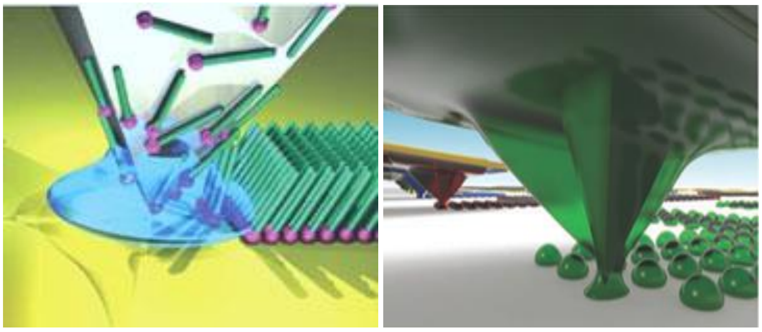

Figure 1.8. *Dip-pen nanolithography process where an AFM tip acts as a pen, molecules as ink, and a solid substrate as paper, to directly write nanoscale and microscale patterns of molecules via a water meniscus (left)[57] or liquid ink meniscus (right).[58] Reprinted by permission from Macmillan Publishers Ltd: Nature Nanotechnology (reference 57), Copyright © 2007 and Nanoink Inc. (reference 58) Copyright © 2011.*

Traditionally, ink molecules are transferred from the tip to substrate via a water meniscus which forms at the tip-substrate interface (Figure 1.8 left). This method of ink transport is influenced by factors such as temperature and humidity as well as method of tip coating and tip-substrate contact time.[59-60] More recently, liquid ink transport (Figure 1.8 right) is becoming increasingly popular as it facilitates printing of biomolecules, polymers and metals.[35, 61-62]

Liquid inks are particularly suitable for use with multi-channel inkwell arrays thus allowing printing of multiple inks simultaneously (Figure 1.9). The transport of the ink from tip to substrate is dependent on factors such as ink viscosity and surface tension between the ink and substrate surface.[62-64] In comparison to transport via a water meniscus, liquid ink transport requires shorter dwell times and thus faster printing can be achieved.[64] Liquid ink printing is achieved by using an ink or carrier liquid which flows through the microfluidic inkwell arrays and maintains hydration throughout the printing process. The carrier liquids can also facilitate the retention of biomolecule activity, hence the suitability of the liquid ink transport method for printing of biomolecules.[63]

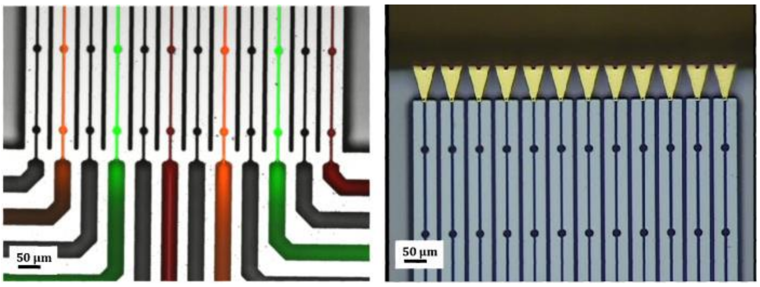

Figure 1.9. *Illustration of the ability to print multiple inks simultaneously using inkwell arrays and multi-pen cantilevers. Left: inkwell arrays with different fluorescent inks in six of the microfluidic channels. Right: Multiple pens inking simultaneously using the inkwell arrays.*[65] *Reprinted by permission of John Wiley and Sons. Copyright © 2010 Wiley Periodicals, Inc.*

DPN is capable of writing micro- and nano-sized features in both a bottom up (self-assembly, templating)[66] and top down (resist-based)[67] manner. The versatile, robust and high resolution technique can be used to deposit a variety of organic and inorganic molecules onto a variety of substrates under ambient conditions.[68] The ability to work under mild conditions is especially important when handling biomolecules. Alternative nanolithography methods, such as e-beam lithography and photolithography, are therefore unsuitable for direct fabrication of biomolecule arrays.[69] Since DPN is a direct-write technique, materials of interest can be placed precisely and exclusively where desired, without the use of a mask or any complicated processing steps.[54]

1.3.2 DPN Process Development

Desired patterns are produced by printing dots and lines in specific arrangements. Dot patterns are achieved by holding the coated tip in a fixed position to form circular "dots" whereas lines are generated by moving the tip at a constant speed, whilst in contact with the substrate (Figure 1.10). Research has shown that ink transport rate, feature size and line width can be controlled by varying conditions such as humidity, temperature, and tip to surface contact time.[39, 59, 70-71] The chemical nature of the ink and substrate are also contributing factors with the strength of each effect also depending on the method of ink transport.

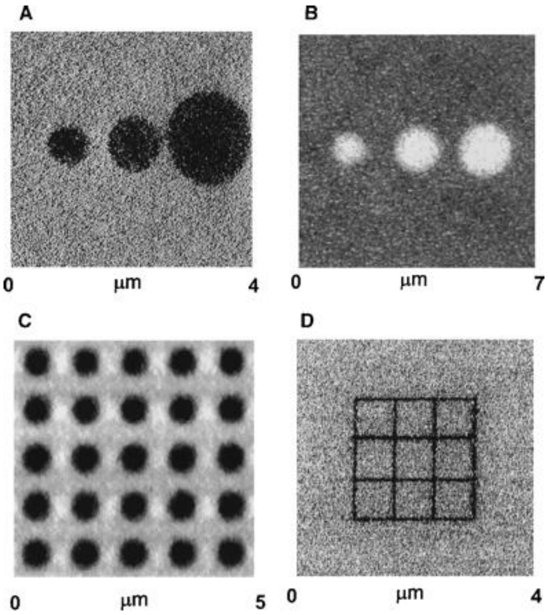

Figure 1.10. *Lateral force images of dots of ODT* ***(A)*** *and MHA* ***(B)*** *on gold with varying dwell times (DT), showing the different transport properties of the two inks.* ***(C)*** *A dot array of ODT produced using 20 s DT and* ***(D)*** *a grid of ODT produced by printing lines of 100 nm width and 2 µm length which took 1.5 minutes to write.[56] Reprinted with permission from AAAS.*

Figure 1.10 gives an indication of how different ink properties can affect the ink transport rates and thus the resulting patterns, particularly in the water meniscus transport method. In Figure 1.10 A, ODT dots were printed using 2, 4 and 16 minute dwell times. However, in the case of MHA (Figure 1.10 B) dwell times of only 10, 20 and 40 seconds were applied. This is due to the different functionalities of the two inks and the fact that ODT is more hydrophobic than MHA. Therefore, transfer of ODT into the water meniscus is less desirable and so the ink transports at a much slower rate in comparison to MHA.[56, 59] This also results in different response to varying conditions, such as humidity, and so careful consideration of all properties must be taken to ensure maximum efficiency in printing and control over feature dimensions.

1.3.3 Applications of DPN

Initial work on DPN by Piner *et al*. involved the use of an AFM tip to direct-write alkanethiols with 30 nm resolution on a gold film.[56] Since this introduction, the technique has been utilised for the deposition of many different materials, on a wide range of substrates, demonstrating vast versatility in application. Zhang *et al*. combined DPN with chemical etching for the fabrication of gold arrays, with sub-50 nm features.[67] Demers *et al*. utilised the technique to produce nanoscale patterns of DNA on gold and silicon oxide surfaces[68] and Li *et al*. developed a new method, known as electrochemical DPN (E-DPN), and used this to fabricate nanoscale features of metals and semiconductors such as platinum, gold and germanium, for potential use in nanoelectronic devices.[72] The possible application of the technique is therefore widespread; however, for the purpose of the work described herein, only the most relevant applications will be discussed further.

1.3.3.1 DPN for Protein Arrays

The advantages of DPN make it a highly desirable technique for the printing of protein arrays.[63, 73-75] Such arrays have proven beneficial in the study of protein interactions,[70] for biomarker profiling,[76] and for the detection of infectious diseases.[77]

Many of the applications involve the indirect patterning of proteins.[71, 77-78] For example, Lee *et al*. printed nanoarrays of MHA on gold, passivated the remaining surface to reduce non-specific binding then immobilised antibodies specific to the HIV-1 p24 antigen onto the MHA arrays (Figure 1.11). They then carried out an immunoassay for the detection of HIV-1 and were able to selectively detect the analyte from clinical samples.[77] Hyun *et al*. also used DPN to print self-assembled monolayers (SAMs) of MHA on gold, which they subsequently used for immobilisation of an elastin-like polypeptide (ELP) and employed the temperature-sensitive patterns for the controlled adsorption and release of proteins.[79]

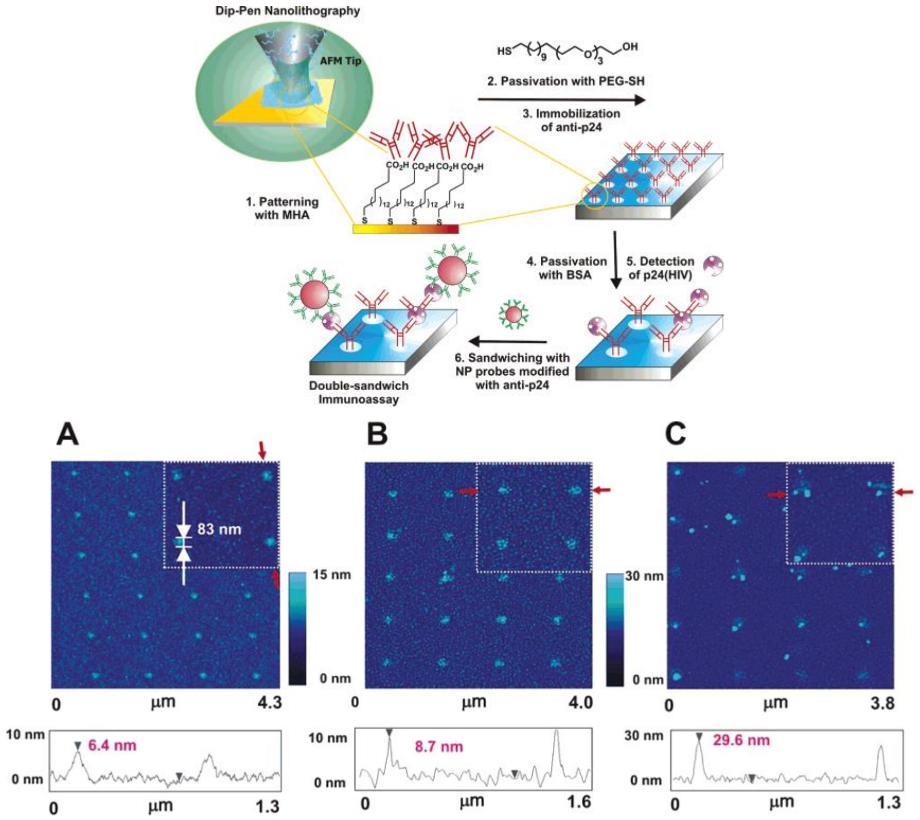

Figure 1.11. *Indirect patterning of immunoassay arrays for the detection of HIV-1 p24 (0.2 pg/mL). (A) Anti-p24 IgG protein nanoarray. Topography trace of adsorbed anti-p24 IgG (6.4 ± 0.9 nm) on MHA, showing a height profile consistent with a monolayer of anti-p24 IgG. (B) After p24 binding to anti-p24 IgG, an average height increase of 2.3 ± 0.6 nm for the IgG features is observed. (C) p24 detection after amplification with anti-p24 IgG coated gold nanoparticles (20 nm). An average topographic change of 20.3 ± 1.9 nm is observed.[77] Reprinted with permission. Copyright © 2004, American Chemical Society.*

However, as well as indirect protein printing, DPN has also been used for the patterning of protein molecules directly onto the surface for subsequent analysis.[35, 73, 75] Irvine *et al*. used liquid ink transport to deposit antibodies onto a nitrocellulose surface and developed immunoassay arrays for the detection of prostate-specific antigen (PSA)[35] and Wu *et al*. coated AFM tips and used DPN to print fluorescent proteins on the submicron scale.[75] Senesi *et al*. also used direct printing of proteins (and oligonucleotides) by employing agarose as a carrier matrix for the biomolecules.[63]

The various approaches which have been mentioned demonstrate the adaptability of DPN for the patterning of proteins for the various applications of protein arrays. The miniaturised printing capabilities of the technique, along with the ability to print multiple inks simultaneously, allow the high-throughput analysis of the biomolecules for the detection of disease and to provide an understanding of biological processes.

1.3.3.2 DPN for Controlling Cellular Interactions

As well as the protein analysis applications mentioned in the prior section, protein arrays fabricated by DPN have also been used for cell adhesion studies.[39, 70]

In an alternative approach, cellular interactions have also been controlled via the printing of alkanethiols by DPN.[80] Curran *et al*. used alkanethiols with various terminal functionalities and showed that functional group, and also spacing between arrays, could be varied to control cellular interactions and the differentiation of mesenchymal stem cells (MSC).[80]

The use of DPN for controlling cellular interactions has been shown as described above; however, the potential of the technique in this area has yet to be reached and so further investigations would be of interest for potential application in regenerative medicine.

1.3.3.3 Polymer Patterning by DPN

Various approaches have been investigated for the patterning of polymers via DPN. The indirect formation of polymer nanopatterns was achieved by Rakickas *et al*. who printed SAMs of MHA on gold then used self-initiated photografting and photopolymerisation (SIPGP) to form hydrogel patterns.[81]

Lim *et al*. directly printed water-soluble polymers using the water meniscus method by functionalising surfaces so that the polymer molecules were transported to the surface via electrostatic interactions.[82] Alternative approaches using liquid ink transport have also been investigated, involving the printing of monomer ink precursors with subsequent polymerisation on the surface.[61, 83-84] On comparing the two ink transport methods, the liquid ink approach appears to give more control over feature size and shape and is also less limited in terms of the requirement of water-soluble polymers.[61]

The advantages of this liquid ink transport method have also been exploited for the printing of other molecules, such as nanoparticles and biomolecules, by using polymers and hydrogels as a carrier matrix for printing.[65, 85]

The majority of polymer patterns produced via DPN have been suggested for their use in electronic devices; however, due to the biocompatibility of polymers and their hydrogels, they also have potential use in biological applications.[65, 81] Since polymer patterns have been utilised previously for the control of cellular interactions,[86-87] this is an area which could be explored using DPN for its advantages in high-resolution patterning.

1.4 Techniques for Biomolecule Detection

Whether patterned on a surface, or in a bulk solution, the detection of biomolecules requires the development of sensitive and high-throughput techniques. There are two main categories of signal generation for use in the detection of biological samples: label-free and label-dependent.

1.4.1 Label-Free Detection

Problems associated with labelling biomolecules such as: the risk of altering protein surface characteristics; variability in labelling efficiency; and time-consuming labelling procedures; may be overcome by the use of label-free detection techniques.[27] Contrary to label-dependent methods, label-free detection depends on the measurement of an inherent property of the molecule, such as mass and dielectric property, or changes in, for example, surface topology on molecular binding.[88] Such techniques avoid any possible interference from tagging molecules whilst providing the possibility to monitor interactions. Many label-free detection methods have emerged such as mass spectrometry (MS) based techniques, surface plasmon resonance (SPR) and atomic force microscopy (AFM).

1.4.1.1 Surface Plasmon Resonance (SPR)

SPR is a surface sensitive, spectroscopic method that can monitor biological interactions without labelling. Capture molecules are immobilised on a metal surface, unlabelled target molecules are added, and a change in the angle of reflection of light is measured.[89] The angle at which the minimum intensity of the reflected light is obtained is known as the “SPR angle”, which is proportional to the amount of target molecules bound to the metal surface.[88] SPR has been widely utilised for the study of biomolecular interactions for disease diagnosis. Campagnolo *et al.* utilised the technique to measure binding kinetics of serum antibodies to human tumour antigen for the rapid diagnosis of cancer.[90] de Boer *et al.* also demonstrated its capabilities for detection of infection status by developing an SPR-based microarray for the screening of antibody profiles.[91] Variations of SPR have also been developed, such as SPR imaging (SPRi)[92] and nanohole arrays.[93]

1.4.1.2 Atomic Force Microscopy (AFM)

The first report of AFM for the imaging of surfaces was by Binnig *et al.*[94] The high resolution technique involves the scanning of a sharp silicon nitride cantilever tip back and forth across a surface. In proximity of the sample surface, a force is felt by the cantilever causing it to deflect. Deflections in the cantilever are monitored optically through the focused laser beam which is reflected to the photodiode detector that will measure any changes in the beam position caused by forces felt during scanning (Figure 1.12). The measurements will then be converted into a detailed image of the surface with sub-nanometre resolution.[95] The main advantages of AFM are its high sensitivity and specificity, and its suitability for detection under physiologically relevant conditions.[88] However, imaging of biomolecules in aqueous solutions can be very difficult and image artefacts may also be problematic.[88]

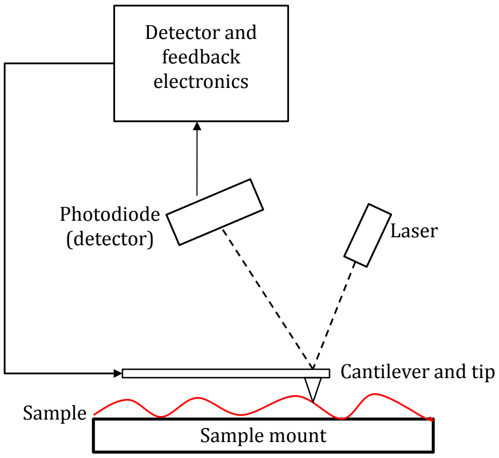

Figure 1.12. *Schematic diagram illustrating the basic functioning of the atomic force microscope.*

1.4.2 Label-Dependent Methods

Although label-free methods have their advantages, they are not easily applied to solution-based detection, and techniques such as AFM lack real quantification capabilities. Label-dependent methods rely on the introduction of a label either by direct attachment to the target molecule, or in a sandwich format where the label is attached to a detection antibody either directly or via another specific interaction. Labels are typically fluorescent dyes, radioisotopes or enzymes which will produce a detectable signal on reaction with a chromogenic or chemiluminescent substrate.

Fluorescence based detection is the most common of the label-dependent methods because it is safe, simple and sensitive with high-resolution.[27, 29] Moreover, many bright and pH stable dyes have been developed with improved emission and excitation spectra, and the method is compatible with standard readily available scanners.[96]

1.4.2.1 Fluorescence Detection

Fluorescence occurs when a molecule, known as a fluorophore, absorbs a photon of light causing the promotion of the species from the ground electronic state to a higher vibrational level of the excited state. Since this higher energy state is unstable, vibrational relaxation occurs to the lowest excited state, followed by relaxation back to the ground state which is accompanied by the emission of light known as fluorescence (Figure 1.13).

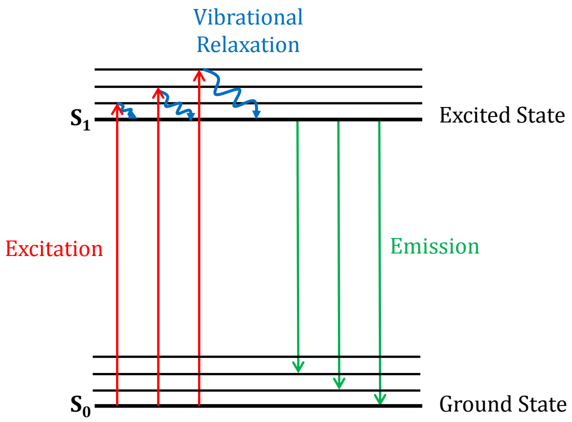

Figure 1.13. *A Jablonski diagram showing the processes of absorption/excitation and emission.*

Since the emitted light is lower in energy, it has a longer wavelength than the absorbed light. Generally, the intensity of the emitted light is proportional to the concentration of the fluorophore which enables quantification of analytes. However, qualitative capabilities are minimal since spectra are not specific to individual molecules. Furthermore, the broad bands which are produced limit multiplexed detection as peaks of different fluorophores tend to overlap. Despite these disadvantages, the use of fluorescence detection is still widespread in protein detection and quantification and also for cell imaging and structure determination.[35, 43, 76, 97-98]

1.5 Raman Spectroscopy

Raman spectroscopy is an alternative optical detection technique which can overcome some of the disadvantages of other methods, such as fluorescence. One of the main advantages is the generation of a unique spectrum corresponding to the structure of the molecule in question, known as a fingerprint spectrum. This allows qualitative analysis and also enables simultaneous detection of multiple analytes. Conventional Raman scattering is label-free; however, modifications of the technique involving the incorporation of labels, or dyes, are also available.

1.5.1 Raman Scattering (RS)

Optical spectroscopy such as absorbance, fluorescence and Raman are based on the interaction between light and molecules and the subsequent generation of a signal. On interaction with a molecule the photons of light may be absorbed or scattered, or they may pass through the molecule without any interaction. Initial studies on the scattering of light focused on elastic scattering, in which scattered photons have the same energy as those of the incident light. This elastic scattering is known as Rayleigh scattering, so named after Lord Rayleigh who discovered the phenomenon.[99] Inelastic scattering, where light leaving the molecule has higher or lower energy to that of incident light, was first observed experimentally by Raman and Krishnan in 1928[100] and has since been referred to as Raman scattering.

When light interacts with a molecule, polarisation of the electron cloud occurs forming a short-lived virtual state. Rayleigh scattering involves only the distortion of the electron cloud with no effect on the nucleus, resulting in just small frequency changes. In Raman scattering however, nuclear motion is induced and energy is transferred from the incident photon to the molecule (Stokes scattering) or from the molecule to the scattered photon (Anti-stokes scattering).[101] The diagram in Figure 1.14 illustrates the energy transitions in each of the three scattering processes.

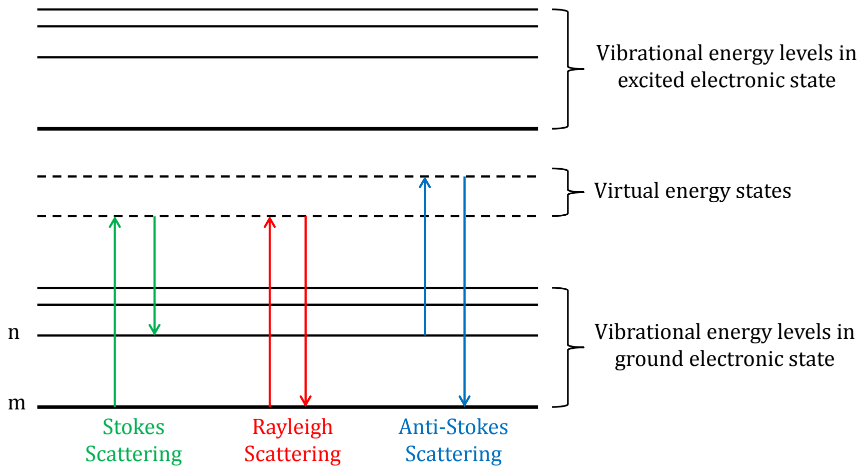

Figure 1.14. *Energy transitions involved in Stokes, Rayleigh and Anti-Stokes Scattering.*

In Stokes Raman scattering, photons are scattered with less energy than incident photons. This is a result of molecules in a ground vibrational state, m, absorbing energy from incident photons and being promoted to an excited vibrational state, n, higher in energy than the ground state. When thermal energy is available, some molecules may be present in an excited vibrational state. Anti-stokes scattering occurs when such molecules lose energy to scattered photons on return to the ground state.

The Boltzmann equation (Equation 1.1) can be used to calculate the ratio of the intensities of Stokes and anti-Stokes scattering, where N_n is the number of molecules in the excited energy state E_n, N_m is the number of molecules in the ground energy state E_m, g is the degeneracy of the levels, $E_n - E_m$ is the difference in energy between states E_n and E_m, k is the Boltzmann's constant (1.3807×10^{-23} JK^{-1}) and T is temperature (K).

$$\frac{N_n}{N_m} = \frac{g_n}{g_m} e^{\left[\frac{-(E_n - E_m)}{kT}\right]}$$

Equation 1.1

At room temperature, the majority of molecules reside in the ground vibrational state and therefore the intensity of Stokes scattering is likely to be higher than that of anti-Stokes scattering.[101]

The shift in energy between the exciting laser beam and the scattered energy, also termed Raman shift, corresponds to molecular vibrations. The number of possible vibrations is related to the number of atoms in a molecule, and the frequency of the vibration is related to the mass of the atoms and the bond strength. Therefore, Raman spectroscopy gives structural information on molecules in the form of unique vibrational fingerprints.

Since only one in every 10^6 - 10^8 scattered photons will do so with a change of energy, Raman scattering is a relatively weak process and therefore requires intense radiation sources. Lasers are commonly utilised as the radiation source as they provide sufficient power and are also monochromatic thus providing quality data. The problem with visible laser excitation is that it can cause sample degradation as well as possible fluorescent interference.[101]

1.5.2 Resonance Raman Scattering (RRS)

The selectivity and sensitivity of Raman scattering may be improved by using a laser excitation frequency close to an electronic transition in the molecule. This effect, known as resonance Raman scattering (RRS), has been reported to give enhancements of up to 10^6,[102] although enhancements of 10^3 or 10^4 are typical.[101]

In resonance Raman, the absorption of a photon induces the excitation of the molecule into an excited electronic vibrational state, as opposed to Raman scattering where excitation is to a virtual state (Figure 1.15).

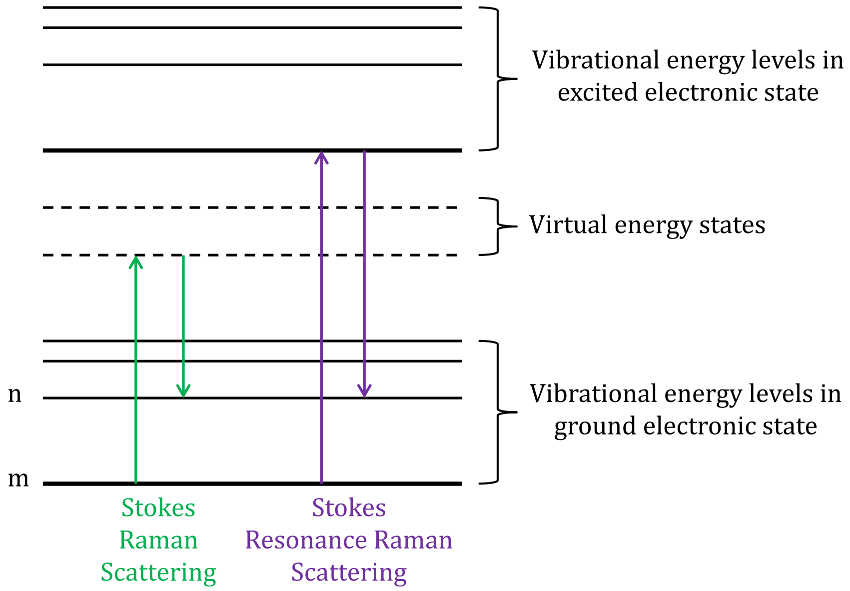

Figure 1.15. *Energy transitions of resonance Raman scattering.*

The enhancement which is observed for resonance Raman scattering can be explained using the Kramer Heisenberg Dirac (KHD) equation (Equation 1.2), where α is the molecular polarisability, ρ and σ are the incident and scattered polarisation direction, Σ is the sum over all vibronic states of the molecule and the remaining terms are constants. G is the ground vibronic state, I is a vibronic state of an excited electronic state and F is the final vibronic state of the ground state.

$$(\alpha_{\rho\sigma})_{GF} = k \sum_{I} \left(\frac{\langle F|r_\rho|I\rangle\langle I|r_\sigma|G\rangle}{\omega_{GI} - \omega_L - i\Gamma_I} + \frac{\langle I|r_\rho|G\rangle\langle F|r_\sigma|I\rangle}{\omega_{IF} + \omega_L - i\Gamma_I} \right)$$

Equation 1.2

Although the complete mathematical explanation is outside the scope of this thesis, the KHD equation can be used to further explain resonance Raman scattering. Under the conditions required for resonance, the energy difference between the lowest vibrational state of the ground electronic state, G, and the resonant vibronic state, I, is the same as that of the exciting light, ω_L. Therefore, the denominator of the first term will be reduced to $i\Gamma_I$ which is very small, and so the first term will become large, resulting in greater polarisability and hence a significant increase in Raman scattering.

As well as the increased intensity of bands which improves sensitivity; RRS also allows the analysis of selectively enhanced molecules, which can therefore be examined without interference from other materials. This is particularly useful in complex matrices such as biological samples, as molecules like proteins and water will undergo only weak Raman scattering; thus eliminating any need for prior separation.

1.5.3 Surface Enhanced Raman Scattering (SERS)

The first observation of SERS was in 1974 by Fleischmann *et al.* who reported an intense Raman signal from pyridine on a roughened silver electrode, which showed enhancement in comparison to adsorption on a smooth silver electrode.[103] This was initially attributed to an increase in surface area allowing more pyridine to adsorb on the surface and thus an increase in the concentration of pyridine in the sampled area. However, two separate research groups later came up with differing theories which both dismissed Fleischmann's hypothesis. Both groups obtained an enhancement in the order of 10^6 which they suggested was too large to be attributed to surface area alone, and that the increase in intensity resulted from a surface enhancement from the roughened silver electrode.[104-105] Jeanmaire and Van Duyne proposed that the enhancement was from an electromagnetic effect[104] whereas Albrecht and Creighton suggested a chemical, charge transfer, enhancement.[105]

It is now widely accepted that SERS enhancement is a combination of both the electromagnetic and the charge transfer effects. However, the electromagnetic enhancement is the dominant process and this occurs when an analyte is adsorbed or held in close proximity to the metal surface leading to an interaction between the analyte molecule and the surface plasmons. The molecule need not be bound directly to the surface for this enhancement effect to be observed. When the laser is tuned in resonance with the surface plasmon, excitation of the plasmons leads to an electromagnetic field which reaches out of the surface, towards where the analyte is positioned.[106]

The chemical enhancement is a result of the bond formation between the analyte and the metal surface. The formation of such bonds will induce a charge transfer which increases the polarisability of the molecule and in turn increases the scattering effect.[107]

The roughened metal surface required for SERS can be introduced in many forms. The most common are electrodes, metal films and colloidal suspensions of metal nanoparticles. Different metals such as silver, gold, aluminium and copper have been utilised. However, silver and gold are the most suitable for Raman scattering as their surface plasmons have a resonance frequency in the visible region.[101] Generally, the greatest signal enhancement can be achieved from silver.[108] This can be attributed to the greater polarisability of silver which gives rise to larger surface plasmons. In addition, gold possesses a smaller scattering to absorbance ratio and so the scattering from silver is greater.

1.5.4 Surface Enhanced Resonance Raman Scattering (SERRS)

The combination of RRS and SERS led to the development of surface enhanced resonance Raman scattering (SERRS). This technique incorporates both surface enhancement and the use of a resonant chromophore to provide enhancements of up to 10^{14}.[101]

As in RRS, the laser excitation frequency must coincide with, or lie close to, an electronic transition of the chromophore. In SERRS, the enhancement is maximised if this frequency also coincides with the resonant frequency of the surface plasmons on the metal surface.

The use of SERRS overcomes the disadvantages of conventional RS. With improved sensitivity, laser power can be reduced which subsequently reduces the risk of sample degradation. Fluorescence interference is also minimised, as the metal surface can quench fluorescence, but also since the intense Raman peaks will dominate over any fluorescence emission. Furthermore, by introducing a range of dye labels with differing resonant frequencies, multiple laser wavelengths can be used to enable multiplexed detection. These multiplexing capabilities of SERRS, as well as its high sensitivity, are the main advantages over rivalling detection methods such as fluorescence detection.

1.5.5 Raman Mapping

Raman mapping involves scanning of a desired area by moving the laser across the surface whilst obtaining a spectrum at each pixel, resulting in images containing tens of thousands of spectra. Maps can be generated for selected vibrations where the intensity of the vibration of choice will be represented in an image with colour scaling, showing where the least to most intense signal for that particular band was observed.

Raman mapping can be used to show the distribution of various components in a sample and has thus been applied for the analysis of food, drugs and cells.[109-111] Furthermore, the method is also suitable for the label-free detection of protein interactions on a surface.[112]

1.6 Project Aims

This thesis investigates novel platforms for the detection of protein biomarkers and for the potential control of cellular interactions. The initial aim was to investigate the application of enhanced Raman scattering to improve the sensitivity over conventional methods of biomarker analysis. The optimised detection system was then to be adapted to an array format and combined with the advantages of DPN to produce a novel system for the analysis of protein biomarkers. DPN was also to be investigated for an alternative application where novel substrates could be designed for the control of cellular interactions. The aims of the project can be separated into three main sections:

- To investigate the use of Raman spectroscopy for the detection of protein biomarkers. The colorimetric changes in a commercial ELISA were to be followed by UV/Vis spectroscopy, before the application of resonance Raman scattering to determine whether the detection over the conventional colorimetric method could be improved. The employed methods were to be applied to various ELISA systems to assess the versatility and to determine the most suitable conditions for the novel system. The detection of protein biomarkers from human blood samples was to be investigated to determine whether the methods could be applied to clinical samples.

- Following the development of a suitably improved detection method in the traditional ELISA, the assay was to be adapted to an array format to improve throughput and introduce a possibility of multiplexed analysis. The novel combination of DPN with RRS was to be investigated for the detection of protein biomarkers. A suitable substrate had to be determined before the assay was optimised for the quantification of target proteins.

- The final objective was to investigate the design of a novel thermoresponsive substrate for the potential control of cellular interactions. The patterning of a suitable temperature-sensitive ink system by DPN was to be investigated. When an optimised system was obtained and the arrays were successfully fabricated, the behaviour of the patterns on the surface could be probed using AFM and Raman scattering to determine whether changes could be observed with changing temperature. Following the fabrication of thermoresponsive polymer arrays, their ability to control the behaviour of cells by the temperature-induced changes in topography was to be investigated.

2. Experimental

2.1 Development of a Resonance Raman ELISA

All experiments were carried out under ambient conditions. Plasticware was autoclaved prior to use to reduce the risk of contamination.

2.1.1 Materials and Instrumentation

Chemicals and materials:

- ELISA test kit, Quantikine® Human TNF-α Immunoassay (DTA00C, R&D Systems Inc., Abingdon, UK) comprising:
    - 96-well polystyrene microplate coated with mouse monoclonal antibody against TNF-α;
    - polyclonal antibody against TNF-α, conjugated to horseradish peroxidase (HRP);
    - lyophilised TNF-α standard;
    - hydrogen peroxide (H_2O_2);
    - 3,3′,5,5′-tetramethylbenzidine (TMB);
    - 2 N sulfuric acid (H_2SO_4);
    - wash buffer (buffered surfactant with preservatives);
    - assay diluent RD1F (buffered protein base with preservatives);
    - calibrator diluent RD6-35 (animal serum with preservatives).
- Control samples (QC01-1, R&D systems Inc., Abingdon, UK)
- Patient serum samples (obtained from Darren Lee Asquith, Glasgow University)
- Human PSA DuoSet (DY1344, R&D Systems Inc., Abingdon, UK) comprising:
    - Monoclonal mouse anti-human PSA capture antibody
    - Recombinant human PSA
    - Biotinylated goat anti-human PSA detection antibody
    - Streptavidin-HRP

- SureBlue TMB Microwell Peroxidase Substrate (KPL Inc., Gaithersburg, MD, USA)
- ABTS 1-Step Peroxidase Substrate (Thermo Scientific, Northumberland, UK)
- Bovine serum albumin (BSA) (Sigma Aldrich, Dorset, UK)
- Tween® 20 (Sigma Aldrich, Dorset, UK)
- 96-well high-binding polystyrene plates (Sigma Aldrich, Dorset, UK)

Buffers:

- Phosphate Buffered Saline (PBS) – 137 mM sodium chloride, 2.7 mM potassium chloride, 8.1 mM disodium hydrogen phosphate, 1.5mM potassium dihydrogen phosphate, pH 7.2 – 7.4, 0.2 μm filtered.
- Reagent Diluent – 1 % BSA in PBS, pH 7.2 – 7.4.
- Wash Buffer – 0.05 % Tween® 20 in PBS, pH 7.2 – 7.4.

Instrumentation:

- Cary 300 Bio UV-Visible Spectrophotometer
- Renishaw Invia Raman Microscope with an Argon ion laser (514 nm)
- Renishaw Ramascope with a HeNe laser (633 nm)
- Microplate Reader (Labsystems iEMS Reader MF)

2.1.2 Monitoring the Reaction over Time by UV/Vis Spectroscopy

The detection antibody-HRP conjugate from the TNF-α ELISA kit was diluted to 1 in 1600. The two colour reagents (TMB + H_2O_2) were mixed in a 1:1 ratio to produce the substrate solution. In two separate disposable plastic cuvettes, diluted antibody-HRP conjugate (200 μL) was mixed with TMB/H_2O_2 substrate solution (200 μL) and doubly distilled deionised water (dddH$_2$O, 200 μL). Samples were then scanned on the Cary 300 UV/Vis spectrometer from 200 – 800 nm, with spectra collected every 5 minutes for 20 minutes. After 20 minutes, H_2SO_4 stop solution (50 μL) was added to one of the cuvettes and UV/Vis spectra were collected of each sample every 5 minutes for a further

20 minutes. The controls used in this experiment were $dddH_2O$ as a blank, TMB/H_2O_2 substrate solution (200 µL substrate solution + 300 µL $dddH_2O$) and antibody-HRP solution (200 µL diluted conjugate + 300 µL $dddH_2O$).

2.1.3 Studying Spectral Changes using Raman Spectroscopy

Raman spectra of the ELISA product of the TNF-α standard (200 µL, 250 pg/mL) were collected at both 514 nm and 633 nm laser excitation wavelength, before and after the addition of H_2SO_4 stop solution. Samples were analysed in microtitre plates using a 20x long-working distance objective at 100% laser power with the scan centred around 1300 cm^{-1}. WiRE™ 2.0 software (Renishaw PLC) was used to run both Raman spectrometers and spectra were recorded using 3 x 3 second accumulations. Each sample was prepared in triplicate and three spectra were recorded for each. Spectra were baseline corrected using a multi-point polynomial fit and level and zero levelling mode in Grams software (AI 7.00). Average peak intensities were obtained from raw data using the maximum and minimum points of the relevant Raman band.

UV/Visible absorption spectra were collected in parallel from a disposable plastic cuvette containing the ELISA product from the 500 pg/mL TNF-α standard (250 µL) and $dddH_2O$ (250 µL).

2.1.3.1 Computational Studies

Computational studies were conducted using the programs GAMESS, version Jan. 2009 (R1),[113] or Gaussian03, Revision E.01.[114] Geometries have been fully optimised without symmetry constraints, involving the functional combinations according to Becke (hybrid) and Lee, Yang, Parr (denoted B3LYP)[115] as implemented in the program, or in the case of the charge transfer complex with the BP86 functional[115-116] in connection with Grimme's dispersion correction[117] (denoted BP86-D). For all calculations the Pople standard 6-311G(d) basis set was used for all atoms. All obtained stationary points were subject to frequency calculation to confirm the minimum on the EPS (no imaginary frequencies). Raman spectra were calculated with Gaussian at the B3LYP/6-311G(d) level of theory.

2.1.4 Quantification of TNF-α by Resonance Raman Spectroscopy

The aforementioned ELISA test kit was used in accordance with the manufacturer's instructions (R&D Systems Inc., UK). TNF-α standard (10 ng) was reconstituted with doubly distilled deionised water (1 mL) to yield a 10 ng/mL stock solution. Dilutions of this standard were made up in animal serum (Calibrator Diluent RD6-35), also provided in the kit.

TNF-α standards, control samples and human blood serum samples (200 µL) were incubated for 2 hours at room temperature in the wells containing immobilized mouse monoclonal antibody against TNF-α. After incubation, the wells were aspirated and washed four times with wash buffer. Anti-TNF-α HRP conjugate (200 µL) was added to each well and incubated for 2 hours at room temperature. Following another series of wash steps with wash buffer, substrate solution (TMB/H_2O_2, 200 µL) was added and the reaction was left to proceed for 20 minutes. Optical density and Raman measurements of the blue charge transfer complex (CTC) were carried out at this stage. For the yellow diimine oxidation product (TMB^{2+}), analysis took place after the addition of 2N sulfuric acid solution (50 µL).

Absorbance measurements were recorded using a microplate reader at 620 nm for the one-electron oxidation products and at 450 nm for the two-electron oxidation product. Raman spectra were collected from the ELISA products using the same method as described in Section 2.1.3 above.

2.1.4.1 Quantification of TNF-α in Controls

The control samples contained a mixture of thirteen recombinant human cytokines at low, medium and high levels in porcine serum. The controls were supplied lyophilised and were reconstituted with $dddH_2O$. Three samples of each control were analysed in the above ELISA, with absorbance readings and Raman spectra collected in triplicate for each sample.

The ELISA was carried out using a standard dilution series (0 – 1000 pg/mL) and the Raman spectra (CTC at 633 nm) and absorbance measurements (TMB^{2+} at 450 nm and CTC at 620 nm) were recorded in the same way as described previously. Results for each method were used to plot a standard curve against which the concentrations of the control samples, treated as unknowns, could be calculated.

2.1.4.2 Quantification of TNF-α in Human Serum Samples

Human blood serum samples of eight patients diagnosed with rheumatoid arthritis (RA) were analysed for their TNF-α content. The serum samples had already been processed as required and were therefore ready for analysis. The patients had been administered disease-modifying anti-rheumatic drugs (DMARD) and the concentration of TNF-α in their blood was unknown. The samples were treated as unknowns in the ELISA, in the same way as the controls (Section 2.1.4.1), and were analysed for their TNF-α content using both absorbance and RRS detection via the methods previously described.

2.1.5 Quantification of PSA by a Resonance Raman ELISA

The PSA DuoSet outlined in section 2.1.1 was used for the development of the ELISA. PSA capture antibody (0.1 mg/mL in PBS, 100 μL) was added to each well before the plate was sealed and allowed to incubate overnight. Each well was washed 3 times with wash buffer (400 μL) before addition of reagent diluent (300 μL) and incubation for a minimum of 1 hour. Reagent diluent was then removed and the wells were washed three times with wash buffer (400 µL). Two-fold dilutions of PSA in reagent diluent (60 – 0.94 ng/mL) were prepared and each was added to its designated well (100 µL). Reagent diluent only (100 µL) was added to one of the wells as a blank control. The slide was then left to incubate for two hours followed by three washes with wash buffer. Biotinylated detection antibody in reagent diluent (200 ng/mL, 100 µL) was then added to each well and left to incubate for a further two hours on a plate shaker. Following another set of three washes, streptavidin-HRP (100 µL) was added to each well and left to incubate for 30 minutes. Once again the wells were washed three times before the addition of SureBlue TMB Microwell Peroxidase Substrate or ABTS peroxidase substrate (100 µL). After 20 minutes of incubation, the ABTS reaction was stopped using 1% SDS and the oxidation products (both TMB and ABTS) were then analysed in the microtitre plates using the Renishaw Ramascope (633 nm) with a 20x long-working distance objective at 100% laser power with the scan centred around 1300 cm^{-1}. WiRE™ 2.0 software (Renishaw PLC) was used to run the spectrometer and spectra were recorded using 3 x 3 second accumulations.

2.1.6 Further Enhancement by SERRS

2.1.6.1 Nanoparticle Synthesis

Prior to nanoparticle synthesis, all glassware was soaked in *aqua regia* for a minimum of 4 hours before being thoroughly rinsed with distilled water. The Turkevich method was used for the synthesis of colloidal gold nanoparticles in the 15-20 nm size range.[118] $NaAuCl_4$ (50 mg, 0.14mM) was dissolved in distilled water and heated until boiling with continuous stirring. Upon boiling, sodium citrate (1.5mL, 1% (w/v)) was added and left to boil for a further 15 minutes. The solution was then removed from the heat and left to cool to room temperature. The absorption maximum of the resulting citrate-reduced gold colloid was observed at 521 nm.

2.1.6.2 SERRS Analysis

Using the same methods as described in Section 2.1.4 and 2.1.5, the ELISAs were carried out on the standard dilution series of TNF-α and PSA, respectively. The ELISA was carried out in duplicate and prior to Raman analysis citrate reduced gold colloid (200 µL), prepared as described above, was added to one set of ELISA products. Both sets were then analysed in microtitre plates on the Renishaw Ramascope (633 nm) using a 20x long-working distance objective at 100% laser power with the scan centred around 1300 cm^{-1}. WiRE™ 2.0 software (Renishaw PLC) was used to run the spectrometer and spectra were recorded using 3 x 3 second accumulations. Origin Pro was used to plot the intensity against the concentration of TNF-α and PSA for the experiment with and without gold colloid. Average intensities were taken from the raw data. For illustration of the spectra, baseline correction was carried out in Grams software (AI 7.00) using a multi-point polynomial fit with level and zero levelling mode.

2.2 PSA Immunoassay Arrays with RRS Detection

All experiments were undertaken at room temperature and humidity (40 - 60%).

2.2.1 Materials and Instrumentation

The Human PSA DuoSet, BSA, Tween® 20, PBS, wash buffer and reagent diluent were used as described in section 2.1.1.

Chemicals:

- TMB-Blotting solution (Thermo Scientific, Northumberland, UK)
- Protein carrier buffer (NanoInk Inc., Skokie, IL, USA)

Materials:

- Nexterion® Slide E MPX 16 epoxysilane activated glass slides with adhesive superstructure wells (Schott, Jena, Germany)

- Nexterion® Slide NC-W (Schott, Jena, Germany)
- Nitrocellulose PATH® slides (Gentel Biosciences, Madison, WI, USA)
- Nexterion® 16-well incubation chamber (Schott, Jena, Germany)
- Inkwell arrays M-6MW (NanoInk Inc., Skokie, IL, USA)
- Type M-ED DPN probe arrays (NanoInk Inc., Skokie, IL, USA)

Instrumentation :

- NLP 2000® (NanoInk Inc., Skokie, IL, USA)
- Alpha300 R confocal Raman microscope with 633 nm laser excitation (WITec, Ulm, Germany)
- Plasma cleaner (Diener electronic, Nagold, Germany)

2.2.2 Bulk Spotting Capture Antibody

The lyophilised capture antibody was reconstituted in five parts PBS and three parts protein carrier buffer with a final antibody concentration of 2 mg/mL to produce the capture antibody print solution. Using a micropipette, two spots (0.3 µL) of capture antibody print solution were added to each of the wells before overnight incubation at 4 °C. Following the overnight incubation, three wash steps were carried out. Each step involved the addition and subsequent aspiration of wash buffer (0.05% Tween 20 in PBS, 100 µL) to each well.

2.2.3 Fabrication of PSA Capture Antibody Arrays

Prior to printing the arrays, the Type M-ED DPN probe array pens were cleaned using an oxygen plasma for 40 seconds at 50% power, 72 cm^3 / minute. The pens were then mounted on the NLP 2000® chip holder in a position that allowed the use of the M-2 end of the probe array. The M-2 end has 12 “A-frame” shaped cantilevers spaced 66 µm apart. Capture antibody print solution (0.3 µL) was prepared as described previously (Section 2.2.2), and then added to each of the six inkwells. The inkwell arrays (Type M-6MW) were placed on the NLP 2000® stage and the slide was aligned alongside the inkwells prior to levelling the pens with the surface. Plane calculations were then performed before programming the NLP 2000® software to print the required arrays. The first step of the programme was for the pens to contact the perfectly aligned inkwells so that all of the cantilever tips were coated with PSA capture antibody. Excess ink was subsequently removed by "bleeding" in a position out with the desired printing area. The arrays were then printed using a 0.1 second dwell time and either 22 µm or 33 µm pitch to allow equal spacing of the array spots. Once the arrays were fabricated as desired, the slide was incubated overnight at 4 °C. After overnight incubation the slides were washed by shaking in wash buffer (0.05% Tween 20 in PBS), before being placed in the Nexterion® IC-16 incubation chamber. The same method was followed for the fabrication of arrays on epoxysilane glass, 3D nitrocellulose slides and nitrocellulose PATH® slides.

2.2.4 PSA Immunoassay

Subsequent to either bulk spotting or array fabrication, the PSA immunoassay was developed. After the washing step described for each method above, the slide was blocked by adding reagent diluent (1% BSA in PBS, 100 µL) to each well and leaving it to incubate for 1 hour. Reagent diluent was then removed and the arrays were washed three times with wash buffer (100 µL). Two-fold dilutions of PSA in reagent diluent (60 – 0.94 ng/mL) were prepared and each was added to its designated well (100 µL). Reagent diluent only (100 µL) was added to one of the wells as a blank control. The slide was then left to incubate for two hours on a plate shaker followed by three washes with wash buffer. Biotinylated detection antibody in reagent diluent (200 ng/mL, 100 µL) was then added to each well and left to incubate for a further two hours on a plate shaker. Following another set of three washes, streptavidin-HRP (100 µL) was added to each well and left to incubate for 30 minutes. Once again, the wells were washed three times before the addition of TMB-Blotting solution (100 µL). The TMB was left either overnight or for 2 hours on epoxysilane glass, or for

30 minutes on nitrocellulose, before being removed from the wells. After removal of TMB, the slide was removed from the incubation chamber and blown dry under nitrogen prior to analysis by Raman spectroscopy. In the cases where a final wash step was added, dddH_2O (100 µL) was added to each well after the removal of TMB and before drying under nitrogen.

2.2.5 Detection by RRS

Raman scans were collected on the WITec alpha 300 with a 633 nm laser excitation wavelength using the piezo-driven XYZ scan stage. The grating was 600 g mm^{-1} and coupled to a thermoelectrically cooled charge-coupled device (CCD). The spectra were centred at 1300 cm^{-1} and collected with an integration time of 0.1 seconds using either a 50x/0.5 or a 100x/0.9 objective. Image scans were obtained using a 1 µm spatial resolution. Raman maps were generated based on the peak at 1609 cm^{-1} as this gave the most intense signal. When scanning the nitrocellulose slides, the laser power had to be reduced to around 350 µW to avoid burning of the surface.

2.3 Thermoresponsive Polymer Arrays

2.3.1 Materials and Instrumentation

Chemicals:

Chemicals were purchased from Sigma Aldrich (Dorset, UK) unless otherwise stated. All solvents were of laboratory grade.

- N-Isopropylacrylamide (NIPAAm)
- (3-glycidyloxypropyl)trimethoxysilane (GPTMS)
- O,O′-Bis(2-aminopropyl) polypropylene glycol-block-polyethylene glycol-block-polypropylene glycol (Jeffamine ED-600)
- Poly(ethylene glycol) dimethacrylate crosslinker (PEG-DMA)
- Hydroxycyclohexyl phenyl ketone (photoinitiator)

- 3-(trimethoxysilyl)propyl methacrylate (TMSPM)
- (3-mercaptopropyl)trimethoxysilane (MPTMS)
- N,N-diethylacrylamide (DEAAm) (Tokyo Chemical Industry UK Ltd., Oxford, UK)

All chemicals were used as supplied, except Jeffamine ED-600 which was dried under vacuum for 2 hours prior to use.

Cell Buffers and Stains:

- PBS tablets (Sigma Aldrich, Dorset, UK)
- mouse anti-vinculin antibody (clone hVin-1, Sigma Aldric, Dorset, UK)
- biotinylated anti-mouse antibody (Vector Laboratories, Burlingame, CA, USA)
- fluorescein-conjugated streptavidin (Vector Laboratories, Burlingame, CA, USA)
- VECTASHIELD Mounting Medium with DAPI (Vector Laboratories, Burlingame, CA, USA)

Materials:

- Silicon dioxide substrates with registration marks (Nanoink Inc., Skokie, IL, USA)
- Nexterion® Slide E MPX 16 epoxysilane activated glass slides (Schott, Jena, Germany)
- Inkwell arrays M-6MW (NanoInk Inc., Skokie, IL, USA)
- Type M-ED DPN probe arrays (NanoInk Inc., Skokie, IL, USA)
- ACT standard non-contact/tapping mode probes with mounts (AppNano, CA, USA)
- ScanAsyst fluid probes (Bruker, Camarillo, CA, USA)

Instrumentation:

- NLP 2000® (NanoInk Inc, Skokie, IL, USA)

- WITec alpha300 R confocal Raman microscope with 633 nm laser (WITec, Ulm, Germany)
- DPN 5000™ nanofabrication system (Nanoink Inc., Skokie, IL, USA)
- PeakForce QNM Scanning Probe Microscope (Digital Instruments, Santa Barbara, CA, USA)
- Axiovert 200M inverted fluorescence microscope (Carl Zeiss Inc, Jena, Germany)
- Linkam PE94 temperature controlled stage (Linkam Scientific Instruments, Surrey, UK)

2.3.2 Preparation of Surfaces

Silicon dioxide substrates were cleaned by sonication in acetone, isopropanol and water, for 10 min in each solvent, and blown dry with nitrogen after each sonication bath. Substrates were then plasma-cleaned for 40 seconds at 50% power, 72 cm^3 / minute in oxygen. To silanise surfaces with MPTMS, the cleaned substrates were placed in an Erlenmeyer flask with MPTMS (2 mL) in a nitrogen atmosphere for 30 minutes and then placed in an oven at 100 °C overnight before printing. For treating substrates with TMSPM, TMSPM was diluted in ethanol (50 µL in 10 mL) and then dilute acetic acid (1:10 glacial acetic acid:water, 0.3 mL) was added just before use. This silane solution was poured onto the surfaces and allowed to react for 3 minutes. The excess was poured off and then substrates were rinsed with ethanol to remove the residual reagent before being dried dried under a nitrogen flux.

2.3.3 Fabrication of Polymer Arrays

Arrays were fabricated using a Nanoink NLP 2000® nanolithography instrument. 1D M-type pen arrays were plasma cleaned for 40 seconds at 50% power (72 cm^3 / minute) prior to use to remove any organic contamination. All the printing experiments were performed at 22-23°C and in a relative humidity range of 25-35%. NIPAAm ink was prepared by dissolving the monomer in various solvents as described in section 4.2.1 along with 4% PEG-DMA w.r.t. NIPAAm and 0.4% photoinitiator (w.r.t NIPAAm). DEAAm ink was prepared by mixing DEAAm (500 mg), 0.5% wt of PEGDMA w.r.t DEAAm (2.51 mg) and 3% wt of photoinitiator w.r.t DEAAm (15.46 mg) in a closed vial protected from light to minimise the activation of photoinitiator before printing. 0.3 µL of this mixture was then added to an inkwell and the tips were dipped in a 12-channel microfluidic inkwell. Once printed arrays were created, the substrates were exposed to a UV lamp for 5 minutes. For Jeffamine ink, stoichiometric amounts (2:1) of GPTMS (442.4 mg) and Jeffamine ED-600 (494.2 mg) were mixed in a closed glass vial under magnetic stirring at least for 2 hours. Distilled water (100 µL) was then added to the mixture and left under stirring for 10 more minutes. The printed Jeffamine arrays were left in a closed box overnight and then cured at 40°C for 1 h. The Jeffamine/DEAAm ink (mixed system) was made up by mixing the Jeffamine ink, prepared as described above, and the DEAAm ink, including also 1% wt (5.05 mg) of TMSPM w.r.t. DEAAm, in a 1:1 ratio and then directly used for printing. These arrays were UV-cured for 5 minutes, left in a closed box overnight and eventually cured at 40 °C for 1 h.

2.3.4 Characterisation of Polymer Arrays

Raman analysis was carried out using a WITec Alpha300 R microscope (Ulm, Germany) with a 633 nm laser excitation, a 100x/0.9 objective and 5 x 10 second accumulations. The grating was 600 g mm^{-1} and coupled to a thermoelectrically cooled charge-coupled device (CCD). Analysis in liquid was obtained using a 60x/0.8 water immersion objective with a Linkam PE94 temperature controlled stage to achieve temperature control. Peak areas were calculated using a trapezoidal integration in MATLAB® R2012a software.

AFM topography analysis in air was carried out on a DPN 5000™ nanofabrication system (Nanoink Inc., Skokie, IL, USA), in close-contact mode using ACT probes purchased from AppNano (nominal value of spring constant = 40 N/m). AFM images in liquid were obtained by scanning the surface using a PeakForce QNM Scanning Probe Microscope (Digital Instruments, Santa Barbara, CA, USA). The AFM measurements were obtained using ScanAsyst-Fluid probes with a spring constant of 0.67 N/m (nominal value of tip radius = 2 nm). AFM images were processed using SPIP™ processing software.

2.3.5 Analysis of Cellular Interactions

2.3.5.1 Fabrication of Substrates

Arrays of Jeff/DEAAm were printed using a 1 s dwell time on thiol-silanised silicon dioxide substrates with pitches of 22 µm and 100 µm (refer to Sections 2.3.2 and 2.3.3 for preparation details). A thiol-silanised silicon dioxide substrate with no printed arrays was used as a planar control. Substrates were equilibrated for 3 days in distilled water at room temperature, followed by 3 days at 37°C in a humidified atmosphere of 5% CO_2.

2.3.5.2 Cell Culture

Le2 endothelial cells were seeded at a density of 3 x 10^4 cells/substrate and cultured in CO_2-independent HAMS-F10 medium, supplemented with foetal bovine serum (FBS, 2.8% (v/v)), antibiotics (88 µg/mL streptomycin, 88 U/mL penicillin, 275 ng/mL Fungizone), insulin-transferrin-selenium (ITS 1.85% (v/v)), and sodium bicarbonate (0.035% (w/v)) for 1 day at 37^{o}C, followed by 7 days at 33^{o}C.

2.3.5.3. Cell Staining

The cells were fixed in formaldehyde in PBS (3.8% (v/v)), rinsed three times in PBS and permeabilised for 7 minutes in pre-chilled (4^{o}C) permeabilisation buffer (50mM NaCl, 3mM $MgCl_2.6H_2O$, 20mM HEPES, 0.1% (w/v) sucrose, 0.5% (v/v) TX-100 in PBS, pH 7.2). Samples were blocked for 15 minutes at 37^{o}C in bovine serum albumin in PBS (1% (w/v)), incubated with mouse anti-vinculin antibody (clone hVin-1, Sigma) for 1.5 hours at 37^{o}C, rinsed three times (5 minutes/wash) in Tween-20 in PBS (PBST, 0.5% (v/v)), incubated with biotinylated anti-mouse antibody (Vector Laboratories, Burlingame, CA) for 1 hour at 37^{o}C, and rinsed three times (5 min/wash) in PBST. The samples were incubated in fluorescein-conjugated streptavidin for 30 minutes at 4^{o}C, rinsed three times in PBST (5 minutes/wash) and mounted in mountant containing DAPI (Vector Laboratories). Immunostained cells were imaged with an Axiovert 200M inverted fluorescence microscope with Plan Neofluar 20x and 40x objectives.

3. Detection of Protein Biomarkers using a Resonance Raman ELISA

3.1 Introduction

The ability to detect and quantify protein biomarkers with high sensitivity and specificity can allow early disease diagnosis, understanding of disease pathways and monitoring response to treatment. This chapter investigates the use of Raman spectroscopy to improve the sensitivity of the commonplace enzyme-linked immunosorbent assay (ELISA) for the detection and quantification of key biomarkers. The colorimetric reaction of conventional enzyme/substrate systems were monitored using UV/Vis spectroscopy. Raman scattering of the coloured products was then investigated and compared to the standard method to determine whether sensitivity of the assay could be improved.

3.1.1 ELISAs for Biomarker Detection

In an ELISA, an antigen is immobilised on a solid substrate, usually the surface of a microwell, either directly or via a specific reaction with its corresponding antibody. The antigen can be detected directly, using an enzyme labelled primary antibody; indirectly, using an enzyme labelled secondary antibody; or in a sandwich format where the antigen is bound between two antibodies: the capture antibody and the detection antibody (Figure 3.1).

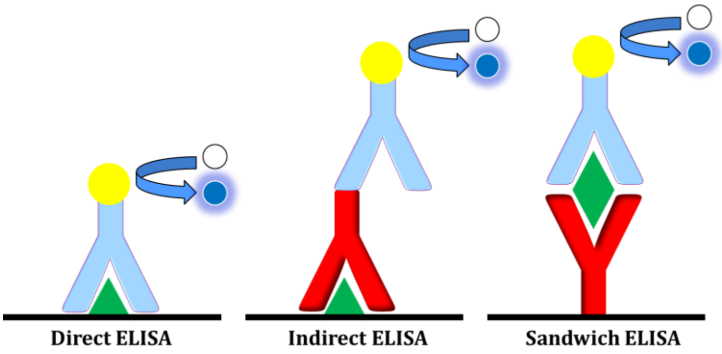

Figure 3.1. *Diagram of three different ELISA formats: direct, indirect and sandwich type.*

The sandwich ELISA is favourable as it is sensitive and robust; there is also no need for sample purification, since the antigen will be selectively bound from the mixture by a specific antibody.

On reaction with a chromogenic substrate, the enzyme will generate a measurable signal which can be correlated to the amount of biomarker present in a sample.

The most common enzyme labels are horseradish peroxidase (HRP), alkaline phosphatase (ALP) and β-galactosidase.[119] HRP is the smallest and most stable of the three and therefore the most desirable.[120] Due to its faster catalytic rate, HRP is also the most sensitive as it generates a strong signal in a short time. However, this makes reactions with HRP self-limiting due to product inhibition of the enzyme.[121] HRP catalyses the oxidation of many reducing substrates by hydrogen peroxide (H_2O_2). The most widely used substrate in this type of system is 3,3′,5,5′-tetramethylbenzidine (TMB) as it is more sensitive and less toxic than alternative substrates such as o-phenylenediamine (OPD) and 2,2′-azino-bis-(3-ethylbenzthiazoline-6-sulfonic acid) (ABTS).

The HRP catalysed oxidation of TMB by H_2O_2 proceeds via a two-step two-electron process as shown in Scheme 3.1. The first step (one-electron oxidation) yields a radical cation which exists in rapid equilibrium with a blue charge transfer complex (CTC) of the parent diamine (TMB^0) and the diimine (TMB^{2+}), where the TMB^0 is the electron donor and the TMB^{2+} is the electron acceptor. By addition of a strong inorganic acid such as sulfuric acid (H_2SO_4), the reaction can be terminated yielding the yellow TMB^{2+}. A spectrophotometer may be used to quantitatively analyse the colour produced, which will be proportional to the amount of analyte in the sample, thus providing a convenient system of detection in ELISAs.

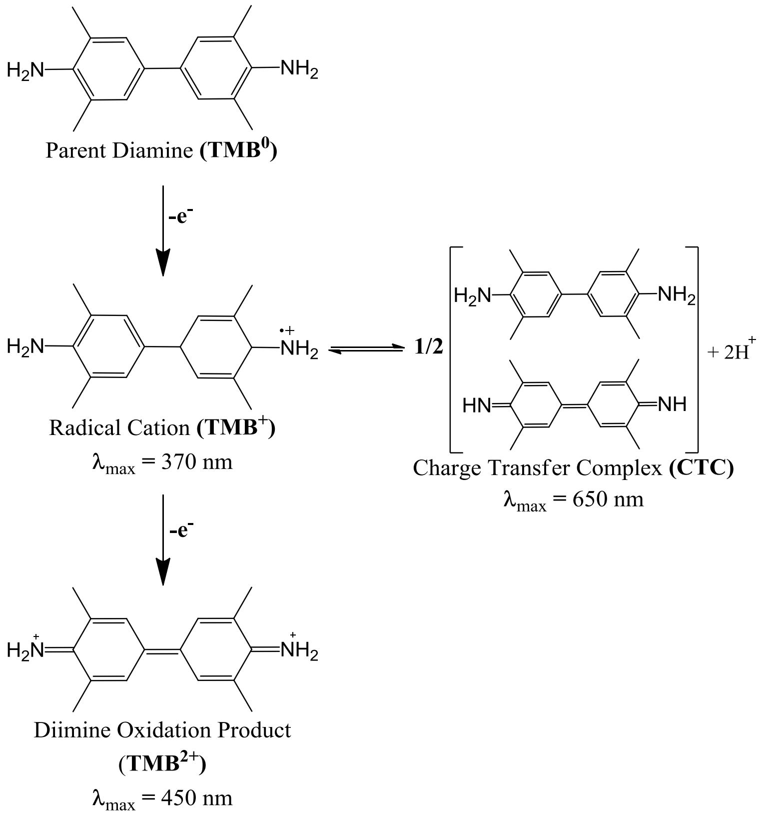

Scheme 3.1. *Reaction scheme for the HRP catalysed oxidation of TMB by H_2O_2.*

As well as its chromogenic properties, TMB is also electroactive and has thus been utilised as an electrochemical substrate. Volpe *et al.* investigated TMB as an electrochemical substrate for direct detection of HRP and achieved a lower detection limit of 8.5×10^{-14} M.[122] They compared three substrates, TMB, hydroquinone and *p*-aminophenyl phosphate (PAPP), and concluded that TMB was the best for low level detection of HRP and gave comparable results to those obtained when using PAPP for ALP detection. Fanjul-Balado *et al.* also made use of its electrochemical properties and applied amperometric detection to a conventional ELISA system for the detection of HRP at levels as low as 2×10^{-14} M. They also used the system indirectly for the quantification of the protein interleukin-6 (IL-6) in the range 3.12 to 300 pg/mL.[123] Electrochemical monitoring of the system was further utilised by Baldrich *et al.* in their development of an amperometric biosensor for detection of HRP/H_2O_2 to levels as low as 6 fM HRP or 5.4 μM H_2O_2.[124] Although the electrochemical methods give good detection limits, simple instrumentation and low production costs, they also show limitations such as variability between arrays, random surface coverage and the inconvenience of having to activate the electrode between steps.[123-124] Furthermore, the presence of large-sized anions commonly found in patient test samples such as heparin and DNA have been shown to affect the electro-oxidation of TMB.[125]

3.2 HRP Catalysed Oxidation of TMB in Solution

Previous studies on the oxidation of TMB have resulted in many proposed mechanisms for the reaction. Early work by Josephy *et al*. used optical and spin resonance spectroscopy to study the oxidation by a range of peroxidases.[126] They achieved an electron spin resonance signal corresponding to a radical cation and a shift in optical spectra upon dilution, indicative of a charge transfer complex (CTC). Marquez and Dunford monitored reaction kinetics and showed for the first time that the oxidation of TMB by peroxidase proceeds via a two-step two-electron oxidation.[127] Misono *et al.* used resonance Raman and absorption spectroscopies to study the electrochemical oxidation processes of TMB in organic solvents.[128]

In the work reported here, the HRP catalysed oxidation of TMB by hydrogen peroxide was first monitored using absorption spectroscopy before studying the spectral changes by Raman scattering.

3.2.1 Monitoring the Reaction by UV/Visible Absorption Spectroscopy

In order to gain a better understanding of how the oxidation reaction proceeds, UV/Vis spectroscopy was employed to monitor the reaction over time, as the two coloured products are generated. After mixing the TMB substrate solution with the enzyme, UV/Vis extinction spectra were collected every 5 minutes in order to monitor the oxidation reaction. Figure 3.2 (a) shows the spectra obtained over the first 20 minutes. It can be observed here that two absorption bands have appeared around 370 nm and 650 nm, which are increasing over time. The appearance of these two new absorption bands can be attributed to the formation of the one-electron oxidation product, where the absorption band at 650 nm is assigned exclusively to the CTC, with an extinction coefficient of 3.9 x 10^4 M^{-1} cm^{-1}.[126]

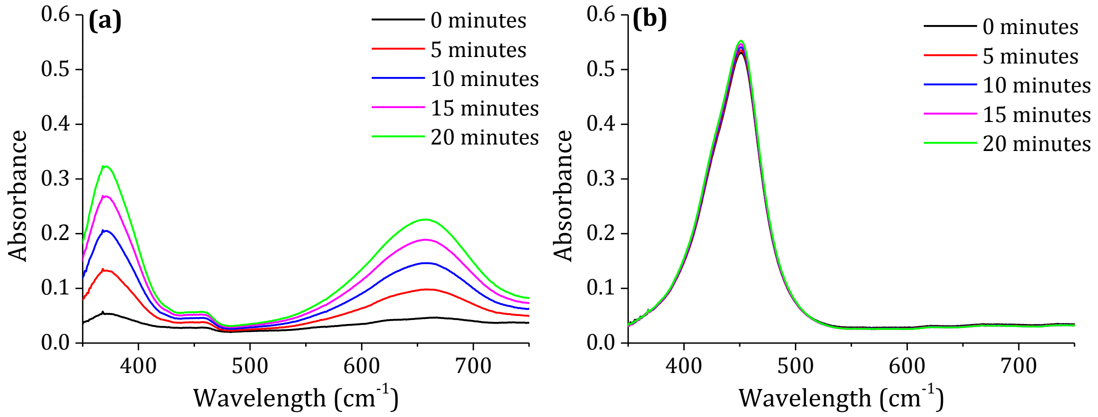

Figure 3.2. ***(a)*** *Extinction spectra of the TMB/H_2O_2/HRP reaction mixture for the first 20 minutes of the oxidation reaction and for a further 20 minutes after the addition of H_2SO_4 stop solution* ***(b)****.*

After the addition of stop solution (H_2SO_4), the reaction was monitored for a further 20 minutes and the resulting spectra are shown in Figure 3.2 (b). As the equilibrium is pushed to the right and the yellow diimine oxidation product is formed, a new absorption band appears at around 450 nm (ε_{450} = 5.9 x 10^2 M^{-1} cm^{-1}) which varies little with time. The bands around 370 nm and 650 nm have also disappeared as the two-electron oxidation product is formed.

In Figure 3.2, the H_2SO_4 stop solution was added after 20 minutes, as indicated in the ELISA procedure. This allowed the two-step oxidation process to be monitored as it would occur in the standard ELISA. Simultaneously, the reaction was also monitored for the final 20 minutes, without the addition of stop solution, to further monitor the production of the one-electron oxidation product. Figure 3.3 is a plot of the absorbance versus time for the two bands arising from the one-electron oxidation product, at 370 nm and 650 nm.

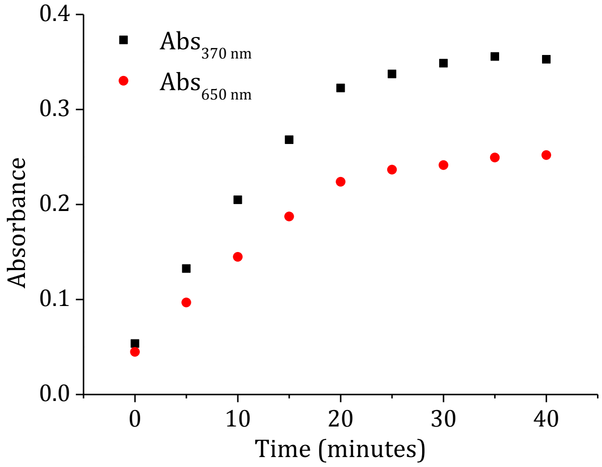

Figure 3.3. *Plot of absorbance versus time for the bands at 370 nm (black) and 650 nm (red) arising from the one-electron oxidation product of TMB.*

For the first 20 minutes as the one-electron oxidation product is formed, it can be observed that there is a linear increase in absorbance for both of the bands (Figure 3.3). Although the absorbance continues to increase after 20 minutes, this is at a much lesser rate and is beginning to level off, indicating that there is little further oxidation after 20 minutes. For this reason, in all further experiments, the TMB was left to incubate for 20 minutes before analysis of the blue CTC.

3.2.2 Resonance Raman Study of TMB Oxidation

In order to investigate the possibility of resonance enhancement, Raman spectroscopy was used to study spectral changes using two visible laser excitation wavelengths, 514 and 633 nm. UV/Vis analysis was carried out in tandem and the resulting spectra can be seen in Figure 3.4 (a). Figure 3.4 (b) and Figure 3.4 (c) show the Raman spectra of the one-electron and two-electron oxidation products, respectively.

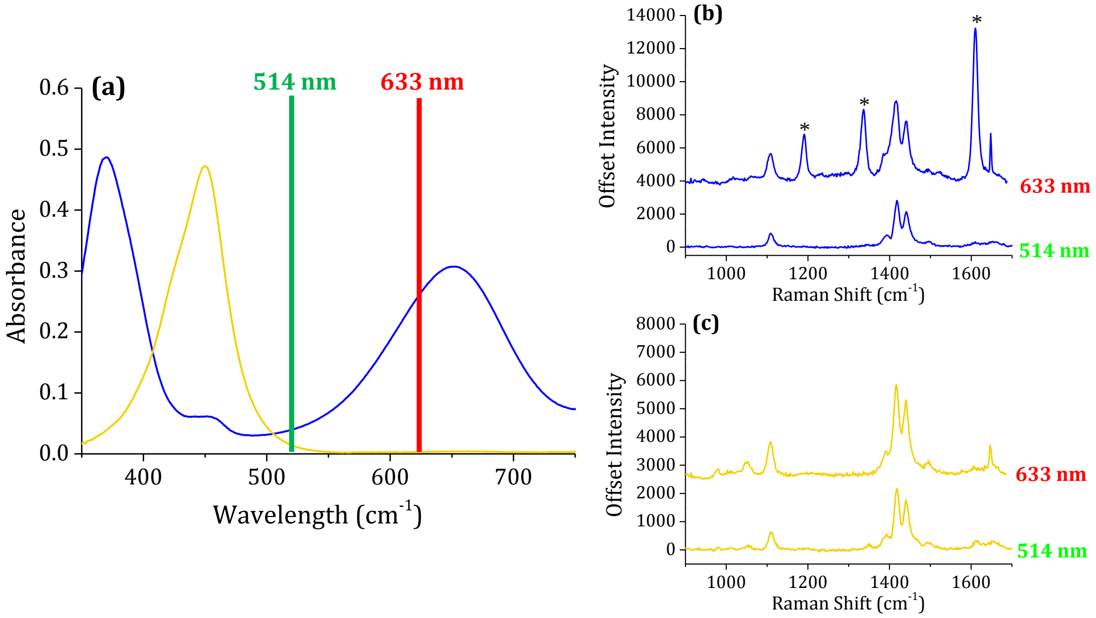

Figure 3.4 (a) *Extinction spectra of the one- (blue) and two-electron (yellow) oxidation products of* TMB^0 *by* H_2O_2. ***(b)*** *Raman spectra of the one-electron oxidation product (*TMB^+ *+ CTC) and* ***(c)*** *of the two electron oxidation product (*TMB^{2+}*) at 514 nm and 633 nm. The resonance enhanced Raman bands are marked with asterisks. Raman spectra were obtained using 3 x 3 second accumulations have been stacked using offset Y values for illustration.*

The Raman bands at 1103, 1413 and 1436 cm^{-1} remained constant throughout all of the spectra. These can be attributed to an excess of the parent diamine (TMB^0) which remains unoxidised in solution. However, when the laser wavelength is tuned in resonance with the lower energy transition (CTC) of the one-electron oxidation product, the bands at 1191 cm^{-1}, 1336 cm^{-1} and 1609 cm^{-1} are selectively enhanced. A very slight enhancement is visible for the two-electron oxidation product at 514 nm but no enhancement is observed at this non-resonant wavelength for the one-electron oxidation product. This is also the case for the two-electron oxidation product at 633 nm where no resonance enhancement is observed. These results are consistent with the spectra observed in Figure 3.4 (a) where the excitation wavelength (633 nm) is near the absorption maximum of the CTC and therefore it would be expected that peaks associated with this complex should be resonance enhanced. In Figure 3.2 (b), a very sharp band is present around 1650 cm^{-1} in the spectrum obtained using 633 nm laser excitation. This band was only observed in certain instances and is similar in nature to a cosmic ray. Since cosmic ray removal occurs when carrying out multiple accumulations, this band is suspected to arise from an issue with the filters.

3.2.2.1 Computational Studies

Although the RRS spectrum of the lower energy transition (CTC) hadn't previously been been reported, RRS of the electrochemical processes of TMB in organic solvents was previously studied by Misono *et al.*[128] However, these were only probed using a 488 nm laser excitation wavelength, which was not in resonance with the CTC but with the TMB^{2+}. They achieved similar spectra to those obtained in this work with shifts in frequency which can be attributed to the electron rearrangement between the one-electron and two-electron oxidation products. Resonance Raman studies of monocation radicals of similar compounds such as benzidine (BZ) and N,N,N′,N′-TMB (N-TMB) have also been reported previously.[129-130]

Computational studies were carried out by Dr. Jörg Saβmannshausen to calculate the theoretical Raman frequencies of the CTC species. The calculated frequencies were in good agreement with the bands observed experimentally, and these were used to tentatively assign the resonance enhanced bands as the following: CH_3 bending modes (1191cm^{-1}), inter-ring C-C stretching modes (1336cm^{-1}), and combination of ring stretching and CH bending modes (1609cm^{-1}).

3.3 Quantification of TNF-α by Resonance Raman Spectroscopy

After observing a strong resonance enhancement when probing the CTC at 633 nm, experiments were carried out to determine whether this enhancement showed concentration dependence. If such a relationship existed it would be possible to quantify the amount of analyte in a sample using this sensitive and selective method. TNF-α was selected as the analyte of interest for initial experiments.

TNF-α is a pro-inflammatory cytokine produced by macrophages in response to infection, injury or cancer. As well as its role in inflammation, TNF-α has been known to induce apoptosis and necrosis and has therefore been utilised as a tumour fighting agent.[131]

TNF-α is primarily produced as a 26 kDa pro-peptide transmembrane protein consisting of 233 amino acids.[132] This membrane-bound precursor is cleaved by TNF-α-converting enzyme (TACE) to release the soluble form of the inflammatory cytokine.[133] Soluble TNF-α exists as a homotrimer made up of three 17 kDa subunits.[132] Each subunit consists of 157 amino acids which form elongated, anti-parallel β-pleated sheets. The three monomers are associated about a three-fold axis of symmetry to form a compact bell-shaped trimer.[134] Both forms of TNF-α are biologically active, the transmembrane form works via cell-to-cell contact and the soluble form acts at the sites of secretion.[135]

Despite its various benefits, TNF-α is known to play a significant part in chronic inflammatory diseases such as rheumatoid arthritis,[136] psoriasis[137] and Crohn's disease[138] as well as conditions such as septic shock syndrome,[139] diabetes[140] and pre-eclampsia.[141] Sensitive detection of the biomarker is therefore important for the diagnosis and treatment of these illnesses. Furthermore, cytokines function in a network, relying on the up-regulation and down-regulation of multiple cytokines simultaneously to achieve a particular physiological effect, thus making them ideal analytes for multiplexed analysis.[17] Although the most common clinical method for the detection of TNF-α is by conventional ELISA, levels of the cytokine have been reported which are below the detection limit of this method. For example, Urszula *et al.*[141] reported increased levels of TNF-α in serum from 0.7 ± 0.3 pg/mL in healthy pregnant women to 1.5 ± 0.7 pg/mL in women with pre-eclampsia. These low levels of the cytokine would not be detectable by a conventional ELISA kit. Furthermore, a recent study involving healthy individuals found that 50 of the 58 samples were below the detection limit of the assay (2 pg/mL) and therefore could not be quantified.[142] A method which offers a lower detection limit than that of the conventional test would therefore be advantageous.

Using the commercial ELISA kit described in section 2.1.4, the sandwich ELISA was carried out on a standard dilution series of the TNF-α and, using a 633 nm laser excitation wavelength, Raman spectra were collected of the CTC resulting from each well. As a control measure, Raman spectra were also collected for the TMB^0 alone, the H_2O_2 solution and the substrate mix ($TMB^0 + H_2O_2$). The spectra of these controls are shown in Figure 3.5 where the blank reaction from the ELISA described above is also included for comparison.

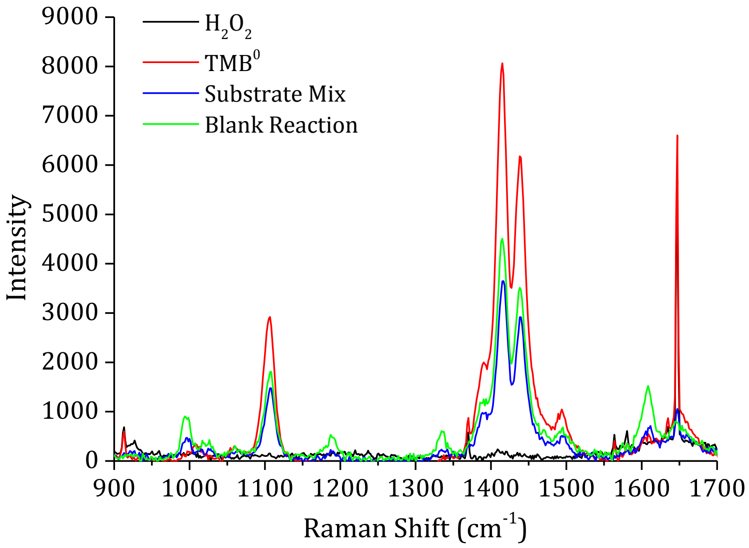

Figure 3.5. *Raman spectra of the four controls: a blank reaction, the TMB/H_2O_2 substrate mix and the two components of the substrate solution (H_2O_2 and TMB^0) at 633 nm laser excitation wavelength using 3 accumulations, each lasting 3 seconds. The blank reaction is the product of an ELISA where BSA was added in place of TNF-α and the CTC was analysed after 20 minutes of TMB incubation.*

In Figure 3.5 it is evident that the blank reaction and the substrate mix give very similar spectra as would be expected, except that in the blank reaction the three enhanced peaks are slightly more intense. This can be attributed to some non-specific binding causing the oxidation to begin without the presence of TNF-α and therefore a very small amount of the CTC being detected. For the TMB^0

however, these three peaks are not enhanced and the peaks at 1103, 1413 and 1436 cm^{-1} are more intense than in the substrate mix or in the blank reaction. This is consistent with the conclusion drawn in section 3.1.2 that these arise from the TMB^0 and are present in the other samples due to an excess left over unoxidised. No significant Raman signal was obtained from the H_2O_2.

Raman spectra of the one-electron oxidation product from each concentration of TNF-α (0 – 2000 pg/mL) were then obtained using a 633 nm laser excitation wavelength. The resulting spectra can be observed in Figure 3.6 below where the three resonance enhanced peaks at 1191, 1336 and 1609 cm^{-1} (indicated by arrows) are shown to increase in intensity with increasing concentration of TNF-α.

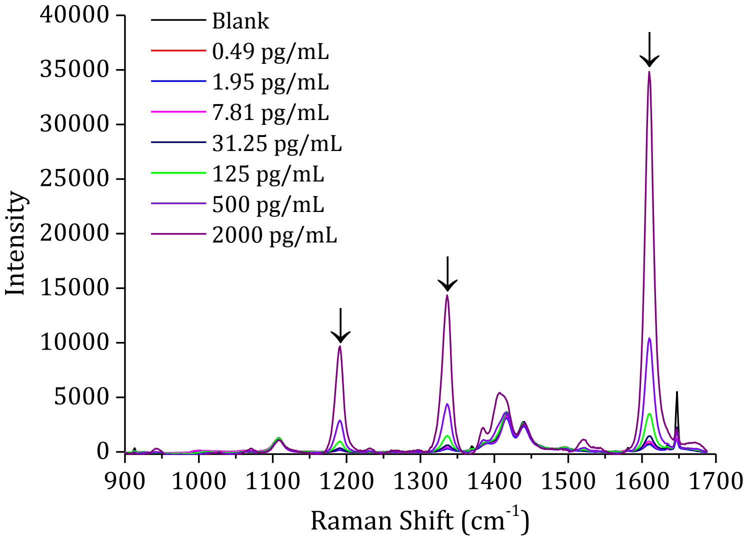

Figure 3.6. *Raman spectra of the CTC from the ELISA of a TNF-α standard dilution series (0 – 2000 pg/mL) collected after 20 minutes TMB incubation. Arrows indicate the position of the three resonance enhanced peaks. Raman spectra were obtained using a 633 nm laser excitation and 3 x 3 second accumulations.*

The intensity of the three resonance enhanced bands was plotted against the concentration of TNF-α and the resulting plots are shown in Figure 3.7 (a), Figure 3.7 (b) and Figure 3.7 (c). It is evident that the resonance enhancement is proportional with increasing concentration of TNF-α and therefore the method can be used for quantification of the cytokine. All three of the resonance enhanced peaks show a direct linear relationship with a good correlation coefficient, R^2 near unity. Furthermore, the range tested here was extended further than that of the standard ELISA which indicates that the dynamic range of the resonance Raman assay could be larger.

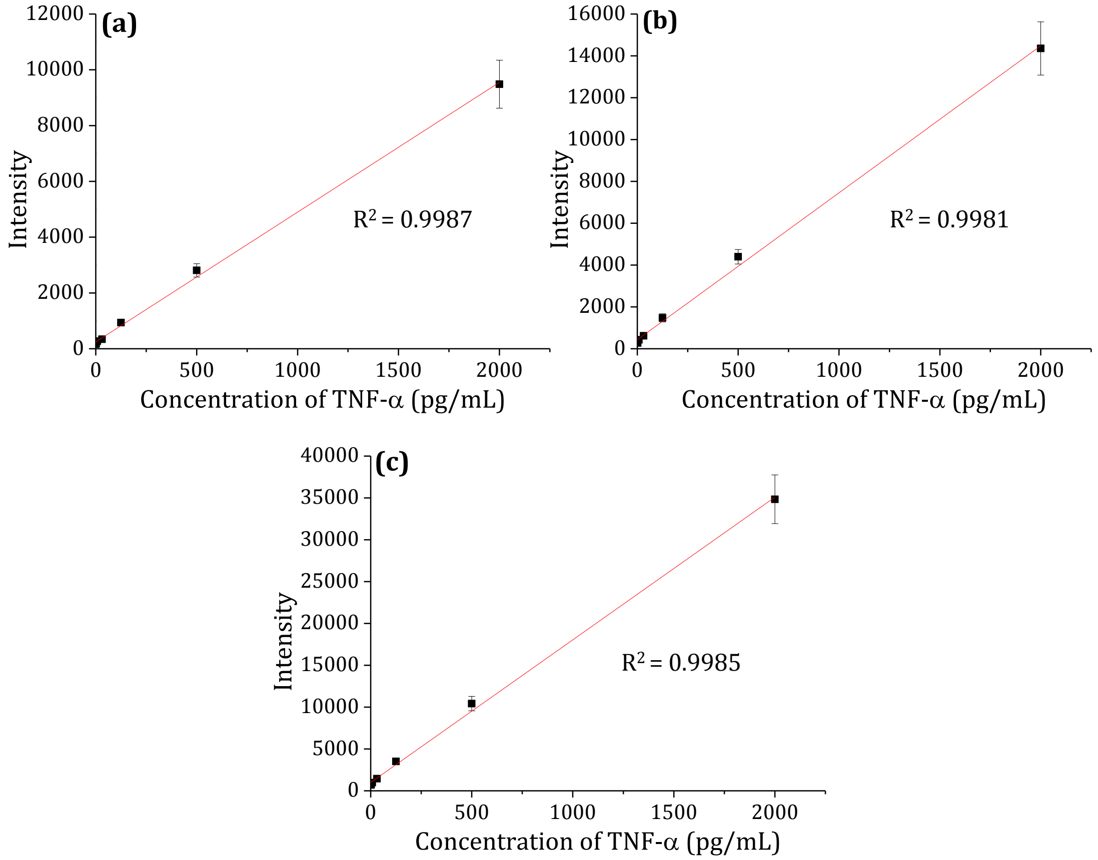

Figure 3.7. *Plot of concentration versus intensity for the three resonance enhanced peaks at 1189 cm*$^{-1}$ ***(a)****, 1336 cm*$^{-1}$ ***(b)*** *and 1609 cm*$^{-1}$ ***(c)****. Graphed values are the mean intensity of three scans of three replicas with the error bars representing standard deviation.*

The concentration versus intensity plots were used to calculate the lower detection limit of the assay which was equal to the mean value of the blank plus twice the standard deviation. This calculation was used as this is the method described to obtain the detection limit in the Quantikine TNF-α ELISA protocol. The values obtained were as follows: 0.097 pg/mL for the peak at 1191 cm^{-1}, 4.17 pg/mL for the peak at 1336 cm^{-1} and 4.79 pg/mL for the peak at 1609 cm^{-1}. Since the detection limit for the band at 1191 cm^{-1} was below the range tested, a further experiment was conducted which focused on the lower end of the range. A standard dilution series (0 -200 pg/mL) of TNF-α was applied to the ELISA and Raman spectra collected (Figure 3.8) of the resulting blue products. It can be observed here that the three resonance enhanced peaks (1191, 1336 and 1609 cm^{-1}) increase in intensity with increasing concentration of the cytokine. The inset shows the peak at 1191 cm^{-1} for the blank control, the 0.049 pg/mL TNF-α standard and the 0.195 pg/mL standard. This demonstrates the precise sensitivity and the ability to differentiate between samples, even at extremely low concentration.

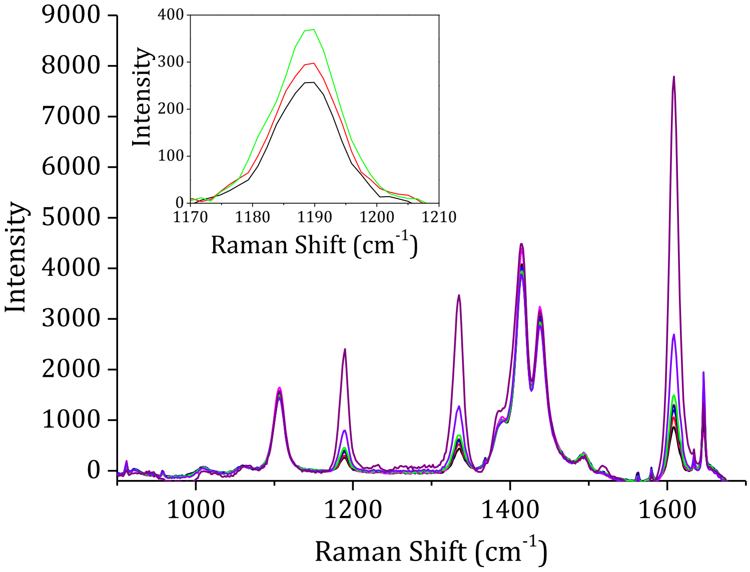

Figure 3.8. *Resonance Raman spectra of the ELISA product of a series of TNF-α standards (0 - 200 pg/mL) at 633 nm laser excitation. The inset shows the peak at 1191 cm^{-1} for the blank control (black), the 0.049 pg/mL TNF-α standard (red) and the and the 0.195 pg/mL TNF-α standard (green). Spectra were obtained using 3 x 3 second accumulations.*

Given that the peak at 1191 cm^{-1} gave the lowest detection limit, this was selected for quantifying the cytokine in subsequent work. Figure 3.9 (a) shows the concentration versus intensity plot based on the peak at 1191 cm^{-1} for the lower concentration range. Absorbance measurements were also taken in parallel so that the RRS method could be compared with the traditional colorimetric method of detection, the resulting absorbance versus intensity plot is shown in Figure 3.9 (c).

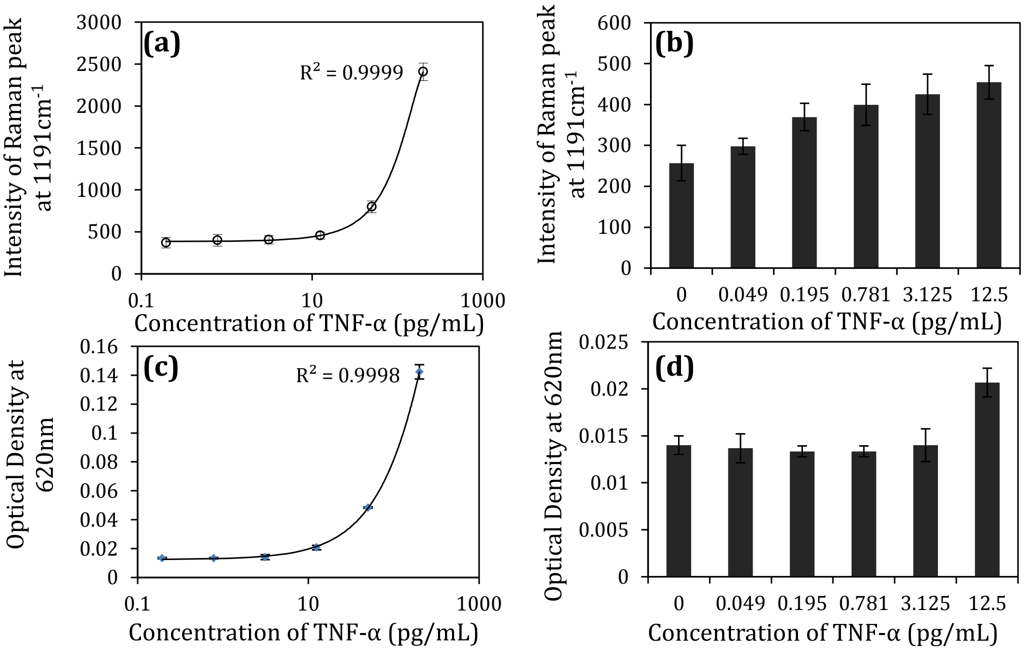

Figure 3.9 (a) *Concentration versus intensity plot based on RRS peak at 1191 cm^{-1} and* ***(c)*** *concentration versus intensity based on absorbance values at 620 nm for the same concentration range (0-200 pg/mL) of TNF-α.* ***(b)*** *and* ***(d)*** *show the corresponding intensities at the lower end of the concentration range for the RRS and absorbance methods, respectively.*

The detection limit for the RRS method was recalculated using the plot in Figure 3.9 (a) and the value obtained was 90 fg/mL, which is in good agreement with the resultant value from the previous calculation. The plot in Figure 3.9 (c) was used in the same way to calculate the detection limit for the absorbance method, which was 4.50 pg/mL. Resonance Raman scattering therefore offers a 50-fold improvement in detection limit compared to that of the conventional method. The intensity of the Raman band at 1191 cm^{-1} for the TNF-α standards at the lower end of the concentration range can be observed in Figure 3.9 (b). A linear increase in peak intensity with increasing concentration of TNF-α was observed, with the exception of the 0.049 pg/mL TNF-α standard. This indicates that the lower detection limit of the assay lies between 0.049 pg/mL and 0.195 pg/mL, which correlates well with the calculated limit. Similarly, the optical density values obtained using the absorbance method for the low end of the concentration range can be found in Figure 3.9 (d). This chart shows that, using the absorbance method, it is not possible to distinguish between the standards of low concentration and the blank control and that the detection limit lies between 3.125 pg/mL and 12.50 pg/mL. Again, this is in good agreement with the calculated limit of detection.

In order to compare the two methods for detecting and quantifying TNF-α in the presence of serum proteins and other cytokines, the amount of TNF-α in controls containing a mixture of thirteen recombinant human cytokines at low, medium and high levels was measured using both RRS and colorimetric detection. Table 3.1 shows the resultant values for each method along with the expected value range which is calculated by the manufacturer using colorimetric detection of TMB^{2+} with the same ELISA kit as used in this work.

Table 3.1. *TNF-α concentrations present in low, medium and high controls obtained using both RRS and colorimetric detection methods.*

Control	**Colorimetric Detection CTC 620 nm (pg/mL)**	**Colorimetric Detection TMB^{2+} 450 nm (pg/mL)**	**Resonance Raman CTC 633 nm (pg/mL)**	**Expected Value Range (±3 s.d.) (pg/mL)**
Low	105.17 ± 5.20	100.10 ± 3.77	111.41 ± 6.84	88 – 154
Medium	330.17 ± 18.93	312.81 ± 17.33	408.94 ± 15.56	235 – 411
High	669.33 ± 30.14	638.85 ± 24.72	734.57 ± 93.22	484 – 762

Since all of the values were within the expected value range, it appears that resonance Raman spectroscopy is a suitable method for quantifying a specific target from a serum mixture. The ability of the method to quantify the TNF-α was not affected by the presence of other cytokines which provides evidence towards the selectivity of the method.

3.3.1 Analysis of Human Blood Samples

To assess the compatibility of the RRS detection for its use in a clinical situation, the blood serum of eight patients diagnosed with rheumatoid arthritis (RA) was analysed for the quantification of TNF-α with absorbance measurements also taken in parallel. Table 3.2 shows the values obtained for each sample using both colorimetric detection and RRS.

Table 3.2. *TNF-α concentrations present in blood serum of eight RA patients, obtained via colorimetric detection and resonance Raman scattering of ELISA products.*

Patient	Colorimetric Detection (pg/mL)	Resonance Raman Spectroscopy (pg/mL)
1	13.27 ± 1.15	13.34 ± 3.88
2	12.76 ± 1.35	12.59 ± 2.47
3	13.52 ± 1.56	18.42 ± 4.05
4	12.50 ± 0.66	17.19 ± 4.16
5	12.88 ± 0.77	18.06 ± 2.13
6	12.12 ± 0.77	13.37 ± 0.58
7	10.70 ± 0.89	14.67 ± 2.52
8	11.47 ± 1.97	11.77 ± 1.91

The colorimetric detection method used in this experiment is what would normally be used to analyse clinical samples. Since RRS gave comparable results to the colorimetric detection, it proves that this method is also suitable for the quantification of TNF-α in human blood serum. Although there are a few discrepancies in the results, these can be attributed to the instrumental setup and the time delay between collecting Raman scattering measurements. In the colorimetric detection method each reading is taken simultaneously using a microplate reader, whereas in the RRS method, measurements were taken one after the other by focusing the microscope in each separate well and moving the plate manually between samples. The consequent time delay in this approach could also allow for further oxidation of the CTC complex into the non-resonant TMB^{2+} species. This can account for the larger standard deviation found in some cases when the conventional method is replaced with RRS. Certain measures could be applied to overcome these issues. For example, a stop solution is now available for stopping the reaction at the blue CTC and Raman plate readers are also commercially available which would allow the samples to be analysed simultaneously, in the same way as the absorbance measurements. Although these improvement measures were not deemed necessary for the purpose of this work, this is something that could certainly be considered for using the assay in a clinical scenario.

3.3.2 Further Enhancement by SERRS

To further enhance the Raman spectra and subsequently further increase the sensitivity, SE(R)RS was investigated to replace RRS. Initially, the ELISA was carried out on the standard dilution series and the Raman spectra were collected with (SERRS) and without (RRS) the presence of citrate reduced gold colloid (Figure 3.10).

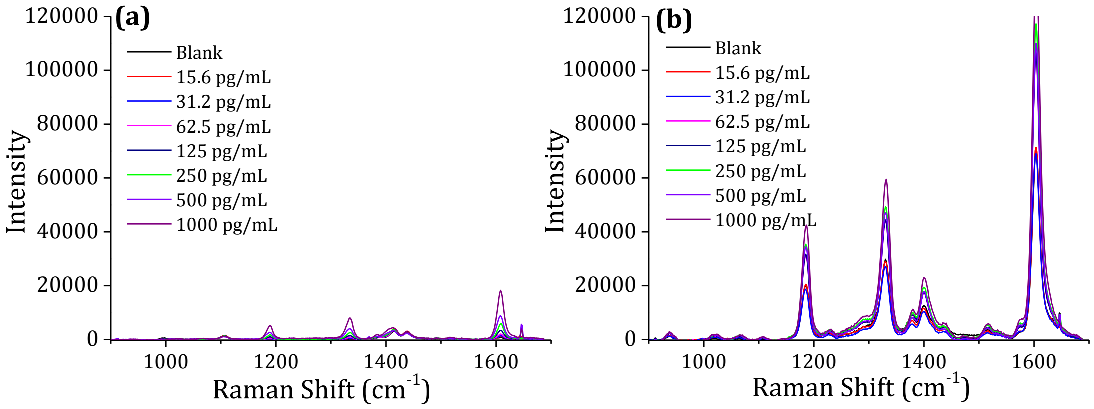

Figure 3.10. *Raman spectra of the ELISA products from a standard dilution series of TNF-α without* ***(a)*** *and with* ***(b)*** *citrate-reduced gold colloid. Spectra were obtained using a 633 nm laser excitation wavelength and 3 x 3 second accumulations.*

As can be observed in Figure 3.10, the Raman signal is further enhanced by the presence of gold colloid giving a much more intense signal. This enhancement however, is random and inconsistent and there is no direct relationship between concentration of TNF-α and peak intensity (Figure 3.11).

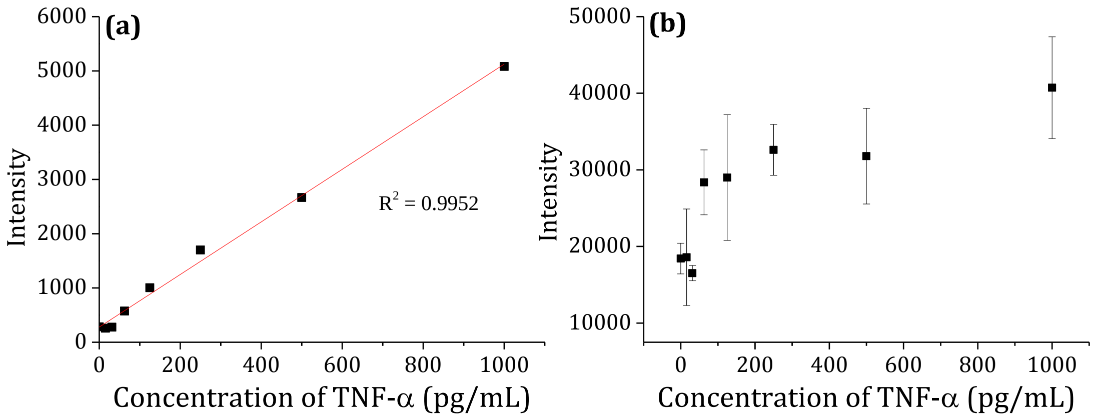

Figure 3.11. *Concentration versus intensity plots based on the peak at 1191 cm^{-1} for the Raman spectra* ***(a)*** *without and* ***(b)*** *with gold colloid collected with 633 nm laser excitation.*

In Figure 3.11 (a) where there is no gold colloid present, a direct linear relationship is observed between the concentration of TNF-α and the peak intensity at 1191 cm^{-1}. This is consistent with all of the previous results using RRS. On introduction of gold colloid (Figure 3.11 (b)) the linearity is lost and the enhancement is no longer proportional to the amount of analyte present, meaning that quantification using this method would not be possible without further optimisation.

Initially it was suspected that the random and inconsistent enhancement arose from over-aggregation of the samples. However, various conditions were altered in attempt to reduce this and to optimise the system but it became apparent that SE(R)RS was not suitable for quantification in this assay and that RRS was a more reliable method.

3.4 Adaptability of the Detection Method for Alternative ELISAs

Since the resonance Raman detection method was applied directly to a conventional ELISA kit, without modification of the assay itself, it was envisaged that this could be applied for the detection of any biomarkers using a TMB-based assay. Furthermore, it may be possible to adapt the system to assays using alternative substrates, such as ABTS. These ideas were investigated to test the versatility of this novel detection system for the application to various types of ELISA.

3.4.1 Detection of Prostate-Specific Antigen by a Resonance Raman ELISA

Prostate-Specific Antigen (PSA) is a 34 kDa, 237 amino acid glycoprotein of the kallikrean-related peptidase family. Although present in semen in its free form, PSA is present in serum mainly in complex form with α1-antichymotrypsin. PSA is a serine protease which has chymotrypsin-, trypsin-, and esterase-like activities and is responsible for liquefaction of the seminal coagulum in male ejaculate.[143]

PSA is currently the most important biomarker for detection and management of prostate cancer. It was purified and characterised by Wang *et al.*[144] in 1979 as a marker for prostatic tissue, present only in the prostate, hence the name PSA. Subsequently, PSA was identified and quantified in serum[145] and later used clinically as a marker of prostate cancer.[146]

Previously, prostatic acid phosphatase (PAP) was the gold standard for diagnosis and monitoring of prostate cancer. However, the lack of sensitivity and unpredictable fluctuations in serum levels for PAP make PSA more sensitive, specific and precise and thus more favourable.[147] Despite this, care must still be taken when using PSA as a prostate cancer marker as elevated levels of PSA are also observed in conditions such as benign prostatic hyperplasia (BPH).[148]

More recently, PSA has also been linked to breast cancer and hence simple, specific and sensitive detection of this biomarker is clearly advantageous.[149-150] However, the low detection levels required for early diagnosis are below the limits of many assays and so improvement in these detection limits is required.[151]

As opposed to the ELISA kit which was used in section 3.3 for the detection of TNF-α, the PSA assay was developed using a DuoSet. The main difference here is that the assay does not come with pre-coated well plates, but instead the capture antibody is provided and wells are coated in-house as part of the process. Aside from the coating of the wells with capture antibody, the rest of the sandwich assay is carried out in the same way using antibodies specific to PSA rather than TNF-α. Therefore, experimental conditions are similar to those described previously and, since the enzyme/substrate system is still HRP/TMB, the detection method optimised in the preceding section can be directly applied.

The wells of high-binding polystyrene plates were coated with PSA capture antibody and the sandwich ELISA was subsequently carried out using a PSA standard dilution series (0 – 60 ng/mL). After development of the TMB for 20 minutes to form the blue CTC, the Raman scattering of each sample was collected using a 633 nm laser excitation wavelength. The spectra of the blank control and of the 60 ng/mL PSA standard can be observed in Figure 3.12.

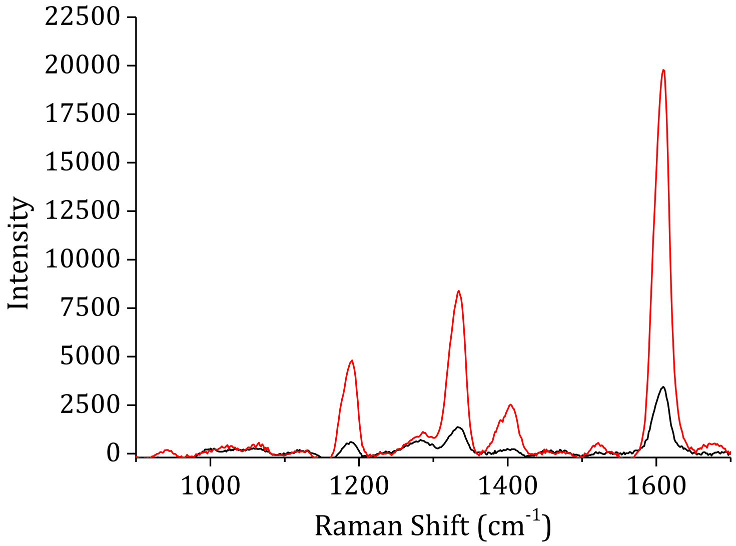

Figure 3.12. *Raman spectra of the ELISA product of the 60 ng/mL PSA standard (red) and the blank control (black). Spectra of the blue CTC were collected using a 633 nm laser excitation wavelength with 3 x 3 second accumulations.*

Although the spectra in Figure 3.12 are similar to those obtained previously, there are some distinct differences, particularly in the bands around 1400 cm^{-1}.

These spectral differences arise not from the analysis of a different analyte but rather that a different TMB solution has been used for this assay. The TMB used previously was part of the TNF-α ELISA kit whereas the solution which was applied this time round was a separate TMB solution, optimised for analysis of the blue CTC. This TMB also comes ready to use as opposed to the previous solution which is supplied as two separate reagents, TMB and H_2O_2, to be mixed before use in the assay. Therefore, the solution must be stabilised to prevent oxidation beginning in the bottle and thus the formulation is slightly different. The changes in the spectra when using this alternative TMB solution also supports the assignment of these non-enhanced bands to the parent TMB leftover in solution, as previously suggested, with the spectral differences between the two formulations arising from the changes in the surrounding environment.

Nonetheless, despite the slight differences in the non-resonant bands, the three resonance enhanced peaks remain in the same positions and are still resonance enhanced. Therefore, quantification of the PSA was possible using a plot of PSA concentration versus intensity of the enhanced peak at 1189 cm^{-1} (Figure 3.13).

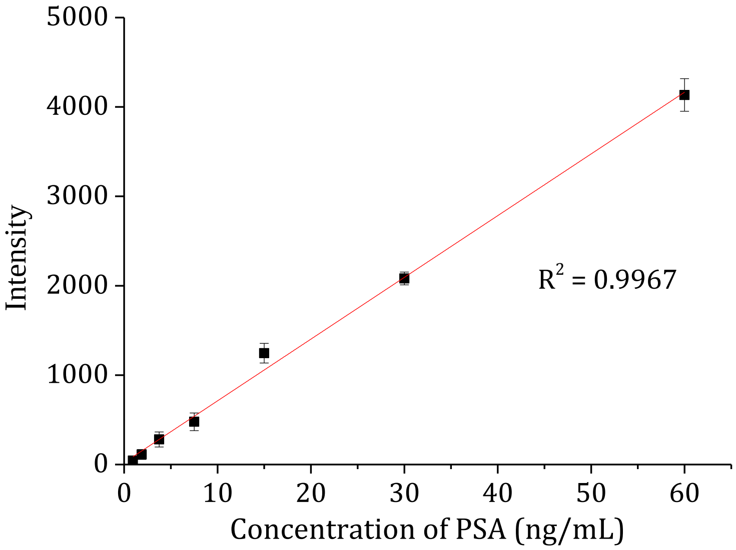

Figure 3.13. *Plot of PSA concentration against intensity of the resonance enhanced Raman band at 1189 cm^{-1}. Plotted values are the average intensity from three scans of three replicates with the error bars representing the standard deviation.*

In Figure 3.13 it is clear that once again a linear relationship could be observed between the concentration of the analyte and the Raman signal. The detection limit of the PSA assay was calculated in the same way as with the TNF-α and the resulting limit was found to be 48.3 pg/mL. This number is comparable with that quoted for the PSA ELISA (69 pg/mL), however, the lack of a major improvement over the colorimetric method in this instance could be attributed to the fact that the assay did not use the fully optimised commercially available ELISA kit. For example, the coating of the wells with capture antibody was carried out in-house and thus optimum coverage may not have been achieved. Therefore, the detection of the two different analytes is not directly comparable though it has still been demonstrated that the detection method can be applied to a variety of biomarkers using TMB-based assays.

3.4.2 Detection Using Alternative Chromogenic Substrates

Resonance Raman has been successfully applied to TMB-based assays for the detection of protein biomarkers. Although TMB is the most popular peroxidase substrate used in ELISAs, alternative chromogenic substrates, such as ABTS, are also available. ABTS is less sensitive than TMB; however, its slower oxidation can be advantageous if, for example, undesirable background signal is a problem. The HRP-catalysed oxidation of ABTS proceeds via Scheme 3.2 to yield a green product which is normally quantified by measuring the absorbance at 405 - 410 nm.

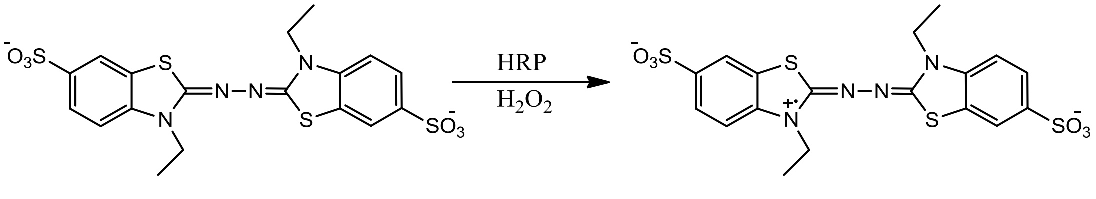

Scheme 3.2. *HRP-catalysed oxidation of ABTS by H_2O_2.*

To investigate how the resonance Raman scattering of ABTS compared with that of TMB for the detection of biomarkers, a brief study was undertaken to compare the performance of the two substrates in a resonance Raman ELISA.

The coloured product was first analysed by UV/Vis spectroscopy and the resulting extinction spectrum is shown in Figure 3.14. The main absorption band can be observed at 414 nm and can be attributed to the green radical anion. Further bands at around 630 nm and 730 nm are also visible, arising from the blue cationic form. For Raman measurements, a laser excitation wavelength of 633 nm was selected as it was suspected that this would be the most likely to give resonance enhancement by coinciding with the absorption of the blue radical cation.

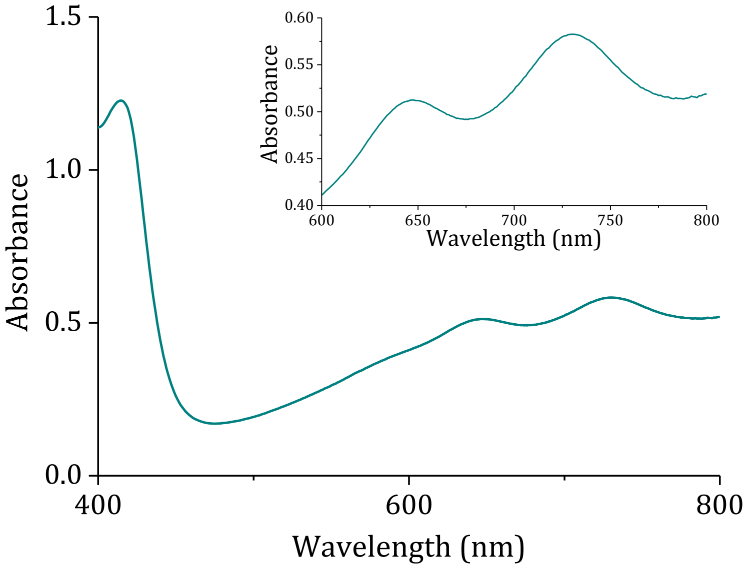

Figure 3.14. *Extinction spectrum of the coloured oxidation product of ABTS.*

Since all of the required reagents were available, the PSA assay was used to study the suitability of ABTS as a substrate in a resonance Raman ELISA. The ELISA was carried out on the standard dilution series of PSA (0 – 60 ng/mL) and ABTS was used as the chromogenic substrate. Raman spectra of the resulting coloured products were obtained at 633 nm laser excitation wavelength. The spectra for the blank control and the 60 ng/mL are shown in Figure 3.15 and it is clear that the spectra obtained from ABTS have more noise than those of TMB and are generally less intense. The inset in Figure 3.15 compares the discrimination of the two substrates indicating that the difference in TMB signal between the blank control and the 60 ng/mL standard is much larger with TMB than when ABTS is used instead. Furthermore, the calculated detection limit using ABTS was 293.4 pg/mL, which is significantly higher than the limit achieved with TMB as the substrate. Although it is known that TMB is more sensitive, it may have been the case that the lesser background of ABTS resulted in improvement over the TMB. However, the larger discrimination and lower detection limit of the TMB-based assay proves that this is not the case. Nonetheless, resonance Raman detection can still be applied to ABTS-based assays with detection possible across the range of the ELISA and with improvement over previous reports using SERS of ABTS for the detection of PSA.[152]

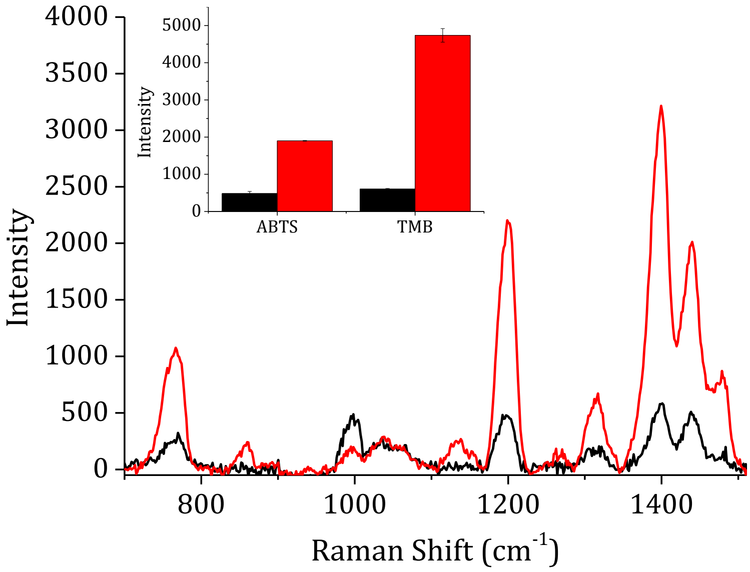

Figure 3.15. *Raman spectra obtained after the ELISA of 60 ng/mL PSA standard (red) and 0 ng/mL of PSA (black) where ABTS is the coloured substrate. The inset compares the discrimination between the blank control and 60 ng/mL of PSA using ABTS and TMB. The discrimination is compared for the band at around 1190 cm^{-1}. All spectra were obtained using 633 nm laser excitation wavelength and 3 x 3 second accumulations.*

Although the resonance Raman detection of PSA using ABTS was inferior to the TMB-based detection, the possibility of improved SERS response using ABTS was considered. The ELISA was carried out in the same way as previously, this time with the introduction of a roughened metal surface in the form of citrate-reduced gold colloid. Raman spectra were obtained and those resulting from the 60 ng/mL PSA sample and the blank control can be observed in Figure 3.16. It is clear here that the spectra have not been enhanced by the addition of the metal surface and that, in fact, the peaks are less well-defined and that the introduction of gold colloid seems to have had a detrimental effect on the overall spectrum of ABTS. The lack of enhancement here when compared to the TMB can be attributed to the opposite charge of the two chromogenic substrates. The positively charged TMB has more of an affinity to the negatively charged nanoparticles than the ABTS does, with its overall negative charge.

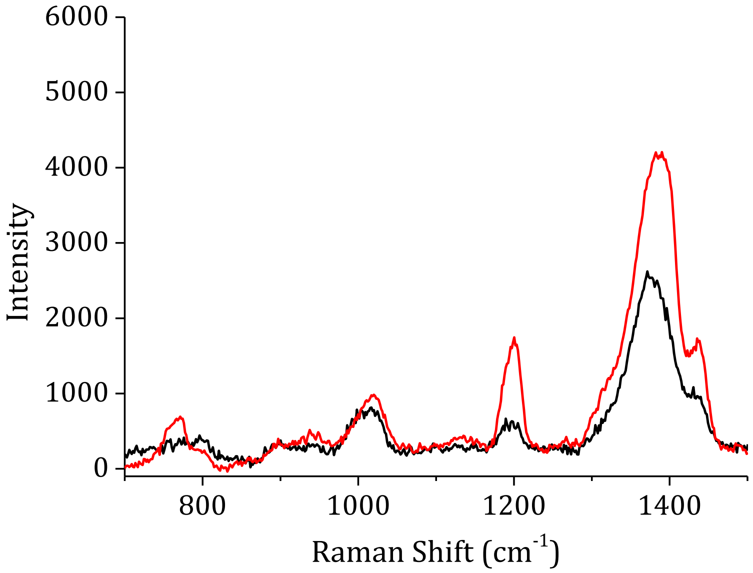

Figure 3.16. *SERRS spectra of ABTS resulting from the ELISA of the 60 ng/mL PSA standard (red) and the blank control (black)*

Although improvements in the SERRS response could be observed, for example with the addition of salt, it was considered that full optimisation of the conditions was not worthwhile for this project as RRS, and also TMB, was better suited for the desired application. Therefore, further investigation into the SERRS of ABTS was not undertaken.

3.5 Concluding Remarks

Resonance Raman scattering has been used for the analysis of chromogenic substrates to replace traditional colorimetric detection in conventional ELISAs. The method was applied to two different substrates to improve the detection limits of the biological assays. TMB-based detection proved to be the most sensitive and the detection limit was improved by up to 50 times when compared to commonly applied methods of detection.

Furthermore, the assay was used for the analysis of human blood serum and results obtained were similar to those of the current clinical method, indicating that the resonance Raman spectra are not affected by the presence of blood serum or other biomarkers.

It was also shown that this detection method is applicable to two key biomarkers, TNF-α and PSA, and it is envisaged that this could be further extended to a variety of other analytes. Additionally, this resonance Raman detection of chromogenic substrates has recently been applied for the detection of DNA thus further proving the versatility of the detection method.[153]

It has been demonstrated that enhancement by RRS can be further improved by using SERRS; however, it appears that quantification is not possible using this method. Although further optimisation of the conditions may have been attempted, it was deemed to be outside the scope of this project. However, optimisation of the conditions was attempted as part of a separate project and it was confirmed that the method would not be suitable for the quantification of analytes. In fact, recent work has found that the nanoparticles themselves catalyse the oxidation of the coloured substrates.[154-155] Therefore, the presence of the analyte is not required for the oxidation to be observed and hence the introduction of nanoparticles is not desirable for the applications presented herein.

4. Immunoassay Arrays Fabricated by Dip-Pen Nanolithography

4.1 Introduction

Although the ELISA is a quick and sensitive method for the detection and quantification of proteins, it suffers from high sample consumption and lack of multiplexing capability.[156] Protein arrays, as discussed previously, can overcome these drawbacks and they have hence become widely investigated for the detection of biomarkers. A previous study showed that DPN could be used for the successful patterning of immunoassay arrays for the detection of PSA.[35] It was envisaged that this patterning could be combined with the sensitivity of resonance Raman scattering to produce a sensitive and robust method for the detection of biomarkers which could eventually be developed into a multiplexed assay for high-throughput analysis.

In an ELISA, the substrate generates soluble products. However, for other methods, such as Western Blots, precipitating substrates are favourable and thus an alternative formulation of TMB is available. In this “blotting” solution the oxidation reaction forms a blue precipitate of the CTC rather than developing a blue colour in solution. It was envisaged that this precipitating TMB may be useful as a substrate in an array format, where the precipitate should form on the protein spots so that the advantages of ELISAs could be combined with the advantages of patterned arrays. Jenison *et al*. previously used this precipitating TMB in an array format for the detection of proteins and DNA.[157] However, they used colorimetric detection and large array spots. It was envisaged here that RRS could be applied for the detection of the TMB, since this achieved good results in solution, and that the spots fabricated by DPN would also improve throughput.

The PSA ELISA investigated previously was adapted to a surface array format using the steps illustrated in Figure 4.1. Capture antibody arrays were printed using DPN and the remainder of the surface was blocked by BSA before adding the PSA standard. A biotinylated detection antibody, specific to PSA, was then added, followed by streptavidin-HRP and finally TMB. On reaction with HRP, the TMB forms the blue CTC as a precipitate in the areas where the spots were printed. Subsequent detection of the blue CTC could be achieved by resonance Raman mapping.

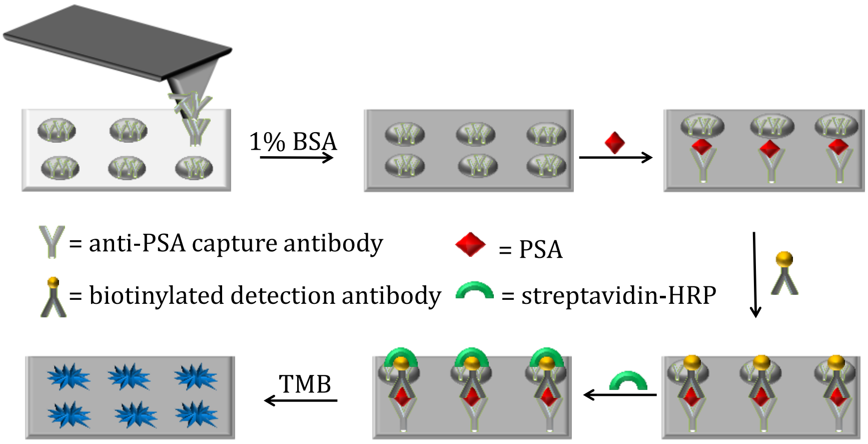

Figure 4.1. *Schematic representation of the assay format adopted in this work. Arrays of PSA capture antibody are printed using the NLP 2000® and the remaining surface is blocked by BSA. PSA standard is added and unbound material washed away before addition of a biotinylated detection antibody. Following another wash step, streptavidin-HRP is added and finally the TMB which will form the blue CTC in localised areas where the spots are printed.*

4.2 Selection of a Suitable Surface for Immunoassay Arrays

Efficient immobilisation is a key factor in determining the success of a protein microarray. As a result, much consideration must be made in selecting a suitable surface for the assay.

With such a diverse range of structural, chemical and biological properties and a nature so labile, it is improbable that any one immobilisation strategy could be universal for proteins. Hence, a broad range of surfaces, with differing immobilisation chemistries, is required for array-based protein analysis. Careful consideration must be made; not only on how effective the immobilisation will be, but also that the protein will avoid denaturation and remain active. It is also vital to minimise the risk of non-specific binding where possible. Furthermore, the suitability of a surface may be affected by the detection technique being employed. Since the detection method being investigated here hadn't previously been utilised with protein arrays, a suitable surface was yet to be established. Therefore, various surfaces were investigated and the results of the assay compared on each.

4.2.1 Epoxysilane Coated Glass

Due to the smooth, flat nature of glass and its low fluorescence background, functionalised glass slides have proved a popular choice as a substrate for protein microarrays. MacBeath and Schreiber[25] showed the capability of such derivatisation by spotting proteins and antibodies onto glass slides which had been pre-treated with an aldehyde-containing silane reagent. The aldehydes react readily with the primary amines on the protein to form a Schiff's base linkage. Subsequent to protein attachment, slides are immersed in a buffer containing bovine serum albumin (BSA) in order to quench the unreacted aldehydes and form a molecular layer which reduces non-specific binding in subsequent steps (Figure 4.2).

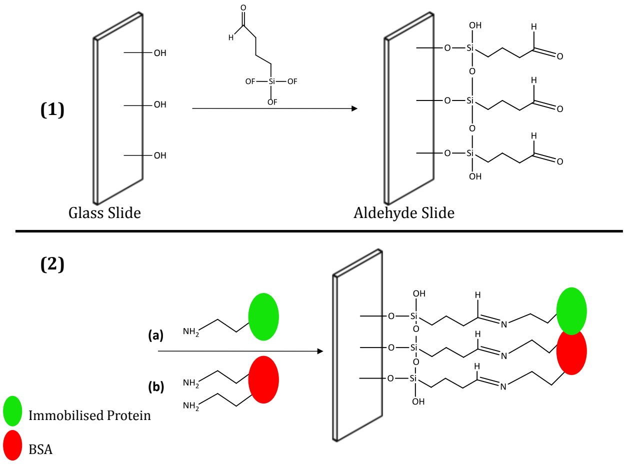

Figure 4.2 *Schematic diagram of the aldehyde functionalisation of a glass slide. Step (1) Glass slide is pre-treated with aldehyde and step (2) (a) attachment of protein to slide via amine groups and quenching of unreacted aldehydes by attachment of BSA (b).*

Epoxysilane coated surfaces, produced in a similar way, have also been utilised and have shown high sensitivity, good signal-to-noise ratios and good spot quality.[158] The high reactivity of the epoxy groups on the surface allows the formation of strong covalent bonds with nucleophilic groups of the amino acid side chains. Figure 4.3 shows an example of how this reaction occurs between primary amines of the proteins and the epoxide groups on the glass slide. A similar reaction can also occur with other nucleophilic groups such as carboxylic acids and occasionally thiol groups from cysteine residues; however, these tend to form disulfide bridges in the tertiary structure of the protein.

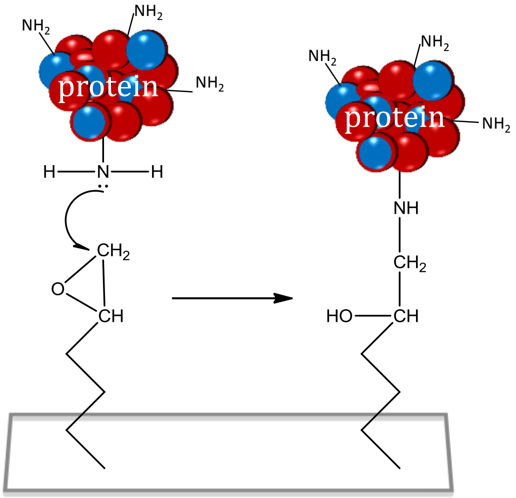

Figure 4.3. *Reaction of epoxide groups on epoxysilane coated glass slides with primary amines of amino acid side chains.*

These epoxysilane coated glass slides have been widely utilised for protein arrays and are thus commercially available. Furthermore, they have been used previously for arrays fabricated using fluorescence detection, providing consistent arrays and good sensitivity.[159]

4.2.1.1 Bulk Spotting PSA Immunoassay on Epoxysilane Glass Slides

Before attempting the PSA immunoassay in a microarray format, the assay was carried out using bulk spotting. This allowed for the verification that the epoxysilane glass was an appropriate surface and that all the components of the assay were in working order; as well as confirmation that the precipitating TMB was suitable as a substrate and that resonance Raman spectra could be obtained similar to previous results with the soluble formulation. Such validation is useful prior to attempting the assay on the smaller scale.

A pipette was used to transfer 0.3 µL of capture antibody onto the glass slides in a "bulk spot" and the immunoassay was carried out as outlined previously. Raman maps were collected using a 633 nm laser excitation wavelength and the results which were achieved for the spot containing 60 ng/mL ((a) and (b)) and for the blank control where no PSA was added ((c) and (d)) can be observed in Figure 4.4.

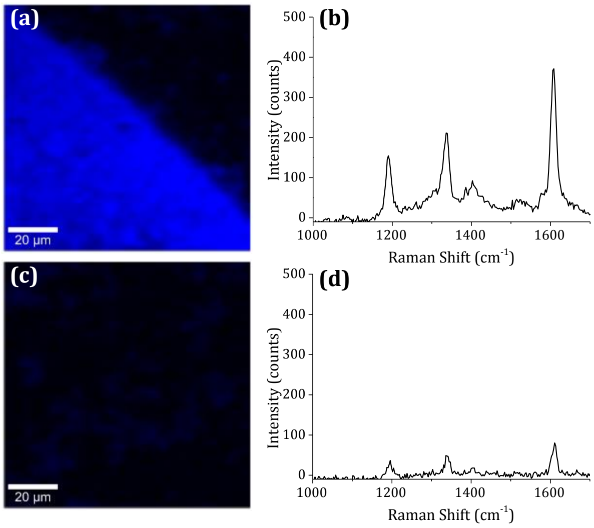

***Figure 4.4 (a)** and **(c)** Raman maps of the bulk spots containing 60 ng/mL and 0 ng/mL of PSA, respectively. **(b)** and **(d)** are the Raman spectra obtained from a point in the corresponding map. Maps were obtained using a 633 nm laser excitation wavelength at 1 µm spatial resolution.*

Figure 4.4 (a) is a false colour image generated with respect to the intensity of the band at 1609 cm^{-1} (Figure 4.4 (b)). The dark areas represent areas of low signal intensity and the bright areas represent areas of higher Raman signal. In this map, the edge of the spot, for the 60 ng/mL sample, is clearly visible thus indicating that the assay was successful. Figure 4.4 (b) shows the Raman spectrum obtained from a randomly selected point in this spot in which the peaks at 1191, 1336 and 1609 cm^{-1} have once again been resonance enhanced using a 633 nm laser excitation wavelength. It is also important to note that the bands at 1103, 1413 and 1436 cm^{-1}, which were clearly visible and well-defined in previous TMB spectra, have reduced significantly in intensity on isolation of the blue CTC. This supports the conclusion drawn previously that these bands could be attributed to an excess of the parent diamine (TMB^0) leftover unoxidised in solution.

Figure 4.4 (c) shows the Raman map taken from the control well where no PSA was added. Although there are patches of precipitate present, no clear spot is observed. The patches indicate that some non-specific binding may have occurred; however, even in the areas where it looks most concentrated, it gave very little Raman signal (Figure 4.4 (d)) and is therefore insignificant.

4.2.1.2 PSA Immunoassay Microarrays on Epoxysilane Glass

Since the assay was successful using bulk spotting it was transferred to the smaller scale where the NLP 2000® was used to print spots of capture antibody onto the surface of the glass slide. Arrays were printed using a 0.1 s dwell time (DT) and spaced 33 µm apart. Each pen of the 12-pen array was programmed to print 2 x 8 spots which resulted in patterns of 24 x 8 spots. Since the pitch between pens is 66 µm, the arrays were equally spaced throughout. The conditions described resulted in spots of about 5 µm in diameter.

The PSA immunoassay was then carried out on a standard dilution series of PSA and Raman spectra were collected from the surface. The area was mapped using Raman imaging in order to determine whether spots could be observed. The Raman maps and corresponding spectra obtained from the 60 ng/mL standard can be observed in Figure 4.5.

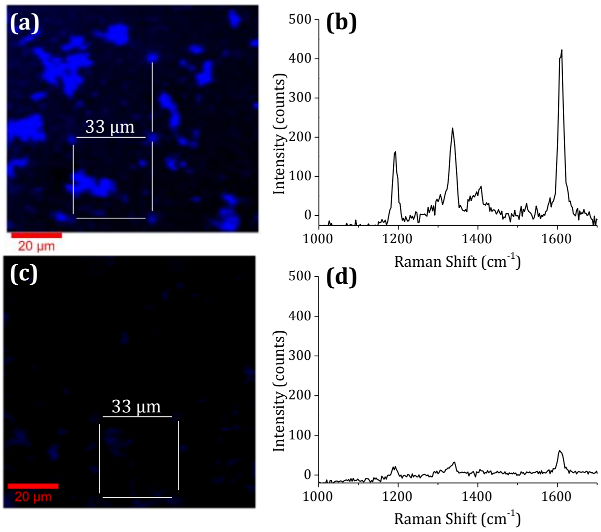

Figure 4.5. *((**a**) and (**c**)) Raman maps of an area of the array and ((**b**) and (**d**)) spectra taken from a spot within the array on epoxysilane coated glass. False colour maps were generated with respect to the band at 1609 cm^{-1}. (**a**) and (**b**) were obtained before a wash step and (**c**) and (**d**) were collected after washing with dddH$_2$O. Maps were obtained using a 633 nm laser excitation wavelength and 1 µm resolution with a 50x objective.*

The peak at 1609 cm^{-1} was again used to generate the maps, which are black in areas of low intensity through to blue in areas of most intense Raman signal. The Raman map in Figure 4.5 (a) shows a section of the array where the spots can be clearly observed. Spectra obtained from one of the spots (Figure 4.5 (b)) shows peaks corresponding to the CTC and the assay was therefore successful. However, although some spots are visible, patches of oxidised TMB can be observed across the area of the slide, making it difficult to see some of the arrays. It was therefore decided to carry out a wash step in attempt to remove some of the patches of non-specific TMB precipitate. The map and a spectrum collected following the wash step are shown in Figure 4.5 (c) and (d), respectively. It can be observed here that although patches appear to be smaller, the area still contains many patches of oxidised TMB out with the printed arrays. It can also be noted that in the Raman spectra acquired from the spots after washing (Figure 4.5 (d)), the intensity of the bands has dramatically decreased. It can therefore be concluded that although some of the non-specific patches were removed, the washing step also removed some of the desired signal thus having a detrimental effect on the assay. This may be due to the fact that the TMB precipitate which forms around the spots is not bound to the surface and it is therefore easily removed by washing.

It was thought that the patches of oxidised TMB may be a result of the precipitate migrating in the solution and landing on the surface during the TMB incubation step. Previously this incubation was overnight, so in order to reduce the possibility of the precipitate migrating from the spots, the duration of this step was reduced.

In the following experiment, the TMB was left on for 2 hours as opposed to previously being left overnight. Figure 4.6 shows the spectra and maps resulting from four of the samples analysed in this assay.

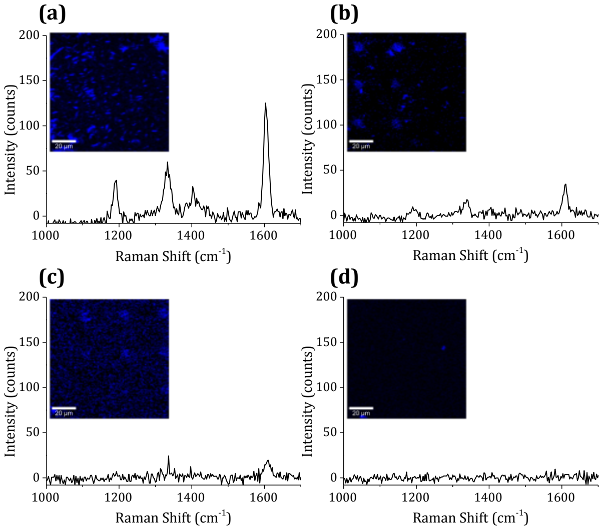

Figure 4.6. *Raman maps and spectra from arrays of* ***(a)*** *60 ng/mL PSA,* ***(b)*** *15 ng/mL PSA,* ***(c)*** *3.75 ng/mL PSA and* ***(d)*** *blank control with two hour TMB incubation. Maps were collected using a 633 nm laser excitation wavelength, a 50x objective and at 1 µm resolution. False colour images were generated with respect to the band at 1609 cm^{-1}. Scale bar = 20 µm.*

Although reduced, there is still a significant amount of oxidised TMB around the surface. It is especially noticeable in the 60 ng/mL sample (Figure 4.6 (a)) where it is difficult to distinguish between the spots and the background TMB. Despite this, a decrease in signal intensity is observed with decreasing PSA concentration and there is little to no signal for the blank control. Therefore, aside from the problems with non-specific signal, the assay showed promise.

However, another problem observed with the assay on epoxysilane glass is the difficulty locating the arrays on the surface, both under white light and in the resulting Raman maps. In an attempt to overcome these issues, alternative substrates were investigated and the results compared to the performance on the epoxysilane coated glass.

4.2.2 3D Nitrocellulose Substrates

Although reasonable results were obtained on epoxysilane glass, the patches of TMB across the surface were problematic and washing removed the desired signal from the spots. Furthermore, the arrays were difficult to visualise on the transparent surface and with non-specific areas of TMB.

Nitrocellulose surfaces are an alternative to functionalised glass slides whereby the glass slide is coated with a polymer layer, which provides a high surface area and immobilises proteins by hydrophobic and electrostatic interactions rather than covalent bonding.[160-161]

Nitrocellulose substrates have a high affinity for protein absorption and, once attached, protein activity is retained. They are easier to use than, for instance, poly-L-lysine slides and the problem of uneven surface coverage is reduced.[162] A drawback of nitrocellulose is that it gives a higher than desirable fluorescent background.[158] However, this can be overcome using alternative detection methods and was thus not considered a problem in this work.

It was suspected that the porous nature of the nitrocellulose surface may allow the TMB precipitate to be retained in the matrix to overcome the problems which arose on the glass surfaces. Therefore, the assay was carried out on nitrocellulose to determine whether or not the different substrate would improve the results.

In the same way as with the glass slides, the assay was first tested in bulk by spotting the capture antibody onto the surface using a pipette then carrying out the PSA immunoassay. Figure 4.7 shows the Raman maps (a) and (c) and representative spectra (b) and (d) obtained from the bulk samples on the 3D nitrocellulose surface. Although an intense Raman signal can be observed here, the spots are not well-defined like those on the epoxy glass slides and it appears that the proteins have spread through the porous matrix rather than remaining in the structured spot formation.

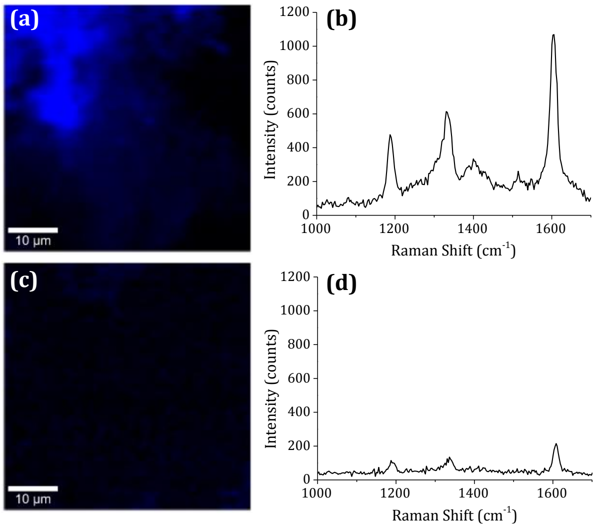

***Figure 4.7. (a)** and **(c)** Raman maps of the 60 ng/mL and 0 ng/mL bulk samples on 3D nitrocellulose, respectively. **(b)** and **(d)** are spectra from selected points in the maps. Maps were obtained using a 633 nm laser excitation wavelength, a 100x objective and 1 µm resolution. False colour images were generated with respect to the band at 1609 cm^{-1}.*

Since a strong TMB signal was observed for the 60 ng/mL sample with little signal from non-specific binding, the immunoassay arrays were investigated despite the fact that the bulk spot had appeared to spread on the surface. It was suspected that this may not be so much of a problem with the arrays where only small amounts of protein are deposited by the DPN tip and thus less spreading may occur.

During printing of the arrays onto the 3D nitrocellulose pads, it was found that the tip was running out of ink quicker so that only small arrays could be printed. This was a result of the porous substrate drawing the ink from the tip more so than a flat surface such as functionalised glass. Nonetheless, the assay was carried out with the arrays that were printed and Raman maps were obtained for each concentration of PSA. The false colour images for the 60 ng/mL and the blank control are shown in Figure 4.8 (a) and (c) along with corresponding spectra from a point in each map (b) and (d).

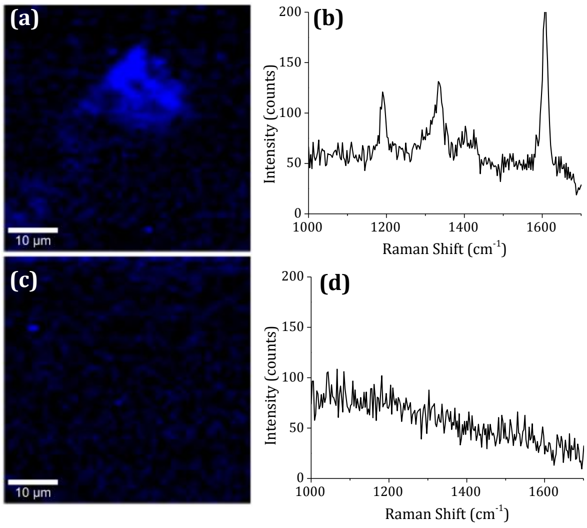

***Figure 4.8. (a)** and **(c)** Raman maps of the 60 ng/mL and 0 ng/mL PSA arrays, respectively, on 3D nitrocellulose. **(b)** and **(d)** are spectra from selected points in the maps. Maps were obtained using a 633 nm laser excitation wavelength and 1 μm resolution using a 100x objective. False colour images were generated with respect to the band at 1609 cm^{-1}.*

Although Raman signal was obtained for the sample containing PSA and not for the blank control, it can also be observed that even when such small volumes of antibody are deposited on the surface, the proteins have spread in the matrix and have not remained in well-defined spots, indicating that perhaps these substrates are too porous and hence not suitable for the development of immunoassay arrays.

Since the 3D nitrocellulose substrates overcame the issues with non-specific TMB signal and also facilitated location of the array spots, it was envisaged that a combination of these advantages with the ability of proteins to form well-defined spots on the flat glass surface, would present an ideal substrate for the purpose of this work.

4.2.3 Nitrocellulose PATH® Slides

PATH® slides are an alternative nitrocellulose substrate where the polymer has been spin-coated onto the glass surface to form an ultra-thin and non-porous nitrocellulose layer. The nitrocellulose coating has been shown to become porous upon hydration, allowing proteins to be adsorbed into the matrix whilst retaining their activity.[35] In comparison to their 3D counterpart, PATH® slides possess reduced fluorescent background and improved protein binding.

It was envisaged that the flat non-porous PATH® slides could improve the printing and spot definition over that on the 3D surfaces, whilst eliminating the problems which were experienced using the functionalised glass slides by absorbing the proteins and hence the TMB precipitate into the matrix.

Arrays of 36 x 8 spots of PSA capture antibody were printed onto the PATH® slides using a 0.1 s DT and 22 µm spacing. The PSA immunoassay was then carried out on the surface with the addition of TMB-blotting solution to produce the blue CTC in the regions where the spots were printed. Figure 4.9 shows optical images of a section of the PSA array on spin-coated nitrocellulose. The image in Figure 4.9 (a) was obtained before a wash step, and Figure 4.9 (b) was taken after washing with dddH$_2$O. It can be observed here that prior to washing the whole area is blue indicating that TMB is all over the surface. After washing however, the blue background has disappeared whilst leaving the blue spots of the array, indicating that the nitrocellulose is holding the proteins and thus the TMB precipitate in place. In order to reduce the chances of background signal, it was therefore decided to use a wash step when carrying out the assay on nitrocellulose. Figure 4.9 (c) and (d) are the equivalent white light images of the epoxy glass surface. These have been included for comparison, and to highlight the fact that the arrays can be seen clearly on nitrocellulose but are not visible on glass. Therefore, printing on nitrocellulose already poses an advantage over using glass substrates as it makes it easier to locate the arrays prior to Raman scanning.

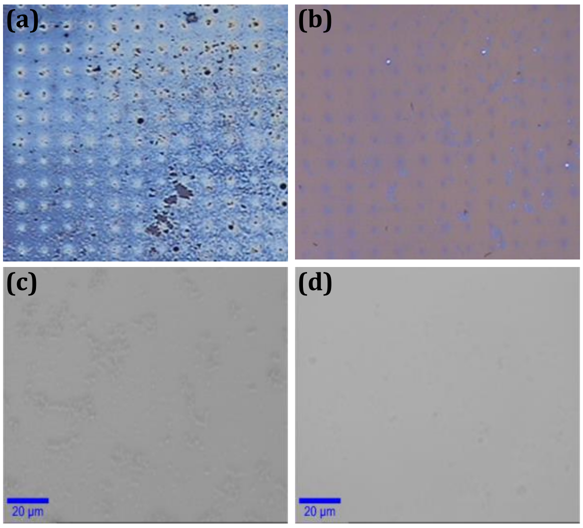

Figure 4.9 ***(a)*** *and* ***(b)*** *White light microscope images of arrays on nitrocellulose PATH® slides and on glass,* ***(c)*** *and* ***(d)****, after the PSA assay was carried out.* ***(a)*** *and* ***(c)*** *are the areas before washing and* ***(b)*** *and* ***(d)*** *were taken after washing with dddH*$_2$*O.*

After the assay was carried out on the PSA standard dilutions and the surface was rinsed with dddH$_2$O, Raman maps of the arrayed area were obtained. Spectra were collected which compared well to those obtained previously, with the three main peaks for the CTC clearly visible. The maps for the 60 ng/mL PSA standard and the blank control, generated based on the band at 1609 cm^{-1}, can be observed in Figure 4.10 (a) and (c), respectively. A spectrum obtained from a spot in each of the maps is also included in Figure 4.10 (b) and (d).

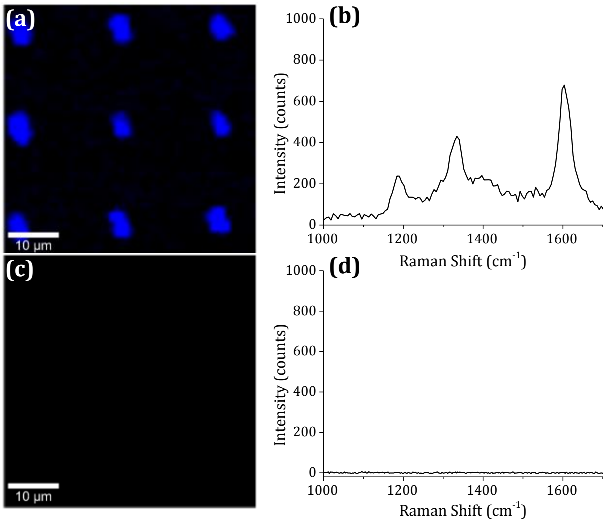

Figure 4.10. ***(a)*** *and* ***(b)*** *Raman maps of arrays on PATH® slides with 60 ng/mL and 0 ng/mL of PSA, respectively. Maps were generated with respect to the peak at 1609 cm^{-1} in the TMB spectrum.* ***(b)*** *and* ***(d)*** *are typical spectra obtained from a spot in the corresponding maps. Image scans were obtained using a 633 nm laser excitation wavelength at 1 µm resolution using a 100x objective.*

In comparison to the assays carried out on epoxysilane glass and those on 3D nitrocellulose, the spots are much clearer and well-defined with very little background interference. This is a result of the "sponge-like" nature of the spin-coated nitrocellulose allowing the precipitate to be trapped in place, rather than migrating in the solution or spreading through the pores of the substrate. This can also account for the fact that the intensity of the spots does not deteriorate with washing.

It could therefore be concluded that the nitrocellulose PATH® slides are the most suitable substrates for immunoassay arrays fabricated by DPN with RRS detection.

4.3 Quantification of PSA using Immunoassay Arrays with RRS Detection

The main aim of this investigation was to produce immunoassay arrays for the quantification of protein biomarkers using resonance Raman detection. Since a suitable surface had been selected and resonance Raman signal could be obtained from the TMB precipitate around the spots, the next stage was to determine whether a relationship between the concentration of analyte and the observed Raman signal could be obtained.

A Nexterion® incubation chamber was used to split the arrays into 16 wells and arrays of PSA capture antibody (36 x 8 spots) were printed in each well using a 0.1 s DT and 22 μm spacing. The PSA immunoassay was then carried out on a standard dilution series (0 – 60 ng/mL) where BSA was added in place of PSA for the blank control. The optimum incubation of TMB-blotting solution was found to be straight from the bottle for 30 minutes followed by a rinse with water to stop the reaction. These conditions were applied and three 50 x 50 μm Raman maps of the resulting arrays were obtained for each concentration of PSA. False colour images were generated based on the band at 1609 cm^{-1} and those obtained for the lower concentrations of PSA can be observed in Figure 4.11.

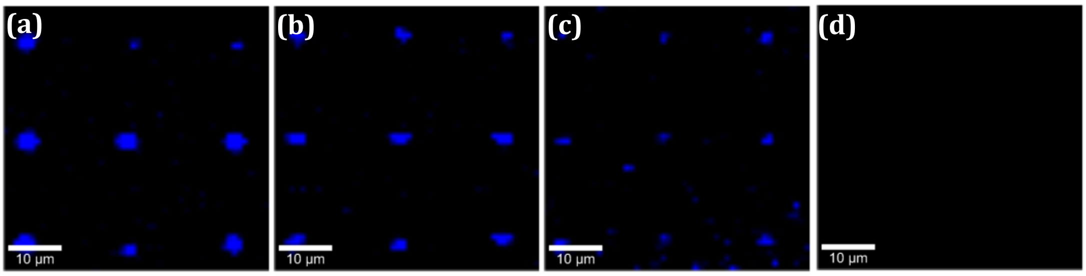

Figure 4.11. *Raman maps of the arrays containing* ***(a)*** *3.75 ng/mL,* ***(b)*** *1.88 ng/mL,* ***(c)*** *0.94 ng/mL and* ***(d)*** *0 ng/mL of the PSA standard. Maps were collected using a 633 nm laser excitation wavelength, a 100x objective and 1 μm spatial resolution. False colour images were generated with respect to the band at 1609 cm^{-1} in the spectrum of the CTC.*

In Figure 4.11 it can be observed that the signal from the spots is decreasing in intensity with decreasing concentration of PSA. Furthermore, a reduction in the size of the spots can also be observed as the concentration is reduced.

To determine whether quantification of the analyte was possible, the concentration of PSA was plotted against the sum spot intensity (Figure 4.12). The sum spot intensity was determined by selecting three spots from each of the three maps and using the WITec project software to calculate the total intensity of the spot. The values plotted were the mean total intensity with error bars representing the standard deviation.

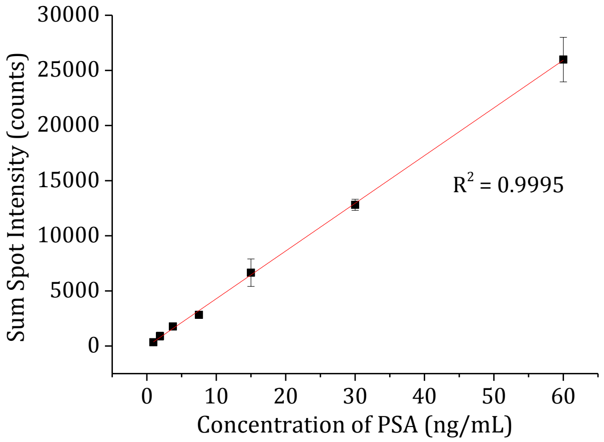

Figure 4.12. *Plot of concentration vs. intensity for the PSA immunoassay arrays on spin-coated nitrocellulose with RRS detection. The plotted intensity values are the mean total intensity of three spots from three maps with error bars representing standard deviation.*

A linear relationship, with R^2 near unity, can be observed for the entire concentration range of PSA. This was not the case with a similar assay using fluorescence detection where “topping out” of the signal could be observed above 15 ng/mL which was attributed to the saturation of the PSA binding to the capture antibody above this point, limiting the number of fluorophores available for detection.[35] The lack of a similar signal saturation in this work indicates that this is not the case and that the “topping out” is instead related to the detection method, thus highlighting the advantage of enzyme-based assays where the enzyme catalyses the conversion of many substrate molecules and hence the detection is less limited by the number of antibodies.

Since a linear relationship was obtained, the detection limit of the assay could be calculated and was found to be 25 pg/mL which is an improvement when compared to the same assay with fluorescence detection (LOD = 98 pg/mL) and also in comparison to the commercially available ELISA kit (LOD = 69 pg/mL) which uses larger sample volumes and lacks multiplexing capability. Furthermore, the detection limit obtained here is slightly lower than that calculated using resonance Raman detection in solution (Chapter 2), with the immunoassay arrays also posing further advantages over the previous method.

A plot of the concentration of PSA against the area of the resulting spot was also produced (Figure 4.13) and a general decrease in spot size with decreasing concentration of PSA was observed. This is a result of the precipitating TMB and the fact that, when there is less PSA present there will be less HRP bound in the assay and thus a reduction in the amount of TMB precipitating around the spots. This is not something that would occur with other detection methods where the label is incorporated into the assay but is a result of the enzymatic reaction and the precipitating TMB.

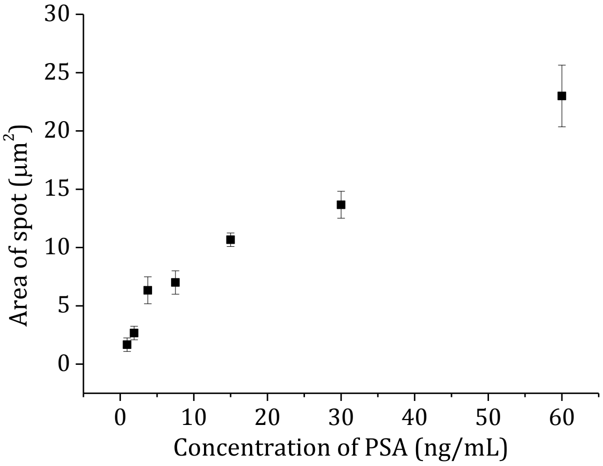

Figure 4.13. *Plot of PSA concentration versus area of the resulting array spot. Plotted values are the mean area of three spots from three maps as calculated by the WITec project software. Error bars represent standard deviation of the results.*

Although the spots decrease in intensity with decreasing concentration of PSA, the diameter of the spots range from about 2 μm to around 5 μm which is considered to be in the ideal size range (1 – 10 μm) for protein arrays.[35, 163] This is of particular significance when using optical detection techniques such as Raman spectroscopy where detection of arrays on the nanoscale may not be achievable using conventional scanners.

4.4 Concluding Remarks

The results presented indicate that the detection of the TMB precipitate using resonance Raman mapping can be successfully applied to immunoassay arrays. PATH® nitrocellulose slides were found to be the most suitable substrates for this work. They allowed the formation of well-defined spots, which could be easily observed under white light, and facilitated the immobilisation of the TMB precipitate with little background interference.

An excellent level of quantification could be observed when the immunoassay was carried out on PATH® slides, which is significant when observing the detection of a solid precipitate produced via microscale reactions. The novel method was applied for the detection of PSA and improved detection limits over alternative methods were achieved. Furthermore, resonance Raman detection of the enzyme-based assay results in a larger dynamic range than similar assays with fluorescence detection.

The feature sizes produced in this work are smaller than those obtained with alternative printing methods and have also been suggested as being in the idealised range (1 - 10 μm), since producing features of this size overcomes disadvantages of nanoscale printing whilst maintaining and improving on the validation of typical micron scale arrays (100 -200 μm).[163]

The detection of PSA has been demonstrated and it is envisaged that the methods presented could be extended to a large number of key biomarkers. Since the format of the assay has been developed from a commercially available ELISA, its application should be simple and straightforward whilst possessing many advantages over the conventional method.

Of particular interest is the potential development of an assay for the detection of multiple analytes which would be the next steps in the progression of this work. The multi-pen printing method utilised allows many different “inks” to be printed simultaneously which should enable the relatively straightforward development of such a multiplexed assay.

It would also be interesting to apply the methods to the analysis of human samples to determine whether quantification of analytes from complex mixtures could be achieved. The successful application of this assay to human samples could result in the potential for a novel method in point of care analysis. The combination of the sensitive and specific detection method with the ability of DPN to pattern multiple inks with high resolution could provide a sensitive and robust method for the detection of multiple analytes with a straightforward readout result.

5. Thermoresponsive Polymer Arrays for Potential Control of Cellular Interactions

5.1 Introduction

As previously discussed, the ability to control cellular interactions is attractive for the development of medical devices and technology. As well as patterning a surface to obtain spatial control, it is also possible to produce switchable surfaces thus offering further capabilities for the manipulation of biomolecules.[164] This chapter investigates the fabrication of a patterned polymeric surface with stimuli-responsive properties for the control of cellular interactions. DPN was utilised for its high-resolution patterning capabilities and various polymers were studied in order to determine the optimum system.

5.1.1 Thermoresponsive Polymer Hydrogels

Three-dimensional (3D) water-swollen polymers, known as hydrogels, have excellent biocompatibility due to their ability to trap water and biological fluids.[165] Their porous microstructure allows permeability, whilst the 3D structure offers mechanical support thus making them suitable in a variety of applications such as tissue engineering, separation systems, biosensors, cell scaffolds, microfluidic systems, implantable devices and synthetic extracellular matrix (ECM).[166-171]

Some hydrogels exhibit stimuli-responsiveness where they will undergo changes in swelling in response to external stimuli such as pH,[172] temperature,[173] light,[174] ionic strength[175] and electric field.[176] These induced changes in polymer structure were initially predicted in 1968[177] and later observed experimentally by Tanaka and co-workers who studied the area extensively.[178-182] Although not a novel discovery, the ability to control properties of polymers using external stimuli continues to be an area of considerable interest due to the potential application of such materials in a vast range of areas.[183]

Since it is relatively simple to control and applicable in biological systems, temperature is perhaps the most heavily studied of the possible stimuli. Across a certain temperature, thermoresponsive polymers in aqueous solution undergo a phase transition and a change in solubility. Polymers which become soluble upon heating have an upper critical solution temperature (UCST) whereas those which become insoluble with heating possess a lower critical solution temperature (LCST).[184] Figure 5.1 (a) and (b) show the phase diagrams for a polymer solution with LCST and UCST, respectively. At the phase transition shown in Figure 5.1 (a), polymer chains which are soluble in water below the LCST will precipitate as the temperature is increased above the LCST.

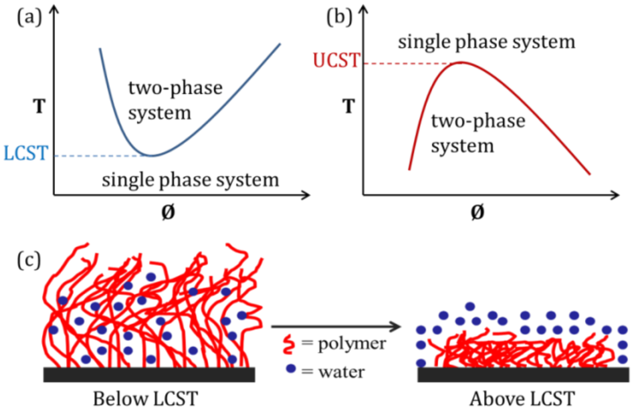

Figure 5.1. *Temperature vs. Polymer Volume Fraction, Ø, for polymer solution with* ***(a)*** *LCST and* ***(b)*** *UCST.* ***(c)*** *Schematic illustration of the swelling behaviour of a thermoresponsive polymer across the LCST.*

For hydrogels, the covalent bonds of the network structure prevent dissolving; however, changes in the swelling of the hydrogel will occur above and below the transition temperature. Most of the commonly studied systems exhibit a LCST which means that below this temperature, water-polymer interactions are thermodynamically favoured and the hydrogel is in its swollen state. However, an increase in temperature above the LCST results in these associations becoming unfavourable and thus facilitating the polymer-polymer and water-

water interactions.[183] This results in the aggregation of the hydrophobic backbone and the polar groups on the polymer, causing a change from a coiled state to a globular or collapsed state, with the water moving into the bulk solution. Below the LCST the polymer is therefore hydrophilic and swollen; whereas when the temperature rises above the LCST, it will become hydrophobic and will thus collapse or de-swell (Figure 5.1 (c)). This transition is a result of the breakdown of polymer-water hydrogen bonding interactions, and can also be attributed to the "hydrophobic effect" which induces a local structure where the water molecules form a shell surrounding the hydrophobic groups of the polymer.[185-186]

The LCST of thermoresponsive polymers is determined by the balance of polymer-polymer interactions and polymer-water interactions. It is therefore possible to tune the LCST by using copolymerisation to introduce more hydrophilic or hydrophobic substituents which will increase or decrease the LCST, respectively. This allows the LCST to be altered to make it more suitable for particular applications. Furthermore, temperature responsiveness can be combined with sensitivity to other stimuli, such as pH, in order to form hydrogels which respond to more than one stimulus.[187] pH responsiveness comes from weakly acidic or basic ionic groups on the polymeric chains, which means that if the polymer backbone contains both thermosensitive units and ionic groups, the hydrogel will possess both temperature and pH sensitivity.[172]

5.1.2 Applications of Thermoresponsive Polymers

The readily controlled change in hydration state and conformation of thermoresponsive polymers makes them extremely useful in a variety of applications such as cell culture,[188-192] thermally controlled drug delivery,[193-195] protein separation,[196] microactuators[197] and microfluidic devices.[198]

For cell culture and tissue engineering applications, thermoresponsive polymers overcome the disadvantages of conventional methods for cell adhesion and detachment. Typically, cells are cultured on tissue culture polystyrene (TCPS) and removed via trypsin digest. However, this damages cell proteins, which is a major drawback; particularly if the cells are being cultured for *in vivo* applications.[98, 199-200] The use of thermoresponsive substrates allows cells to adhere and proliferate at culture temperature and then detach upon cooling below the LCST. Okano's research group, who pioneered in this area, used surfaces grafted with thermoresponsive polymer and successfully cultured bovine hepatocytes which are sensitive to enzyme detachment methods.[199] They reported that the cultures obtained using their polymer grafted dish were superior to those recovered via the commonly utilised trypsin digest method. Following this, thermoresponsive polymer surfaces were extensively applied for cell culture applications.[183]

In a further development, Yamato *et al.* showed that by patterning cell culture surfaces with thermoresponsive polymer, they could form a co-culture of different cell types which they suggested could be useful for tissue engineering applications and for investigating cell-cell interactions (Figure 5.2).[201-202]

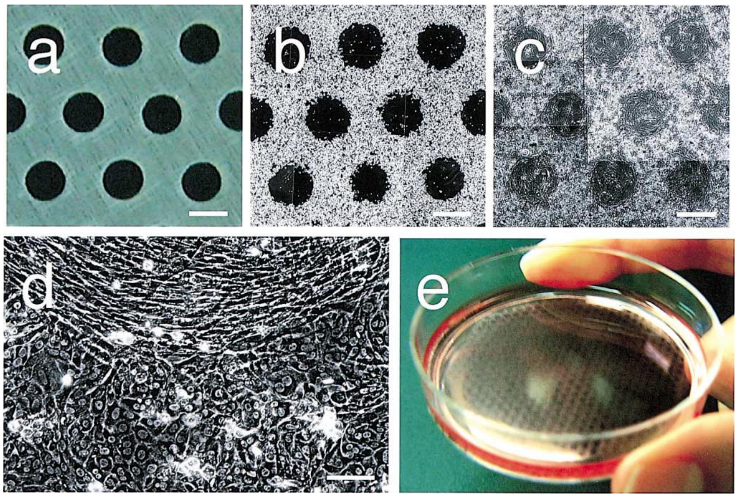

Figure 5.2. *Co-culture of hepatocytes and fibroblasts on a patterned thermoresponsive polymer substrate.* ***(a)*** *The metal mask used for the formation of the polymer patterns of 1 mm diameter circles.* ***(b)*** *Hepatocytes were seeded and cultured on the patterned dishes at 20°C, below the LCST of the polymer, and adhered only on the non-grafted areas.* ***(c)*** *Fibroblasts were seeded at 37°C, above the LCST of the polymer, and co-cultured in a defined pattern.* ***(d)*** *is a magnified image of the border of the two areas after culture and* ***(e)*** *is a macroscopic view of the patterned hepatocytes before the fibroblasts were seeded. Bar = 1 mm in a-c and 100 μm in d.*[202] *Reprinted with permission from Elsevier, Copyright © 2002.*

Since the work of Yamato and co-workers, thermoresponsive polymer surfaces have been utilised for cell sheet engineering and to produce tissue-like structures for application to a variety of tissue types.[98, 203-206]

5.1.3 Thermoresponsive Polymer Patterns

Many of the applications of thermoresponsive polymers require that the polymer is immobilised on a surface in order to create a switchable substrate. Often this is in the form of a layer or coating; however, further control can be achieved by the formation of polymer patterns.

Previous patterns of thermoresponsive polymers on a surface have used UV[207] or electron beam[202] irradiation through a patterned metal mask to ablate the polymer layer in exposed areas. However, masks offer limited control over size and position of patterns. Other techniques such as microcontact printing,[208] electron-beam lithography[209] chemical lithography[210] and nanoshaving[211] have also been investigated. These approaches involve patterning of an initiator followed by atom transfer radical polymerisation (ATRP) for the production of the polymers, rather than direct patterning onto the surface. The ability to pattern the polymer directly, however, can provide precise control over the feature size, shape and location on the surface.[212]

Lee *et al.* used thermal dip-pen nanolithography (tDPN) to produce nanopatterns of a temperature-sensitive polymer which they utilised for the binding and release of proteins.[212] They printed polymer lines and characterised the thermoresponse using adhesion force, F_{adh}, measurements. They observed the expected hydrophilic-hydrophobic transition but without a change in topography, attributing this to the orientation of the polymer on the surface. Although their surface was successfully applied for protein adsorption, the lack of height change may limit the application in other areas.

In this work, the aim was to use DPN to produce polymer patterns with sufficient control over feature size and position and to subsequently study the changes in topography of the patterns, which should swell or shrink in response to temperature change. Ultimately, the goal was to use the optimised system to control cellular behaviour by changing temperature and thus the polymer topography.

In order to achieve these objectives, a suitable ink system and surface chemistry first had to be developed to obtain successful printing of the polymer arrays.

5.2 Fabrication of Thermoresponsive Polymer Arrays

The strategy adopted here was to print a monomer ink solution, or pre-polymer, using liquid ink transport with subsequent polymerisation on the surface. Various thermoresponsive inks were investigated and the ink transport and printing capabilities were compared for each system.

The NLP 2000® was utilised for printing all of the arrays due to its capabilities in fast patterning and its suitability for printing with liquid inks using the inkwell arrays.

5.2.1 Poly(N-isopropylacrylamide)

Poly(N-isopropylacrylamide) (PNIPAAm) is the most widely studied thermoresponsive polymer due to its known biocompatibility, the sharp phase transition, and its LCST of around 32°C which makes it suitable for biological applications. This was hence selected as a good starting point for investigations.

N-isopropylacrylamide (NIPAAm), Figure 5.3, is a solid monomer; therefore, it had to be dissolved in a suitable solvent prior to printing. This required extensive optimisation of monomer concentrations, suitable solvents and solvent ratios.

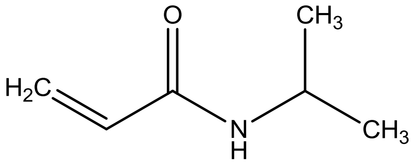

Figure 5.3. *N-Isopropylacrylamide.*

Initially, the monomer was dissolved at 50% w/v in a 1:1 ratio of H_2O and IPA with a small amount of poly(ethylene glycol) dimethacrylate (PEG-DMA) as the crosslinker (4% w.r.t NIPAAm) and hydroxycyclohexyl phenyl ketone as the photoinitiator (0.4% w.r.t NIPAAm) for crosslinking by UV irradiation. The bulk properties were then investigated prior to attempting to print. This way it was possible to determine the bulk swelling properties and determine whether or not the crosslinking process was successful in these conditions. Figure 5.4 shows the Raman characterisation of the ink before and after polymerisation. The spectra have been split into two regions, below 2000 cm^{-1} and 2500 cm^{-1} – 3200 cm^{-1}, which can be observed in Figure 5.4 (a) and (b), respectively. The spectrum of the monomer ink solution was obtained (black), before any exposure to UV, and two different samples were irradiated for 5 minutes and 10 minutes in a sealed chamber under inert atmosphere before Raman spectra were obtained. The spectra for the sample irradiated for 5 minutes (red) and 10 minutes (blue) can also be observed in Figure 5.4. In the monomer sample, the stretching mode for C=C can be observed at around 1620 cm^{-1}. This also overlaps slightly with the C=O amide stretching band (around 1654 cm^{-1}); however, in the polymer samples, after UV crosslinking, the C=C stretch has disappeared and only the C=O amide stretch is still visible indicating that the polymerization has been successful. This is also supported by the disappearance of the vibrations in the 3000 cm^{-1} – 3100 cm^{-1} as these bands can be attributed to the CH stretching modes of CH=CH and $CH=CH_2$. From the spectra it could also be concluded that 5 minutes was enough time for the samples to be exposed to the UV lamp in order to achieve successful polymerisation.

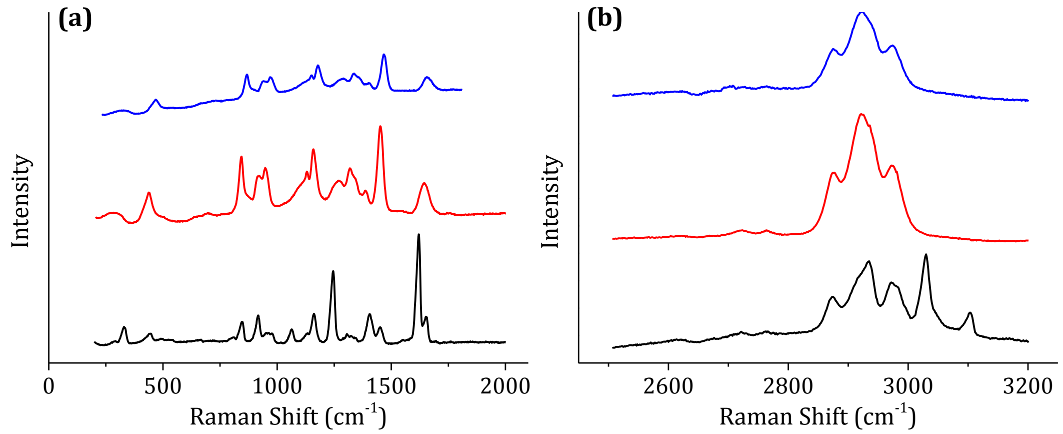

Figure 5.4. *Raman spectra in the region below 2000 cm^{-1}* ***(a)*** *and between 2500 cm^{-1} and 3200 cm^{-1}* ***(b)*** *for the monomer solution (black), after 5 minutes of UV irradiation (red) and after 10 minutes of UV irradiation (blue). Spectra were obtained using a 633 nm laser excitation wavelength and with 5 x 10 second accumulations.*

Further to characterising the changes by Raman scattering, confirmation of the swelling properties of the polymer was attained. A disk, approximately 3.5 cm^{-1} in diameter, was polymerised by UV crosslinking for 5 minutes before being placed in dddH$_2$O for 72 hours to reach equilibrium swelling. The sample was then heated and a phase transition was observed at 32°C – 34°C. The phase transition could be observed by eye as the transparent hydrogels shrunk considerably and turned opaque. The swelling ratio was also calculated using Equation 5.1 and was found to be ~3 which is in the range of those quoted in the literature for PNIPAAm.

$$q_W = \frac{W_{20°C}}{W_{40°C}}$$

Equation 5.1

Where:

q_W = equilibrium weight swelling ratio
$W_{20°C}$ = weight of the swollen hydrogel at room temperature
$W_{40°C}$ = weight of the hydrogel after heating to 40°C

Since the polymerisation was successful and the thermoresponsive behaviour could be observed for the bulk material, it could be supposed that the conditions were suitable and that successful patterning of this system may yield stimuli-sensitive arrays. For this reason, the same monomer solution was prepared to be used as an ink for patterning by DPN.

For any array printing, careful consideration of the ink properties and surface chemistry must be taken. Nanoink silicon dioxide surfaces were selected which are supplied with registration marks, making it easy to locate specific areas on the surface. To facilitate binding of the polymer to the silicon dioxide surface, silanisation of the surface was required. Two different silanes, one with methacrylate and one with thiol end functional group, were investigated for this purpose. Although there was a slight improvement on the thiol silanised surface, the ink did not form spots and instead spread out on the surface before evaporating completely. It was suspected that increasing the monomer concentration may improve the printing; however, a full range of concentrations was attempted to no avail, so the solvent system had to be changed. Various solvent combinations and conditions were attempted until an optimum system was discovered. A summary of some of the conditions with the resulting printing performance can be found in Table 5.1.

Table 5.1. *Various ink systems which were attempted to facilitate the printing of NIPAAm.*

Solvent	Printing Performance
H_2O/IPA	• Spots spread then evaporated at various monomer concentrations • 60 % monomer gave best results
Glycerol/IPA	• 60% monomer insoluble • 35% monomer arrays printed but rinsed off with H_2O after crosslinking • 35% monomer in 1:1 and 1:3 also began to solidify in wells
H_2O/Brij 35	• Arrays printed with 20% and 30% monomer in H_2O with 50 % Brij (w.r.t monomer weight) but spread and dried out with 30% monomer
H_2O/Brij 35/Glycerol	• Printed arrays but spot quality inferior to H_2O/Brij 35

Changing the solvent to glycerol/IPA rather than H_2O/IPA improved the printing performance somewhat; hence the arrays were exposed to 5 minutes UV irradiation to crosslink the polymer. Subsequent rinsing of the surface, however, removed the arrays, indicating that either the bonding of the polymer to the surface hadn't occurred or that the polymerisation was unsuccessful. Forney *et al*. found that by adding a non-ionic surfactant, polyoxyethylene (2) cetyl ether (Brij 52), they could achieve rapid deswelling of PNIPAAm which they thought may arise from further control of the polymer nanostructure, supported by the surfactant.[213] A similar surfactant, polyoxyethylene (23) lauryl ether (Brij 35) was employed in this work and the formulation used by Forney *et al*.[213] was followed in order to improve the printing performance. Bulk swelling behaviour was also confirmed prior to printing and the phase transition could be observed at around 32°C. Arrays were successfully printed using this method and the ink behaviour improved drastically over previous systems. Characterisation by Raman scattering was undertaken to confirm the composition of the array spots. The spectrum of the spot did not match that of the monomer taken previously; hence the spectrum of Brij 35 in H_2O was also obtained for comparison (Figure 5.5). This confirmed that in fact the array spots were composed of the surfactant rather than the monomer. The spots also rinsed off with H_2O after crosslinking and so this system was deemed unsuitable for printing.

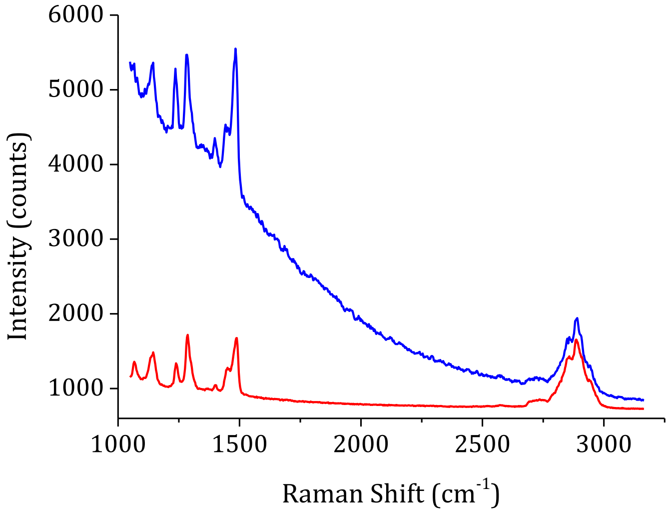

Figure 5.5. *NIPAAm in H_2O/Brij array spot (blue) Brij in H_2O (red). Characterisation of the array spot by Raman scattering showed that the array spot was composed of Brij 35. Spectra were collected using a 633 nm laser excitation and 5 x 10 second accumulations.*

Although further optimisation of the system could be attempted, there were many parameters to be considered and it was hypothesised that perhaps another monomer may be more suitable for use with DPN. Another of the N-alkyl acrylamides, N,N-Diethylacrylamide (DEAAm), was investigated in the next phase of this work.

5.2.2. N,N-Diethylacrylamide

The main advantage of DEAAm over NIPAAm for the work presented here is that DEAAm is a liquid monomer and therefore no solvent was required for the printing of the arrays using liquid ink transport. Instead, the crosslinker and initiator could be dissolved in the monomer, leaving less parameters to be considered for optimisation, and the ink solution could once again be cured by UV-irradiation (Scheme 5.1).

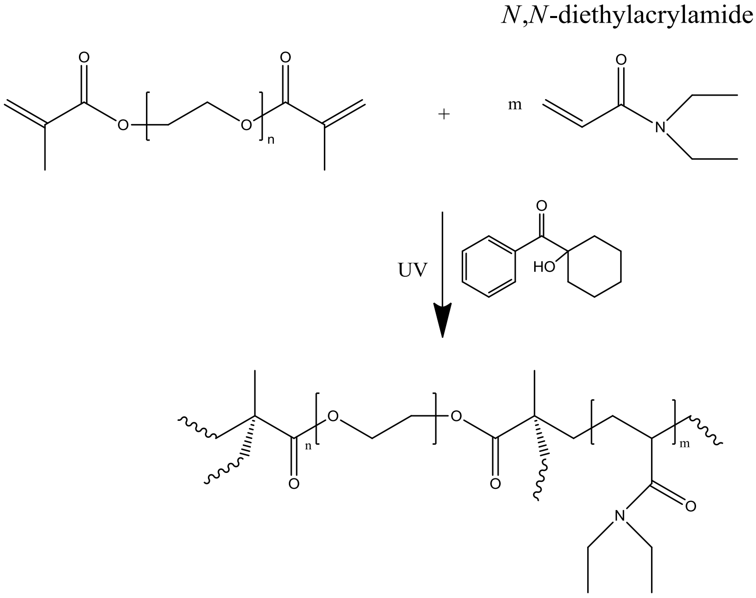

Scheme 5.1.*The polymerisation of DEAAm with PEG-DMA using a photoinitiator*

The best bulk swelling properties ($q_W = 4$) were achieved using 0.5 % crosslinker and 3 % initiator (w.r.t monomer); therefore, the same concentrations were used to make up the pre-polymer ink solution. Again, two different silanes were investigated for covalent bonding of the thermoresponsive polymer arrays to the silicon dioxide substrate. The results of the printing on each surface can be observed in Figure 5.6. The array printing improved significantly over that of the NIPAAm and consistent and well-defined array spots were formed, particularly on the methacrylate silanised surface (Figure 5.6 (b) and (d)). Different printing conditions were investigated for the novel ink system and the best results were obtained using shorter dwell times. This is a result of the ink remaining on the tip for the whole printing process, thus allowing more consistent array spots to be obtained.

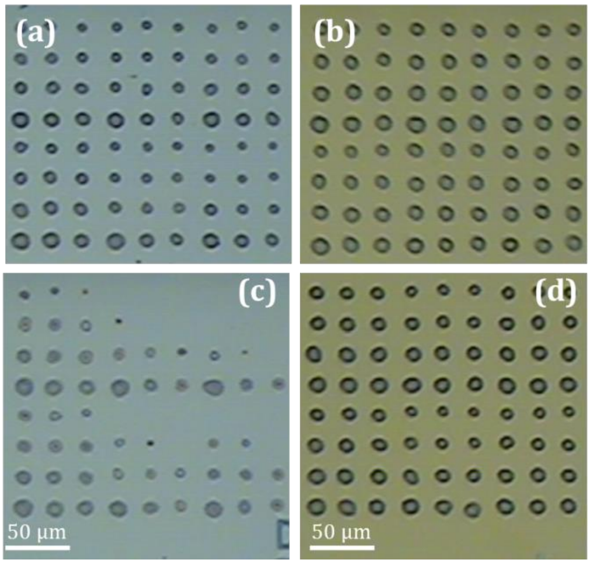

Figure 5.6. *Arrays of DEAAm on silicon dioxide substrates silanised by thiol **(a)** and **(c)** and methacrylate **(b)** and **(d)** terminated silanes. The arrays were printed using 0.25 s DT **(a)** and **(b)** and 0.5 s DT in **(c)** and **(d)**.*

Raman scattering was used to determine the composition of the printed features and the spectrum of the spot was compared to a spot of the ink solution, made by pipetting a small amount of the ink onto the silicon dioxide surface. The resulting spectra are shown in Figure 5.7 where it can be observed that the spectra of the ink solution (red) and the printed array spot (blue) are different, indicating that the composition of the array spots was not the same as that of the bulk ink solution. The presence of the band at around 1720 cm^{-1} for the printed array spot is characteristic of the carbonyl stretching of ester groups. This led to the suspicion that the spot may be composed of the PEG-DMA crosslinker, which was further supported by the presence of the C-O-C stretching mode at 1285 cm^{-1}.

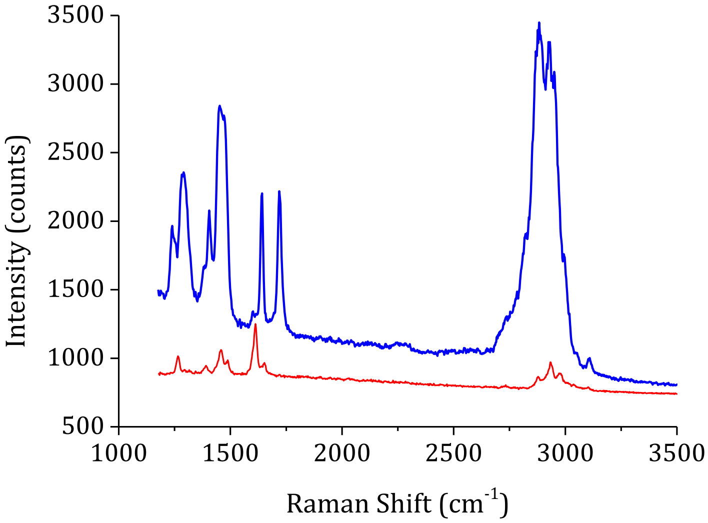

Figure 5.7. *Raman spectra of the printed array spot (blue) and ink microspot made by pipette (red). Spectra were collected using a 633 nm laser excitation wavelength and 5 x 10 second accumulations.*

In order to confirm the composition of the features printed by DPN, a Raman spectrum of each of the individual ink components was acquired. The resulting spectra are compared in Figure 5.8 (a) where it does in fact appear that the printed array spot is giving the same spectrum as the crosslinker. Figure 5.8 (b) is a direct comparison of the array spot spectrum with that of the crosslinker, confirming that the array spot consists of PEG-DMA and that the monomer is not present in the printed spot.

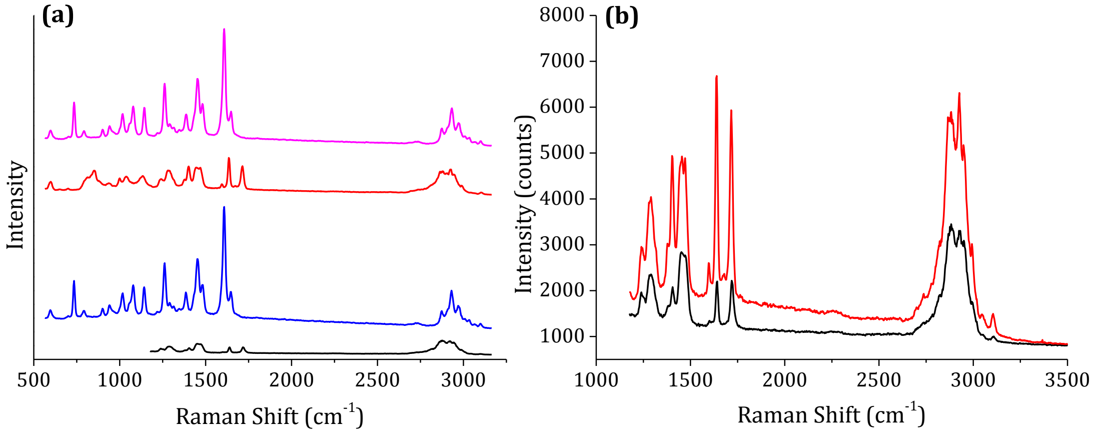

Figure 5.8. *Raman spectra of each component of the ink solution* ***(a)*** *stacked for illustration. The spectrum of the printed array spot (black), the monomer (blue), the crosslinker (red) and entire ink solution (magenta). Since it appears that the spectrum of the printed array matches that of the crosslinker, the two are compared directly in* ***(b)****. All spectra were obtained at 633 nm laser excitation using 5 x 10 second accumulations.*

The lack of monomer in the array spot is a result of the volatility of DEAAm in air. The DEAAm becomes increasingly volatile at the microscale, resulting in evaporation of the monomer during the printing process. Various steps were taken to prevent or decelerate the evaporation; however, all attempts were unsuccessful for a variety of reasons and a new ink system was therefore investigated.

5.2.3 Jeffamine ED-600

Jeffamines are a range of commercially available amino-terminated copolymers of ethylene oxide and propylene oxide, which have recently been shown to exhibit thermoresponsive properties.[214-215] A novel ink system, using Jeffamine ED-600 as the thermoresponsive component, was investigated (Scheme 5.2).

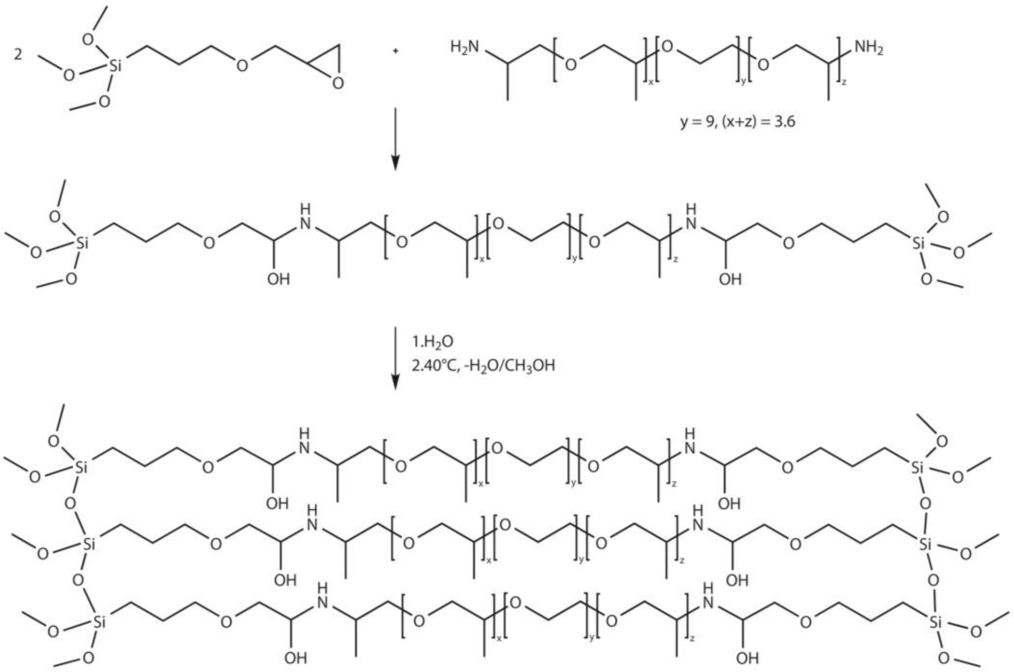

Scheme 5.2. *Polymerisation of Jeffamine ED-600 with GPTMS.*

The Jeffamine ink was prepared by mixing the Jeffamine ED-600 with GPTMS and stirring for 2 hours before adding water and stirring for a further

10 minutes. Each inkwell was then loaded with 0.3 μL of Jeffamine ink and the arrays were printed as previously described. Post-printing, the arrays were left overnight in a closed box prior to being cured at 40°C for 1 hour.

The swelling of the system was investigated for the bulk sample and the phase transition was observed, with a swelling ratio of ~ 1.4.

Since the ink contained silane end-groups, it was initially suspected that silanisation of the surface would not be required or that an epoxy silane coated surface may be suitable. Therefore, various substrates were investigated to find the most appropriate for the printing of Jeffamine arrays. Printing on epoxy silane coated glass slides was successful, however it was considered rather impractical as the arrays were difficult to visualise (Figure 5.9 (a)). Arrays on the bare silicon dioxide surface spread and did not form well-defined features (Figure 5.9 (b)) and similar results were observed on the methacrylate-silanised surface (Figure 5.9 (c)). The best array printing was observed on the thiol-silanised substrate (Figure 5.9 (d)), contrary to what was found with the DEAAm ink. This is due to the Jeffamine ink being more hydrophilic than the UV-curable DEAAm and thus the substrate is required to be more hydrophobic to allow formation of spots.

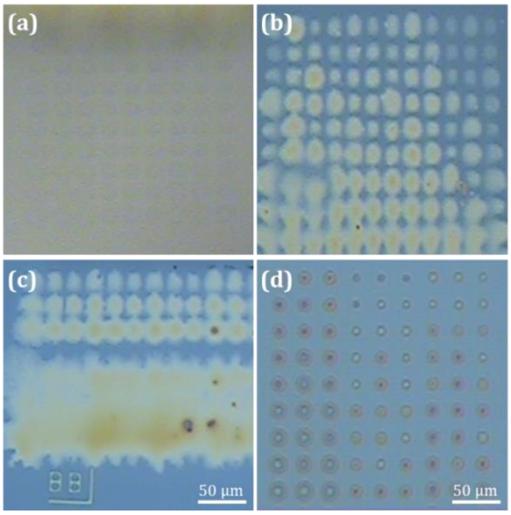

Figure 5.9. *Jeffamine array spots printed on epoxy silane coated glass* ***(a)****, bare silicon dioxide* ***(b)*** *methacrylate-silanised silicon dioxide* ***(c)*** *and thiol-silanised silicon dioxide* ***(d)****.*

Characterisation of the polymer arrays by Raman scattering gave the same spectrum for the array spot as that obtained from the bulk material, indicating that the array spots were indeed composed of the desired Jeffamine ink (Figure 5.10).

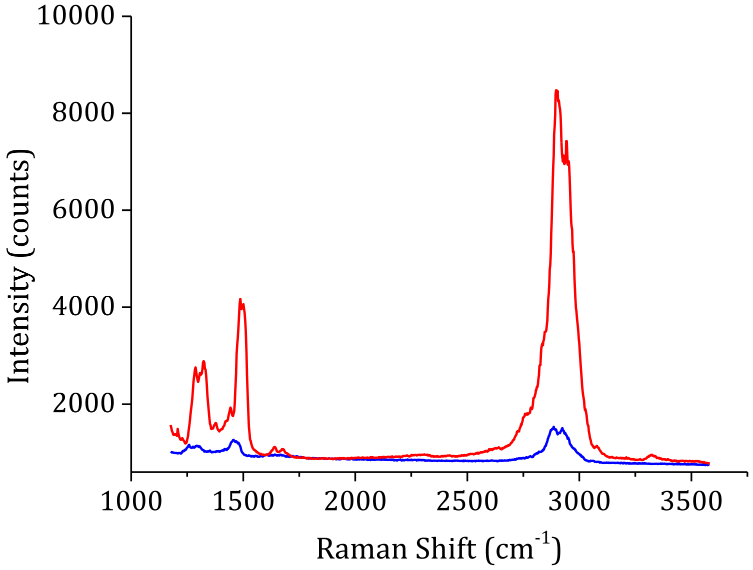

Figure 5.10. *Raman spectra of the Jeffamine bulk material (red) and the printed array spot (blue) acquired using a 633 nm laser excitation wavelength and 5 x 10 second accumulations.*

Although the bulk swelling properties of the Jeffamine ED-600 were slightly inferior to those of the previously investigated UV-curable inks, the ink transport and printing capabilities thus far showed significant improvement.

Further characterisation of the polymer arrays was attained using AFM. Figure 5.11 shows a white light image of the printed features (a) with a corresponding AFM topography image of a section of the arrays (b). Figure 5.11 (c) is the height profile across two of the spots which shows the successful formation of polymer spots.

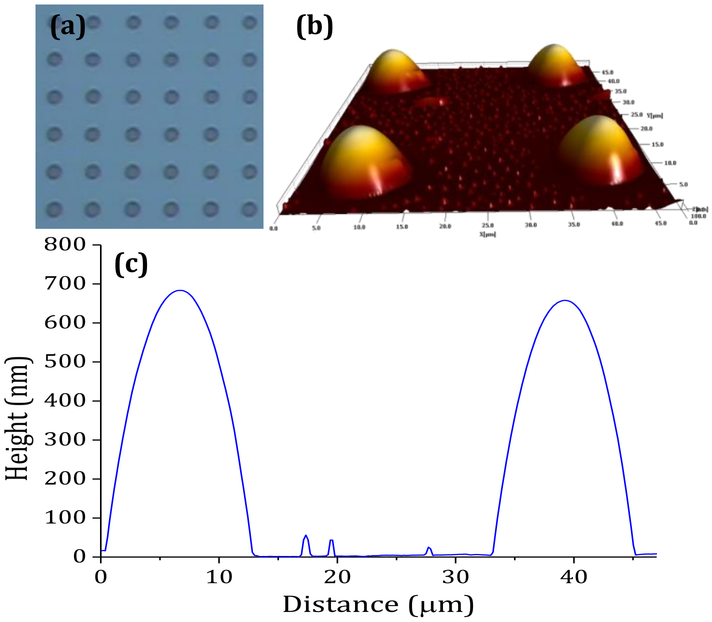

Figure 5.11. (a) *White light image of the Jeffamine ED-600 arrays printed using the NLP 2000® with a 0.5 s dwell time and 33 μm spacing.* ***(b)*** *Corresponding AFM topography image.* ***(c)*** *The height profile across two of the array spots observed in* ***(b)****.*

The improved ink transport and consequent successful array printing can be attributed to the slightly higher viscosity of the Jeffamine ED-600 ink compared with the systems studied previously. This also allowed large sets of arrays to be printed without the need to re-ink the tip whilst retaining the consistency of spot size and shape.

To determine whether the size of the spots could be controlled, a study was undertaken where the dwell time was varied and AFM images of the resulting arrays were obtained. Figure 5.12 is the plot of dwell time against spot diameter (a) and spot height (b). It can be observed here that there is a general increase in both the height and diameter of the printed features with increasing dwell time. The array spots ranged from 11 μm in diameter to around 15 μm when varying the dwell time from 0.1 s to 1 s and the height of the spots ranged from 605 nm up to 720 nm with the same change in tip-substrate contact time. This trend in spot size indicates that, with a simple alteration in printing conditions, arrays of Jeffamine ED-600 can be printed with significant control over the size of spots. Therefore, patterning of these polymer arrays with both spatial control and control of the feature size is achievable using DPN.

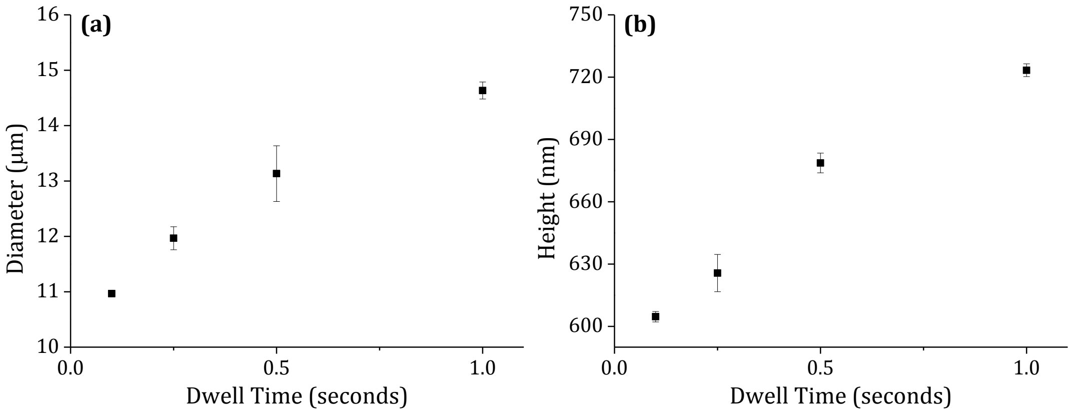

Figure 5.12. *Plot of dwell time against spot diameter* ***(a)*** *and height* ***(b)*** *of the Jeffamine ED-600 arrays printed by DPN.*

With the successful array printing, the Jeffamine ED-600 ink system showed good potential for the production of thermoresponsive polymer arrays; however, the one concern was the inferior swelling properties over those of, for example, the DEAAm. In order to improve the swelling properties, it was suspected that perhaps the two systems could be combined; hence a combination of the two ink systems was investigated.

5.2.4 Mixed System: Jeffamine ED-600 and N,N-Diethylacrylamide

In the novel combination of the Jeffamine ED-600 with the DEAAm, it was envisaged that the Jeffamine could not only act as a thermoresponsive component but also as a host matrix for the DEAAm. The hydroxyl and secondary amine groups in the Jeffamine matrix can interact with the amide group of the DEAAm to reduce the evaporation of the DEAAm and to improve the ink transport. Both ink systems were prepared individually, in the same way as previously, before being combined with the addition of a methacrylate-terminated silane, which was introduced to covalently link the Jeffamine matrix to the acrylamide network (Scheme 5.3).

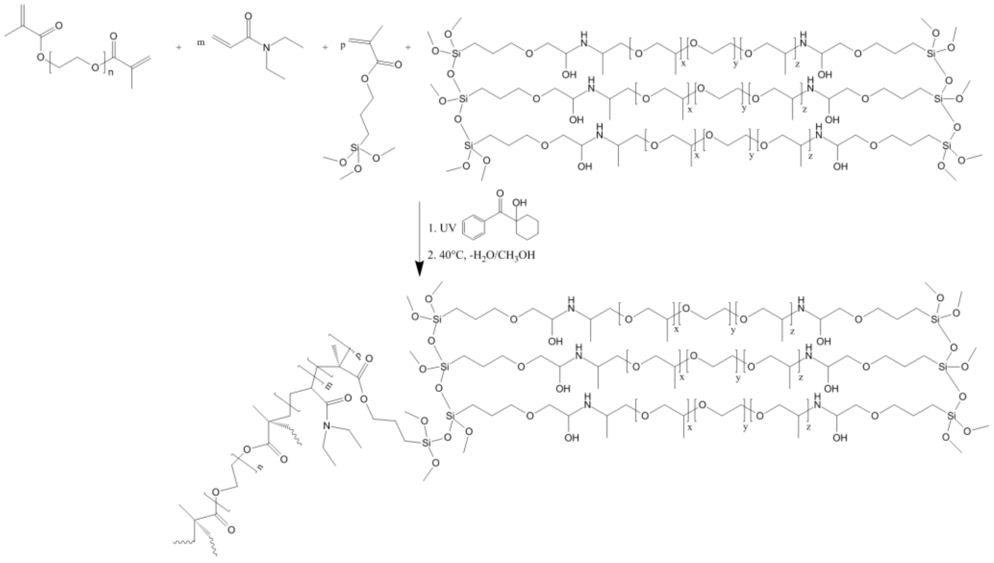

Scheme 5.3. *The Jeffamine/DEAAm mixed system where the Jeffamine gel acts as a host matrix for the DEAAm.*

The bulk swelling properties of the mixed system (Jeff/DEAAm) were investigated and a swelling ratio of 2.3 was obtained. This is an intermediate value between those exhibited by the two systems individually which indicated that the combination of the two is successful and that the introduction of the DEAAm into the Jeffamine matrix enhances the thermosensitivity. The phase transition of the bulk system could be observed by eye and is illustrated in Figure 5.13. It can be observed here that the polymer disk has shrunk after heating and takes up less space in the dish. A break in the polymer has also occurred, probably due to the increased brittleness when the water is expelled. Furthermore, the phase change was reversible which was not the case with the Jeffamine system and so arises from the presence of the DEAAm which does show a reversible phase change when present in its own individual system.

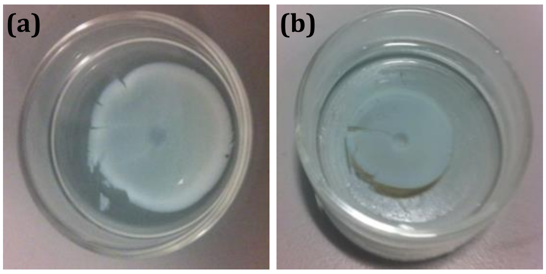

Figure 5.13. *The Jeff/DEAAm polymer disk in water at room temperature* ***(a)*** *and when heated past the LCST* ***(b)****. The change in dimensions can be observed upon shrinking.*

Since the bulk properties of the mixed system showed improvements over those of the Jeffamine alone, the printing capabilities were investigated to determine whether similar arrays could be fabricated. Arrays were printed on thiol-silanised silicon dioxide substrates using the same conditions as the Jeffamine system alone and, once again, it was possible to print large sets of arrays with well-defined spots. Figure 5.14 shows a white light image (a) and AFM topography image of a small section of the arrays (b) indicating that printing with Jeff/DEAAm resulted in features similar to those previously fabricated with Jeffamine ED-600.

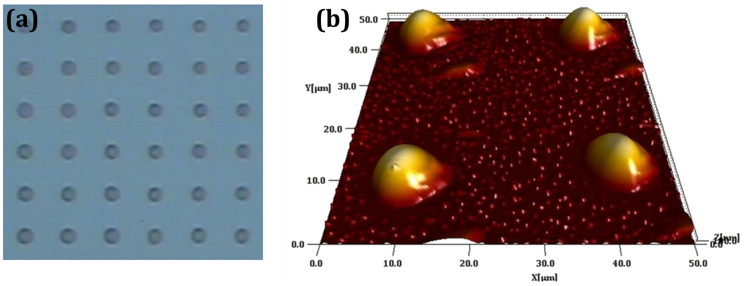

Figure 5.14. *White light* ***(a)*** *and AFM topography* ***(b)*** *images of the Jeff/DEAAm arrays printed using the NLP 2000®with 0.5 s dwell time and 33 μm pitch.*

In a similar manner to the Jeffamine alone, the Jeff/DEAAm arrays were printed with a range of dwell times and the resulting spot sizes were compared (Figure 5.15). Once again, a general increase in both spot diameter (a) and height (b) could be observed indicating that control over the feature size was possible. In comparison to the arrays of Jeffamine ED-600, the Jeff/DEAA features were generally smaller, ranging from just over 9 μm to around 13 μm in diameter and from less than 550 nm to just over 650 nm in height. This slight decrease in feature size could be resulting from a change in viscosity between the two ink systems. A slight increase in viscosity will give rise to slower ink transport from tip to substrate and hence smaller spots will be obtained using the same contact times.

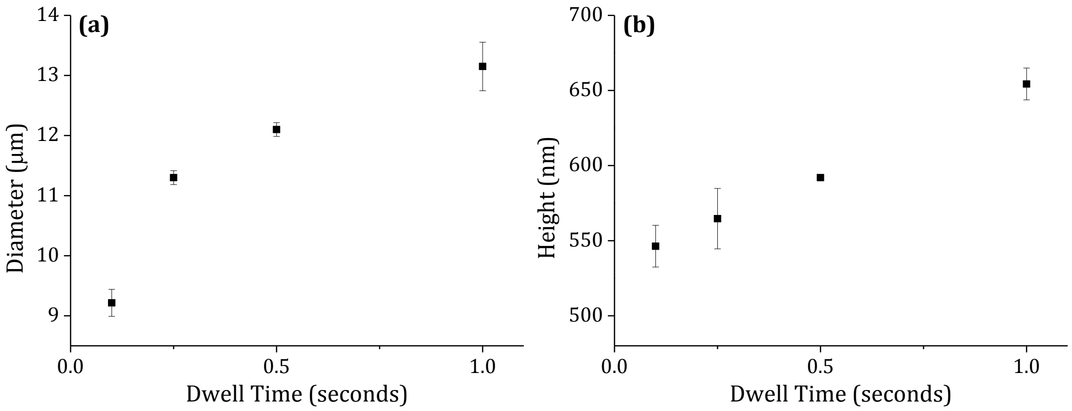

Figure 5.15. *Plot of dwell time versus spot diameter* ***(a)*** *and height* ***(b)*** *for the Jeff/DEAAm arrays fabricated by DPN.*

Chemical characterisation of the printed arrays was necessary to confirm the composition of the spots and to obtain structural information of the novel ink system. Raman scattering was used for this characterisation and a comparison was made between the spectra of the array spots and the bulk material. The resulting spectra are displayed in an offset stack in Figure 5.16 where it can be observed that the spectrum of the Jeff/DEAAm array spot (black) does not match that of the Jeff/DEAA bulk material (red) but appears to have the same peaks as the Jeffamine bulk material (blue).

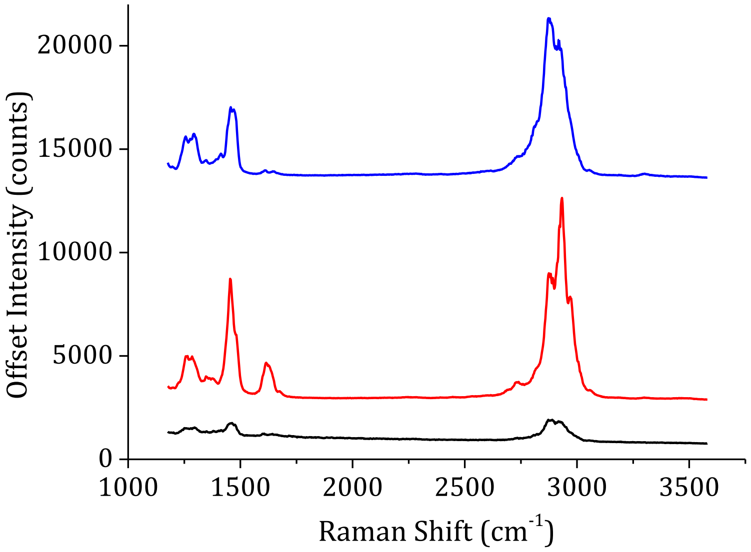

Figure 5.16. *Raman spectra of the Jeff/DEAAm array spot (black), Jeff/DEAAm bulk material (red) and Jeffamine ED-600 bulk material (blue). Spectra were collected using a 633 nm laser excitation and 5 x 10 second accumulations. The spectra have been stacked for illustration using offset Y values.*

The spectrum of the Jeff/DEAAm bulk material possesses a relatively strong band around 1615 cm^{-1} with a shoulder about 1673 cm^{-1} which can be attributed to C=C stretching and the tertiary amide C=O stretching, respectively. The absence of these bands in the Jeff/DEAA array spot led to the impression that the spots were composed only of Jeffamine and that the DEAAm was still evaporating during the printing process, or that the quantities present were too small to be observed in the Raman spectrum.

The Jeff/DEAAm ink system was made up again and different amounts of DEAAm were added to determine whether differences in the spectra could be observed. Where previously the ratio of Jeffamine:DEAA was 1:1, the same ink was made again as well as a 1:3 and a 1:5 ratio of Jeffamine:DEAA for comparison. Arrays were printed and the Raman spectra were obtained from the spots containing each different ratio (Figure 5.17). However, even when the ink contains 5:1 DEAA:Jeffamine, the spectrum of the array spot is still lacking the bands in the C=C and C=O stretch region and the spots still appear to be composed of Jeffamine only.

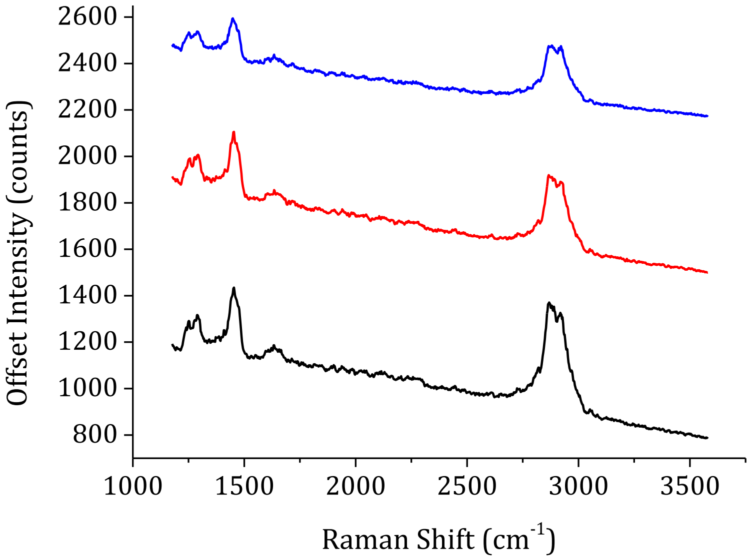

Figure 5.17. *Raman spectra of the array spots with increasing ratio of DEAAm:Jeffamine. 1:1 (black) 3:1 (red) and 5:1 (blue). Spectra were collected using 633 nm laser excitation and 5 x 10 second accumulations. For ease off illustration, spectra are stacked using offset Y values.*

Although the printed array spots did not appear to have the desired composition, the successful fabrication of arrays was still achieved. Therefore, along with the Jeffamine only, the Jeff/DEAAm arrays were carried forward into the next stage of the investigation to allow a comparison of the two systems to be made.

5.3 Characterisation of Thermoresponsive Behaviour

The main purpose of this work was to produce polymer arrays which undergo changes in response to variation in temperature. It was therefore critical to characterise the thermoresponsive behaviour of the arrays on the surface to determine whether or not a response could be observed. Although the bulk swelling properties of the systems had been investigated, it was essential to confirm that the microspots exhibited similar behaviour when attached to a surface.

Initially, Raman spectroscopy was used to investigate any structural changes which take place as a result of the interactions between the polymer and water molecules across the LCST. Schmidt and Dybal previously used changes in the Raman spectra to characterise structural changes in the polymer-water systems and to determine the effects different functional groups have on the interactions and thus on the spectral changes.[216-217]

After the successful fabrication of the polymer arrays, the Raman spectra of the array spots were collected before they were placed in $dddH_2O$ and left for 72 hours to reach equilibrium swelling, in the same way as the bulk material. Spectra in water at room temperature were then obtained prior to heating to 37 °C and leaving for 72 hours to allow the system to equilibrate. Raman spectra were then collected at this increased temperature and the spectra for each stage could be compared. The same process was followed for both the

Jeffamine and the Jeff/DEAAm arrays and the resulting spectra are shown in Figure 5.18 (a) and (b), respectively.

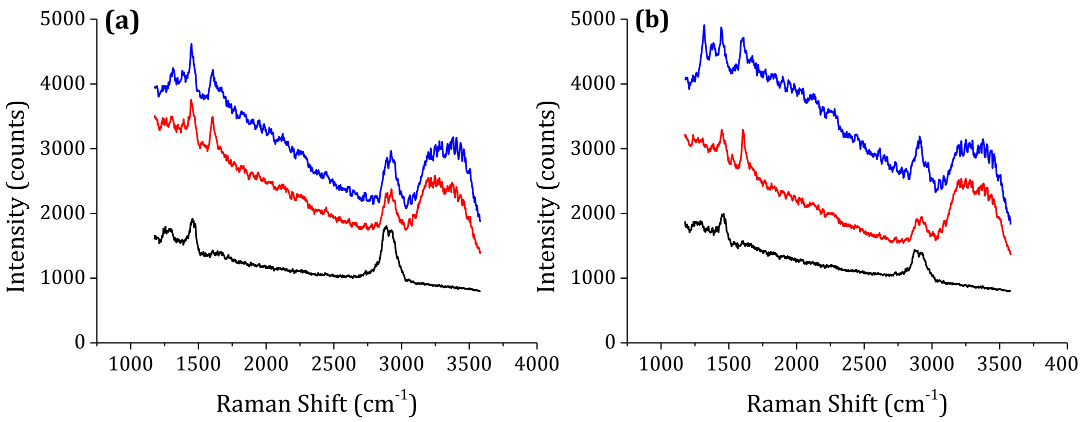

Figure 5.18. *Raman spectra of* ***(a)*** *Jeffamine only and* ***(b)*** *Jeff-DEAAm dry array spots (black) array spots in water at RT (red) and array spots in water with heating (blue). All spectra were collected using 633 nm laser excitation and 5 x 10 second accumulations. Spectra in water were obtained using a 60x water immersion objective and temperature control was achieved using a heated stage.*

When placed in water, the appearance of an OH stretching mode between 3000 cm^{-1} and 3500 cm^{-1} and the OH bending mode around 1600 cm^{-1} can be observed. The observed OH stretch is broad and flat which can be attributed to the interaction of the water molecules with polymer and thus the restriction in position and orientation of the water molecules. There is also a shift in frequency in the OH bending mode upon heating, as well as an increase in intensity and narrowing of the band, which is typically found due to the weakening of hydrogen bonds and the strengthened OH bonds.[218]

Furthermore, there is a change in the ratio of the symmetric and asymmetric stretches (~ 2880 cm^{-1} and 2920 cm^{-1}) when the arrays are in water. The area under the peaks was calculated in order to compare the peak ratios more accurately and it was observed that the peak ratio of the symmetric CH stretch : asymmetric CH stretch decreased between the dry arrays and arrays in water then increased to an intermediate point upon heating (Table 5.2). This indicates that the decrease is coinciding with increasing water content and thus confirms the thermo-induced changes in the polymer array spots. It is also shown here that the ratio of the OH stretch : CH stretch changes significantly before and after heating and the decrease in this ratio is consistent with water being expelled on collapsing or deswelling of the polymer microspot. Additionally, all of the changes which can be observed are more significant in the Jeffamine/DEAAm than in the Jeffamine alone indicating that the thermoresponsive properties are greater in this system. Therefore, even although the spectrum of the Jeff/DEAAm microspot did not match that of the bulk material and it appeared that the spots were composed only of Jeffamine, there is an improvement in the swelling properties of the mixed system when compared to the Jeffamine alone thus suggesting that the polyacrylamide chains may still be present in the printed arrays.

Table 5.2. *Calculated peak ratios for Jeffamine and Jeff/DEAAm array spots to compare the dry spots with those immersed in water at RT and when heated to 37 °C.*

	Peak Ratio (CH Stretch:CH Stretch)	**Peak Ratio (OH Stretch:CH Stretch)**
Dry Arrays	Jeffamine: 1.3 Jeff/DEAAm: 1.5	-
Before Heating	Jeffamine: 0.9 Jeff/DEAAm: 0.7	Jeffamine: 9.7 Jeff/DEAAm: 15.3
After Heating	Jeffamine: 1.1 Jeff/DEAAm: 0.8	Jeffamine: 7.5 Jeff/DEAAm: 9.2

Further to the changes in hydration state which could be observed using Raman spectroscopy, it was important to determine whether the arrays exhibited a change in topography corresponding to the collapse of the polymer chains. AFM was used to image the array spots before and after heating and the resulting images were compared in order to confirm whether or not a change in topography had occurred.

In the same way as before, printed arrays were placed in water and left for three days to reach equilibrium swelling. AFM images were collected then the temperature was set to 37 °C and the arrays were left to equilibrate for three more days prior to AFM analysis at the increased temperature. The registration marks on the silicon dioxide surface were used as an aid to ensure that the same spots were scanned before and after heating in order to ensure a fair comparison. Figure 5.19 shows an example of the height profile of a Jeff/DEAAm array spot before (red) and after (blue) heating. The insets are the AFM topography images from which the height profiles were obtained with the white lines indicating the precise location of the height profiles.

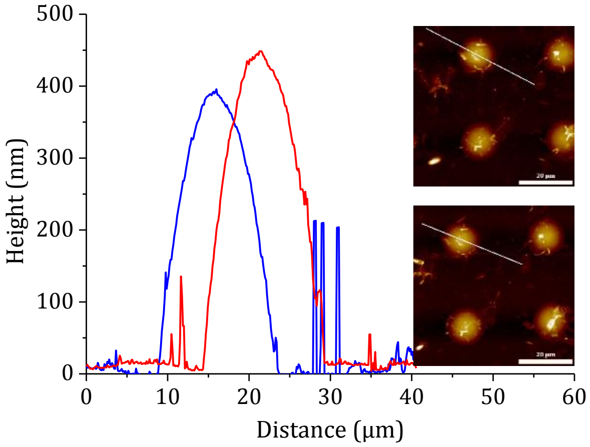

Figure 5.19. *AFM height profile for Jeff/DEAAm in water before (red) and after (blue) heating. Inset: top and bottom are AFM images before and after heating, respectively. White lines indicate where height profile is from. Scale bar = 20 µm.*

The height profiles in Figure 5.19 show that the Jeff/DEAAm spot has decreased in height and increased in diameter upon heating. This is consistent with the polymer collapsing or deswelling across the LCST. For both the Jeffamine and the Jeff/DEAAm, three spots were analysed before and after heating and the average changes in height and diameter can be observed in Table 5.3. It is clear here that both systems show a change in spot height and diameter with heating and that the changes are more significant in the Jeff/DEAAm than in the Jeffamine alone thus further confirming that the introduction of DEAAm into the system has improved the thermoresponsive properties of the polymer arrays.

Table 5.3. *Changes in height and diameter of the Jeffamine and Jeff/DEAAm arrays with heating.*

	Average Height Change (nm)	**Average Diameter Change (µm)**
Jeffamine	-33 ± 6.1	+0.23 ± 0.11
Jeffamine/DEAAm	-68 ± 12.6	+0.60 ± 0.05

The changes in height and diameter of the array spots which were observed across the transition temperature indicate that the polymer microstructures are undergoing a temperature-induced change in topography. This controlled change in topography, along with the spatial control and control over feature size, could potentially be useful in controlling cellular interactions.

5.4 Control of Cellular Interactions

As previously discussed, changes in topography can influence the behaviour of cells on a surface because these changes reflect topographical variations which occur in the cell's natural environment.[40, 219-220] Furthermore, thermoresponsive polymer substrates have been used extensively to control cell attachment and detachment.[183, 188, 199]

The thermoresponsive polymer arrays which have been fabricated in this work undergo both chemical and topographical changes in response to temperature variation across a LCST. These changes could be useful in manipulating the behaviour of cells and therefore this application was investigated.

Since the Jeff/DEAAm arrays underwent the largest temperature-induced changes, these were selected for the cellular studies. Arrays were printed using a 1 s dwell time so that spots greater than 10 μm in diameter and 650 nm in height could be produced. Spots of this size were considered most suitable for these experiments as the larger diameter could potentially allow them to act as a platform for the cell nucleus while the height should be low enough to allow the cells to spread over multiple features.

The pitch of the arrays was also deemed important because variations in the pitch meant that cells could have access to more or less features which could potentially influence their behaviour. For this reason, two different pitches were investigated: 22 μm spacing and 100 μm spacing. Since the cells are typically around 100 μm or more, it was envisaged that on the surfaces with spots printed 22 μm apart, they could potentially have access to many features per cell whereas on the arrays of 100 μm pitch, each cell should only have access to one spot. As a control measure, a planar surface with no arrays but with the same surface chemistry was also investigated for comparison.

The initial experiment was to determine whether the surfaces were biocompatible and if the Le2 endothelial cells would grow on each of the substrates before testing whether detachment of the cells would occur on reducing the temperature. Cell sheets were cultured on each of the surfaces for 7 days at 37 °C and they were found to be growing well. Therefore, the temperature was decreased to 33 °C and left overnight but no signs of detachment were observed and they obtained normal cell morphology. Unfortunately, since the surfaces are non-transparent, it wasn't possible to collect images at this stage without fixing and staining.

However, since the cells survived well at both 37 °C and 33 °C, it was decided to compare the cell behaviour on the different surfaces and so the cells were fixed at 33 °C after 2 days of culture and stained for focal adhesions, actin and DNA. This way the cell attachment, spreading and cytoskeletal organisation could be compared on the different surfaces for cells cultured at the lower temperature.

For cell staining, three different fluorescent dyes were used: tetramethyl rhodamine isothiocyanate (TRITC) for staining actin and gaining information on the cytoskeleton; fluorescein isothiocyanate (FITC) for vinculin staining to identify focal adhesions; and 4′,6-diamidino-2-phenylindole (DAPI) for DNA and thus nuclear staining. Selected images of each of the three surfaces for the three individual stains can be observed in Figure 5.20.

All of the surfaces showed excellent biocompatibility, allowing the cells to attach and grow well with good spreading (Figure 5.20). On the planar surfaces

(Figure 5.20 (a), (d) and (g)), the cells appeared to be forming multi-layered sheets. However, this was occurring to a much lesser extent on the patterned surfaces; particularly on the surface with 22 μm spacing (Figure 5.20 (b), (e) and (h) where the cells seemed to be growing in more of a monolayer. This suggests that either the cells are growing faster on the planar surface, or that the patterns are promoting monolayer growth.

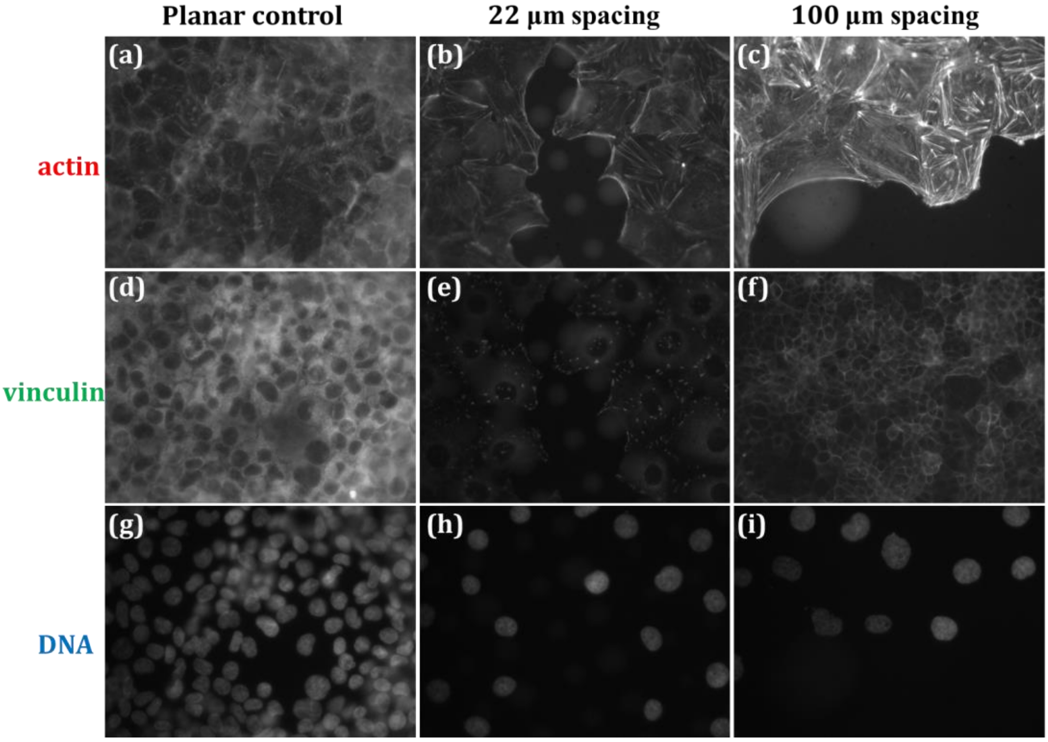

Figure 5.20. *Fluorescent images of the cells on the planar surface* ***(a), (d)*** *and* ***(g)****, the surface with arrays spaced 22 μm apart* ***(b)****,* ***(e)*** *and* ***(h)*** *and the surface with arrays spaced 100 μm apart* ***(c), (f)*** *and* ***(i)****. Different filters were used to show different components of the cell:* ***(a)****,* ***(b)*** *and* ***(c)*** *show the TRITC stained actin;* ***(d)****,* ***(e)*** *and* ***(f)*** *show the FITC stained vinculin and* ***(g)****,* ***(h)*** *and* ***(i)*** *show the DNA stained by DAPI. Cell images are courtesy of Dr. Laura E. McNamara, Glasgow University.*

Of the three substrates, the cell behaviour looked best on the surface with 22 μm spacing where the cells had contact with more features. It appears that the cytoskeleton is better developed in the cells on the 22 μm spaced surface as the actin stress fibres are more defined (Figure 5.20 (b)) whereas on the planar surface (Figure 5.20 (a)), mainly cortical actin at the cell periphery can be seen. Furthermore, it appeared that the cells were directly interacting with the features and better focal adhesions had formed on this substrate, indicating more cell attachment on the surface. This can be observed in Figure 5.20 (e) where the focal adhesions are indicated by the small lines and are more abundant and well-defined than those in Figure 5.20 (d) and (f), where it is difficult to see individual focal adhesions due to the high confluency of the cells.

Figure 5.21 shows overlayed images where each of the three stains can be visualised simultaneously. The confluent, multi-layered growth of the cells on the planar surface can be observed in Figure 5.21 (a). Figure 5.21 (b) shows the cells on the 22 μm spaced substrate interacting with the features. Figure 5.21 (b) has been taken with a higher magnification to show a space between cells, where the interaction with the substrate can be observed. However, for the planar surface (Figure 5.21 (a)) no such areas could be found and therefore the lower magnification gives a better representation of the behaviour across the substrate.

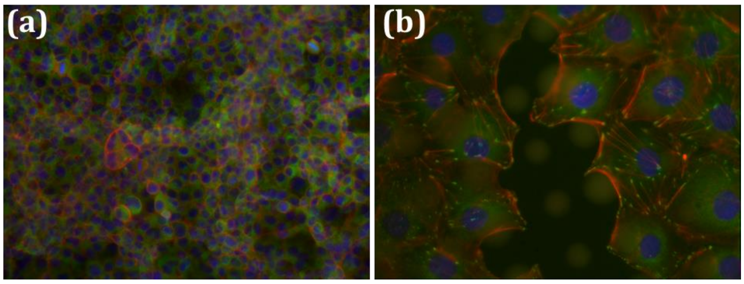

Figure 5.21. *Overlayed fluorescent images of the planar control* ***(a)*** *and the substrate containing arrays spaced 22 μm apart* ***(b)****. In* ***(a)*** *a 20x objective was used to show a representative area and in* ***(b)*** *a 40x objective was used to illustrate the interaction of the cells with the printed polymer features. Images courtesy of Dr. Laura E. Mcnamara.*

These preliminary experiments give an indication of how the cells behave on the polymer surfaces and show that they are indeed biocompatible and that different behaviour can be observed by altering the dimensions of the arrays. This indicates that the substrates may be suitable for the control of cellular interactions; however, in order to obtain more information about how the cells will respond to the temperature-induced change in the features, further experimentation would be required where the behaviour of the cells would be compared across the transition temperature.

5.5 Concluding Remarks

The work discussed in this chapter involved the optimisation of a suitable ink system for the patterning of thermoresponsive polymer arrays by DPN with precise control over feature size and location. Various monomers were investigated for their patterning suitability and it was found that printing NIPAAm posed difficulties using liquid ink transport since the monomer was solid and a suitable carrier matrix was not determined. Arrays of DEAAm could be fabricated but the volatility of the monomer resulted in evaporation from the printed spots. Successful array fabrication, however, was achieved for the printing of Jeffamine ED-600 which could also be combined with DEAAm to produce consistent arrays on a thiol-silanised silicon dioxide surface.

The thermoresponsive behaviour of the arrays of Jeffamine ED-600 and Jeff/DEAAm was characterised by Raman spectroscopy and AFM and a temperature-induced change in hydration state and topography were observed. The response obtained from the Jeff/DEAAm mixed system was intermediary of the response observed for the ink components individually, indicating that the Jeffamine ED-600 could act as a carrier matrix for the DEAAm, preventing the evaporation of this component. Although the Raman spectrum of the Jeff/DEAAm spots appeared to arise from the Jeffamine ED-600 alone, improvement in the thermoresponsive properties of the arrays indicated that the DEAAm polymer chains must be present in the microspots, albeit in low abundance. However, the observed improvement in the thermosensitivity is significant and so the novel combination of the two ink systems was successful.

The highly tuneable properties of the switchable substrates fabricated in this work make them potentially suitable in a range of applications. Preliminary experiments were carried out to test their suitability for the control of cellular interactions and the biocompatibility of the surfaces was confirmed. It was indicated that the behaviour of the cells changed depending on the dimensions of the arrays; however this area requires further investigation.

It would be particularly interesting to compare the behaviour of cells at two different culture temperatures, above and below the LCST, to determine whether or not the temperature-induced changes in feature height will alter the cellular interactions and whether changes in the cell morphology can be observed with changing temperature.

6. Conclusions

This work has demonstrated the use of Raman spectroscopy and dip-pen nanolithography, both individually and as synergic techniques, for a variety of useful applications.

The detection of key biomarkers by resonance Raman scattering was shown to improve sensitivity over the traditional colorimetric detection method in a conventional ELISA. Resonance Raman spectra were not affected in the presence of serum or other cytokines, and gave comparable results to methods currently utilised, thus indicating that the method may be suitable for use in a clinical setting.

An adaptation of this improved detection technique was combined with the advantages of DPN for the fabrication of protein arrays, resulting in immunoassay arrays which were successfully applied for the detection of PSA. The detection of a stable, coloured microspot produced via DPN and an enzyme-based reaction was achieved via resonance Raman mapping with excellent quantification capabilities and a long dynamic range. This was the first time the two techniques had been combined in such a way and it is envisaged that further development could lead to the design of a sensitive, multiple target assay for medical diagnosis.

The methods described demonstrate the detection of a common enzyme/substrate system which should enable the application of the techniques for the detection of a variety of key biomarkers with high sensitivity and throughput.

Although SERRS was investigated for further enhancement, it was discovered that RRS was more suitable in this type of assay as it could be simply applied for detection and quantification with the desired sensitivity being achieved.

DPN was also utilised for the successful fabrication of thermoresponsive polymer arrays which have potential application for the control of cellular interactions. Raman scattering was used throughout the design of these substrates for characterising the monomer and polymer materials and also for confirmation of the temperature-induced response. The changes observed using Raman scattering were supported by AFM analysis of the substrates and successful characterisation of the thermoresponsive behaviour of the polymer arrays was achieved.

The work highlighted in this thesis has successfully demonstrated the versatility of Raman spectroscopy and DPN for use in biological applications. Both techniques can be applied extensively and pose great potential for use in the development of various medical devices and technology. The combination of the two techniques could create a powerful tool for bioanalysis and is something which could certainly be explored further.

7. References

1. Wilkins, M. R. In *2D Electrophoresis: From Protein Maps to Genomes*, First Siena Conference, 5-7 September; 1994.
2. Wasinger, V. C.; Cordwell, S. J.; Cerpapoljak, A.; Yan, J. X.; Gooley, A. A.; Wilkins, M. R.; Duncan, M. W.; Harris, R.; Williams, K. L.; Humphery-Smith, I. *Electrophoresis* **1995,** *16* (7), 1090-1094.
3. Wilkins, M. R.; Sanchez, J. C.; Gooley, A. A.; Appel, R. D.; Humphery-Smith, I.; Hochstrasser, D. F.; Williams, K. L. *Biotechnol. Genet. Eng. Rev.* **1996,** *13*, 19-50.
4. Tyers, M.; Mann, M. *Nature* **2003,** *422* (6928), 193-197.
5. Liebler, D. C., *Introduction to Proteomics: Tools for the New Biology*. Humana Press: Totowa, NJ, 2002.
6. Hanash, S. *Nature* **2003,** *422* (6928), 226-232.
7. Hanash, S. M.; Madoz-Gurpide, J.; Misek, D. E. *Leukemia* **2002,** *16* (4), 478-485.
8. Van Eyk, J. E. *Curr. Opin. Mol. Ther.* **2001,** *3* (6), 546-553.
9. Campbell, N. A., *Biology*. Benjamin Cummings: San Francisco, 2002.
10. Suttie, J. W., *Introduction to Biochemistry*. Holt, Rinehart and Winston: New York, 1977.
11. Pauling, L.; Corey, R. B.; Branson, H. R. *Proc. Natl. Acad. Sci. USA* **1951,** *37* (4), 205-211.
12. Pauling, L.; Corey, R. B. *Proc. Natl. Acad. Sci. USA* **1951,** *37* (5), 251-256.
13. Protein Organization. http://www.yellowtang.org/chemistry.php (accessed May 2013).
14. Kasemo, B. *Surf. Sci.* **2002,** *500* (1-3), 656-677.
15. Rifai, N.; Gillette, M. A.; Carr, S. A. *Nat. Biotechnol.* **2006,** *24* (8), 971-983.
16. de Jager, W.; Prakken, B. J.; Bijlsma, J. W. J.; Kuis, W.; Rijkers, G. T. *J. Immunol. Methods* **2005,** *300* (1-2), 124-135.
17. Mathias, P. C.; Ganesh, N.; Cunningham, B. T. *Anal. Chem.* **2008,** *80* (23), 9013-9020.

18. Yalow, R. S.; Berson, S. A. *Nature* **1959,** *184* (4699), 1648-1649.

19. Edwards, R., *Immunoassays : Essential Data*. John Wiley and Sons : Published in association with BIOS Scientific Publishers, Oxford.: Chichester [England], 1996.

20. Rehm, H., *Protein Biochemistry and Proteomics*. Academic: Oxford, 2005.

21. Adaptive Immune Defenses: Antibodies. http://www.virology.ws/2009/07/22/adaptive-immune-defenses-antibodies/ (accessed May 2013).

22. Kohler, G.; Milstein, C. *Nature* **1975,** *256* (5517), 495-497.

23. Hlady, V.; Buijs, J. *Curr. Opin. Biotechnol.* **1996,** *7* (1), 72-77.

24. Blawas, A. S.; Reichert, W. M. *Biomaterials* **1998,** *19* (7-9), 595-609.

25. MacBeath, G.; Schreiber, S. L. *Science* **2000,** *289* (5485), 1760-1763.

26. Miyahara, Y.; Moriizumi, T.; Ichimura, K. *Sens. Actuators* **1985,** *7* (1), 1-10.

27. Tomizaki, K.; Usui, K.; Mihara, H. *FEBS J.* **2010,** *277* (9), 1996-2005.

28. Uetz, P.; Giot, L.; Cagney, G.; Mansfield, T. A.; Judson, R. S.; Knight, J. R.; Lockshon, D.; Narayan, V.; Srinivasan, M.; Pochart, P.; Qureshi-Emili, A.; Li, Y.; Godwin, B.; Conover, D.; Kalbfleisch, T.; Vijayadamodar, G.; Yang, M. J.; Johnston, M.; Fields, S.; Rothberg, J. M. *Nature* **2000,** *403* (6770), 623-627.

29. Zhu, H.; Snyder, M. *Curr. Opin. Chem. Biol.* **2003,** *7* (1), 55-63.

30. Wulfkuhle, J. D.; Liotta, L. A.; Petricoin, E. F. *Nat. Rev. Cancer* **2003,** *3* (4), 267-275.

31. Kijanka, G.; Murphy, D. *J. Proteomics* **2009,** *72* (6), 936-944.

32. Miller, J. C.; Zhou, H. P.; Kwekel, J.; Cavallo, R.; Burke, J.; Butler, E. B.; Teh, B. S.; Haab, B. B. *Proteomics* **2003,** *3* (1), 56-63.

33. Silzel, J. W.; Cercek, B.; Dodson, C.; Tsay, T.; Obremski, R. J. *Clin. Chem.* **1998,** *44* (9), 2036-2043.

34. Woodbury, R. L.; Varnum, S. M.; Zangar, R. C. *J. Proteome Res.* **2002,** *1* (3), 233-237.

35. Irvine, E. J.; Hernandez-Santana, A.; Faulds, K.; Graham, D. *Analyst* **2011,** *136* (14), 2925-2930.

36. Ekins, R. P. *J. Pharm. Biomed. Anal.* **1989,** *7* (2), 155-168.

37. Moody, M. D.; Van Arsdell, S. W.; Murphy, K. P.; Orencole, S. F.; Burns, C. *BioTechniques* **2001,** *31* (1), 186-190.

38. Kambhampati, D., *Protein Microarray Technology*. Wiley-VCH: Weinheim, 2004.

39. Lee, K. B.; Park, S. J.; Mirkin, C. A.; Smith, J. C.; Mrksich, M. *Science* **2002,** *295* (5560), 1702-1705.

40. Chen, C. S.; Mrksich, M.; Huang, S.; Whitesides, G. M.; Ingber, D. E. *Science* **1997,** *276* (5317), 1425-1428.

41. Baac, H. W.; Lee, J. H.; Seo, J. M.; Park, T. H.; Chung, H.; Lee, S. D.; Kim, S. J. *Mater. Sci. Eng. C Biomimetic Supramol. Syst.* **2004,** *24* (1-2), 209-212.

42. Zhu, B. S.; Zhang, Q. Q.; Lu, Q. H.; Xu, Y. H.; Yin, J.; Hu, J.; Wang, Z. *Biomaterials* **2004,** *25* (18), 4215-4223.

43. McNamara, L. E.; McMurray, R. J.; Biggs, M. J. P.; Kantawong, F.; Oreffo, R. O. C.; Dalby, M. J. *J. Tissue Eng.* **2010,** *2010*, 120623-120623.

44. Bettinger, C. J.; Zhang, Z.; Gerecht, S.; Borenstein, J. T.; Langer, R. *Adv. Mater.* **2008,** *20* (1), 99-103.

45. Dalby, M. J.; Andar, A.; Nag, A.; Affrossman, S.; Tare, R.; McFarlane, S.; Oreffo, R. O. C. *J. R. Soc. Interface* **2008,** *5* (26), 1055-1065.

46. Thapa, A.; Webster, T. J.; Haberstroh, K. M. *J. Biomed. Mater. Res., Part A* **2003,** *67A* (4), 1374-1383.

47. Dalby, M. J.; Gadegaard, N.; Tare, R.; Andar, A.; Riehle, M. O.; Herzyk, P.; Wilkinson, C. D. W.; Oreffo, R. O. C. *Nat. Mater.* **2007,** *6* (12), 997-1003.

48. MacNeil, S. *Nature* **2007,** *445* (7130), 874-880.

49. Falconnet, D.; Koenig, A.; Assi, T.; Textor, M. *Adv. Funct. Mater.* **2004,** *14* (8), 749-756.

50. Dalby, M. J.; Gadegaard, N.; Riehle, M. O.; Wilkinson, C. D. W.; Curtis, A. S. G. *Int. J. Biochem. Cell Biol.* **2004,** *36* (10), 2005-2015.

51. Norman, J.; Desai, T. *Ann. Biomed. Eng.* **2006,** *34* (1), 89-101.

52. Truskett, V. N.; Watts, M. P. C. *Trends Biotechnol.* **2006,** *24* (7), 312-317.

53. Hyun, J.; Zhu, Y. J.; Liebmann-Vinson, A.; Beebe, T. P.; Chilkoti, A. *Langmuir* **2001,** *17* (20), 6358-6367.

54. Haaheim, J.; Eby, R.; Nelson, M.; Fragala, J.; Rosner, B.; Zhang, H.; Athas, G. *Ultramicroscopy* **2005,** *103* (2), 117-132.

55. Salaita, K.; Wang, Y.; Mirkin, C. A. *Nat. Nanotechnol.* **2007,** *2* (3), 145-155.

56. Piner, R. D.; Zhu, J.; Xu, F.; Hong, S. H.; Mirkin, C. A. *Science* **1999,** *283* (5402), 661-663.

57. Cheung, F. Dip-pen nanolithography: No double-dipping *Nat. Nanotechnol.* [Online], 2007. http://dx.doi.org/10.1038/nchina.2007.57.

58. Nanoink Inc. http://www.nanoink.net/technology.html (accessed March 2013).

59. Rozhok, S.; Piner, R.; Mirkin, C. A. *J. Phys. Chem. B* **2003,** *107* (3), 751-757.

60. Peterson, E. J.; Weeks, B. L.; De Yoreo, J. J.; Schwartz, P. V. *J. Phys. Chem. B* **2004,** *108* (39), 15206-15210.

61. Hernandez-Santana, A.; Irvine, E.; Faulds, K.; Graham, D. *Chem. Sci.* **2011,** *2* (2), 211-215.

62. Wang, H. T.; Nafday, O. A.; Haaheim, J. R.; Tevaarwerk, E.; Amro, N. A.; Sanedrin, R. G.; Chang, C. Y.; Ren, F.; Pearton, S. J. *Appl. Phys. Lett.* **2008,** *93* (14).

63. Senesi, A. J.; Rozkiewicz, D. I.; Reinhoudt, D. N.; Mirkin, C. A. *ACS Nano* **2009,** *3* (8), 2394-2402.

64. Hung, S.-C.; Nafday, O. A.; Haaheim, J. R.; Ren, F.; Chi, G. C.; Pearton, S. J. *J. Phys. Chem. C* **2010,** *114* (21), 9672-9677.

65. Jang, J. W.; Smetana, A.; Stiles, P. *Scanning* **2010,** *32* (1), 24-29.

66. Demers, L. M.; Mirkin, C. A. *Angew. Chem. Int. Ed.* **2001,** *40* (16), 3069-3071.

67. Zhang, H.; Chung, S. W.; Mirkin, C. A. *Nano Lett.* **2003,** *3* (1), 43-45.

68. Demers, L. M.; Ginger, D. S.; Park, S. J.; Li, Z.; Chung, S. W.; Mirkin, C. A. *Science* **2002,** *296* (5574), 1836-1838.

69. Samorí, P., *Scanning Probe Microscopies Beyond Imaging: Manipulation of Molecules and Nanostructures*. Wiley-VCH: Weinheim, 2006.

70. Lee, M.; Kang, D. K.; Yang, H. K.; Park, K. H.; Choe, S. Y.; Kang, C.; Chang, S. I.; Han, M. H.; Kang, I. C. *Proteomics* **2006,** *6* (4), 1094-1103.

71. Lee, S. W.; Oh, B. K.; Sanedrin, R. G.; Salaita, K.; Fujigaya, T.; Mirkin, C. A. *Adv. Mater.* **2006,** *18* (9), 1133-1136.

72. Li, Y.; Maynor, B. W.; Liu, J. *J. Am. Chem. Soc.* **2001,** *123* (9), 2105-2106.

73. Lee, K. B.; Lim, J. H.; Mirkin, C. A. *J. Am. Chem. Soc.* **2003,** *125* (19), 5588-5589.

74. Lim, J. H.; Ginger, D. S.; Lee, K. B.; Heo, J.; Nam, J. M.; Mirkin, C. A. *Angew. Chem. Int. Ed.* **2003,** *42* (20), 2309-2312.

75. Wu, C. C.; Xu, H. P.; Otto, C.; Reinhoudt, D. N.; Lammertink, R. G. H.; Huskens, J.; Subramaniam, V.; Velders, A. H. *J. Am. Chem. Soc.* **2009,** *131* (22), 7526-7527.

76. Lynch, M.; Mosher, C.; Huff, J.; Nettikadan, S.; Johnson, J.; Henderson, E. *Proteomics* **2004,** *4* (6), 1695-1702.

77. Lee, K. B.; Kim, E. Y.; Mirkin, C. A.; Wolinsky, S. M. *Nano Lett.* **2004,** *4* (10), 1869-1872.

78. Lee, S.; Ko, Y. H.; Jung, H.; Kim, J. D.; Song, J. M.; Chooe, J.; Eo, S. K.; Kang, S. H. *Talanta* **2009,** *78* (2), 608-612.

79. Hyun, J.; Lee, W. K.; Nath, N.; Chilkoti, A.; Zauscher, S. *J. Am. Chem. Soc.* **2004,** *126* (23), 7330-7335.

80. Curran, J. M.; Stokes, R.; Irvine, E.; Graham, D.; Amro, N. A.; Sanedrin, R. G.; Jamil, H.; Hunt, J. A. *Lab Chip* **2010,** *10* (13), 1662-1670.

81. Rakickas, T.; Ericsson, E. M.; Ruzele, Z.; Liedberg, B.; Valiokas, R. *Small* **2011,** *7* (15), 2153-2157.

82. Lim, J. H.; Mirkin, C. A. *Adv. Mater.* **2002,** *14* (20), 1474-+.

83. Hernandez-Santana, A.; Mackintosh, A. R.; Guilhabert, B.; Kanibolotsky, A. L.; Dawson, M. D.; Skabara, P. J.; Graham, D. *J. Mater. Chem.* **2011,** *21* (37), 14209-14212.

84. Su, M.; Aslam, M.; Fu, L.; Wu, N. Q.; Dravid, V. P. *Appl. Phys. Lett.* **2004,** *84* (21), 4200-4202.

85. Huang, L.; Braunschweig, A. B.; Shim, W.; Qin, L.; Lim, J. K.; Hurst, S. J.; Huo, F.; Xue, C.; Jang, J. W.; Mirkin, C. A. *Small (Weinheim an der Bergstrasse, Germany)* **2010,** *6* (10), 1077-1081.

86. Charest, J. L.; Eliason, M. T.; Garcia, A. J.; King, W. P. *Biomaterials* **2006,** *27* (11), 2487-2494.

87. Dalby, M. J.; Riehle, M. O.; Sutherland, D. S.; Agheli, H.; Curtis, A. S. G. *J. Biomed. Mater. Res., Part A* **2004,** *69A* (2), 314-322.

88. Ray, S.; Mehta, G.; Srivastava, S. *Proteomics* **2010,** *10* (4), 731-748.

89. McDonnell, J. M. *Curr. Opin. Chem. Biol.* **2001,** *5* (5), 572-577.

90. Campagnolo, C.; Meyers, K. J.; Ryan, T.; Atkinson, R. C.; Chen, Y. T.; Scanlan, M. J.; Ritter, G.; Old, L. J.; Batt, C. A. *J. Biochem. Biophys. Methods* **2004,** *61* (3), 283-298.

91. de Boer, A. R.; Hokke, C. H.; Deelder, A. M.; Wuhrer, M. *Glycoconjugate J.* **2008,** *25* (1), 75-84.

92. Lausted, C.; Hu, Z. Y.; Hood, L. *Mol. Cell. Proteomics* **2008,** *7* (12), 2464-2474.

93. Ji, J.; O'Connell, J. G.; Carter, D. J. D.; Larson, D. N. *Anal. Chem.* **2008,** *80* (7), 2491-2498.

94. Binnig, G.; Quate, C. F.; Gerber, C. *Phys. Rev. Lett.* **1986,** *56* (9), 930-933.

95. Tortonese, M.; Barrett, R. C.; Quate, C. F. *Appl. Phys. Lett.* **1993,** *62* (8), 834-836.

96. Glökler, J.; Angenendt, P. *J. Chromatogr. B* **2003,** *797* (1-2), 229-240.

97. Biebricher, A.; Paul, A.; Tinnefeld, P.; Golzhauser, A.; Sauer, M. *J. Biotechnol.* **2004,** *112* (1-2), 97-107.

98. Ide, T.; Nishida, K.; Yamato, M.; Sumide, T.; Utsumi, M.; Nozaki, T.; Kikuchi, A.; Okano, T.; Tano, Y. *Biomaterials* **2006,** *27* (4), 607-614.

99. Strutt, J. W. *Philos. Mag.* **1871,** *41* (4), 107.

100. Raman, C. V. a. K., K.S. *Nature* **1928,** *121*, 501-502.

101. Smith, E., *Modern Raman Spectroscopy : A Practical Approach*. John Wiley and Sons: Chichester, 2005.

102. Jensen, L.; Zhao, L. L.; Autschbach, J.; Schatz, G. C. *J. Chem. Phys.* **2005,** *123* (17).

103. Fleischmann, M.; Hendra, P. J.; Mcquillan, A. J. *Chem. Phys. Lett.* **1974,** *26* (2), 163-166.

104. Jeanmaire, D. L.; Vanduyne, R. P. *J. Electroanal. Chem.* **1977,** *84* (1), 1-20.

105. Albrecht, M. G.; Creighton, J. A. *J. Am. Chem. Soc.* **1977,** *99* (15), 5215-5217.

106. Moskovits, M. *Rev. Mod. Phys.* **1985,** *57* (3), 783-826.

107. Otto, A. *J. Raman Spectrosc.* **1991,** *22* (12), 743-752.

108. Stokes, R. J.; Macaskill, A.; Lundahl, P. J.; Smith, W. E.; Faulds, K.; Graham, D. *Small* **2007,** *3*, 1593-1601.

109. Larmour, I. A.; Faulds, K.; Graham, D. *Anal. Methods* **2010,** *2* (9), 1230-1232.

110. Gendrin, C.; Roggo, Y.; Collet, C. *J. Pharm. Biomed. Anal.* **2008,** *48* (3), 533-553.

111. Kneipp, K.; Haka, A. S.; Kneipp, H.; Badizadegan, K.; Yoshizawa, N.; Boone, C.; Shafer-Peltier, K. E.; Motz, J. T.; Dasari, R. R.; Feld, M. S. *Appl. Spectrosc.* **2002,** *56* (2), 150-154.

112. Combs, Z. A.; Chang, S.; Clark, T.; Singamaneni, S.; Anderson, K. D.; Tsukruk, V. V. *Langmuir* **2011,** *27* (6), 3198-3205.

113. Schmidt, M. W.; Baldridge, K. K.; Boatz, J. A.; Elbert, S. T.; Gordon, M. S.; Jensen, J. H.; Koseki, S.; Matsunaga, N.; Nguyen, K. A.; Su, S. J.; Windus, T. L.; Dupuis, M.; Montgomery, J. A. *J. Comput. Chem.* **1993,** *14* (11), 1347-1363.

114. Frisch, M. J.; Trucks, G. W.; Schlegel, H. B.; Scuseria, G. E.; Robb, M. A.; Cheeseman, J. R.; Jr., J. A. M.; Vreven, T.; Kudin, K. N.; Burant, J. C.; Millam, J. M.; Lyengar, S. S.; Tomasi, J.; Barone, V.; Mennucci, B.; Cossi, M.; Scalmani, G.; Rega, N.; Petersson, G. A.; Nakatsuji, H.; Hada, M.; Ehara, M.; Toyota, K.; Fukuda, R.; Hasegawa, J.; Ishida, M.; Nakajima, T.; Honda, Y.;

Kitao, O.; Nakai, H.; Klene, M.; Li, X.; Knox, J. E.; Hratchian, H. P.; Cross, J. B.; Adamo, C.; Jaramillo, J.; Gomperts, R.; Stratmann, R. E.; Yazyev, O.; Austin, A. J.; Cammi, R.; Pomelli, C.; Ochterski, J. W.; Ayala, P. Y.; Morokuma, K.; Voth, G. A.; Salvador, P.; Dannenberg, J. J.; Zakrzewski, V. G.; Dapprich, S.; Daniels, A. D.; Strain, M. C.; Farkas, O.; Malick, D. K.; Rabuck, A. D.; Raghavachari, K.; Foresman, J. B.; Ortiz, J. V.; Cui, Q.; Baboul, A. G.; Clifford, S.; Cioslowski, J.; Stefanov, B. B.; Liu, G.; Liashenko, A.; Piskorz, P.; Komaromi, I.; Martin, R. L.; Fox, D. J.; Keith, T.; Al-Laham, M. A.; Peng, C. Y.; Nanayakkara, A.; Challacombe, M.; Gill, P. M. W.; Johnson, B.; Chen, W.; Wong, M. W.; Gonzalez, C.; Pople, J. A., Gaussian, Inc. Gaussian, Inc., Pittsburgh PA, 2004.

115. Becke, A. D. *Phys. Rev. A* **1988,** *38* (6), 3098-3100.
116. Perdew, J. P. *Phys. Rev. B* **1986,** *33* (12), 8822-8824.
117. Grimme, S. *J. Comput. Chem.* **2006,** *27* (15), 1787-1799.
118. Turkevich, J.; Stevenson, P. C.; Hillier, J. *Discuss. Faraday Soc.* **1951,** (11), 55-75.
119. Wisdom, G. B. *Clin. Chem.* **1976,** *22* (8), 1243-1255.
120. Deshpande, S. S., *Enzyme Immunoassays: From Concepts to Product Development*. Kruwer Academic Publishers: Dordrecht, 1996.
121. Porstmann, T.; Kiessig, S. T. *J. Immunol. Methods* **1992,** *150* (1-2), 5-21.
122. Volpe, G.; Compagnone, D.; Draisci, R.; Palleschi, G. *Analyst* **1998,** *123* (6), 1303-1307.
123. Fanjul-Bolado, P.; Gonzalez-Garia, M. B.; Costa-Garcia, A. *Anal. Bioanal. Chem.* **2005,** *382* (2), 297-302.
124. Baldrich, E.; del Campo, F. J.; Munoz, F. X. *Biosens. Bioelectron.* **2009,** *25* (4), 920-926.
125. Liu, M. L.; Zhang, Y. Y.; Chen, Y. D.; Xie, Q. J.; Yao, S. Z. *J. Electroanal. Chem.* **2008,** *622* (2), 184-192.
126. Josephy, P. D.; Eling, T.; Mason, R. P. *J. Biol. Chem.* **1982,** *257* (7), 3669-3675.

127. Marquez, L. A.; Dunford, H. B. *Biochemistry (Mosc).* **1997,** *36* (31), 9349-9355.

128. Misono, Y.; Ohkata, Y.; Morikawa, T.; Itoh, K. *J. Electroanal. Chem.* **1997,** *436* (1-2), 203-212.

129. Boilet, L.; Buntinx, G.; Lapouge, C.; Lefumeux, C.; Poizat, O. *PCCP* **2003,** *5* (5), 834-842.

130. Guichard, V.; Bourkba, A.; Poizat, O.; Buntinx, G. *J. Phys. Chem.* **1989,** *93* (11), 4429-4435.

131. Barbara, J. A. J.; VanOstade, X.; Lopez, A. F. *Immunol. Cell Biol.* **1996,** *74* (5), 434-443.

132. Tang, P.; Hung, M. C.; Klostergaard, J. *Biochemistry (Mosc).* **1996,** *35* (25), 8216-8225.

133. Black, R. A. *Int. J. Biochem. Cell Biol.* **2002,** *34* (1), 1-5.

134. Eck, M. J.; Sprang, S. R. *J. Biol. Chem.* **1989,** *264* (29), 17595-17605.

135. Perez, C.; Albert, I.; Defay, K.; Zachariades, N.; Gooding, L.; Kriegler, M. *Cell* **1990,** *63* (2), 251-258.

136. Tetta, C.; Camussi, G.; Modena, V.; Divittorio, C.; Baglioni, C. *Ann. Rheum. Dis.* **1990,** *49* (9), 665-667.

137. Ettehadi, P.; Greaves, M. W.; Wallach, D.; Aderka, D.; Camp, R. D. R. *Clin. Exp. Immunol.* **1994,** *96* (1), 146-151.

138. D'Haens, G. *Curr. Pharm. Des.* **2003,** *9* (4), 289-294.

139. Mira, J. P.; Cariou, A.; Grall, F.; Delclaux, C.; Losser, M. R.; Heshmati, F.; Cheval, C.; Monchi, M.; Teboul, J. L.; Riche, F.; Leleu, G.; Arbibe, L.; Mignon, A.; Delpech, M.; Dhainaut, J. F. *J. Am. Med. Assoc.* **1999,** *282* (6), 561-568.

140. Galic, S.; Oakhill, J. S.; Steinberg, G. R. *Mol. Cell. Endocrinol.* **2010,** *316* (2), 129-139.

141. Urszula, T. M.; Jerzy, L.; Bozena, K.; Ewa, F.; Agata, K.; Anna, N.; Tomasz, M. *Ginekol. Pol.* **2010,** *81* (3), 192-196.

142. *Thermo Scientific Human TNF-a ELISA Kit (EH3TNFA)*. Pierce Biotechnology: 2009.

143. el-Shirbiny, A. M. *Adv. Clin. Chem.* **1994,** *31*, 99-133.

144. Wang, M. C.; Valenzuela, L. A.; Murphy, G. P.; Chu, T. M. *Invest. Urol.* **1979,** *17* (2), 159-163.

145. Papsidero, L. D.; Wang, M. C.; Valenzuela, L. A.; Murphy, G. P.; Chu, T. M. *Cancer Res.* **1980,** *40* (7), 2428-2432.

146. Stamey, T. A.; Yang, N.; Hay, A. R.; McNeal, J. E.; Freiha, F. S.; Redwine, E. *New Engl. J. Med.* **1987,** *317* (15), 909-916.

147. Schifman, R. B.; Ahmann, F. R.; Elvick, A.; Ahmann, M.; Coulis, K.; Brawer, M. K. *Clin. Chem.* **1987,** *33* (11), 2086-2088.

148. Dhanasekaran, S. M.; Barrette, T. R.; Ghosh, D.; Shah, R.; Varambally, S.; Kurachi, K.; Pienta, K. J.; Rubin, M. A.; Chinnaiyan, A. M. *Nature* **2001,** *412* (6849), 822-826.

149. Yu, H.; Diamandis, E. P.; Sutherland, D. J. A. *Clin. Biochem.* **1994,** *27* (2), 75-79.

150. Melegos, D. N.; Diamandis, E. P. *Clin. Biochem.* **1996,** *29* (3), 193-200.

151. Ward, A. M.; Catto, J. W. F.; Hamdy, F. C. *Ann. Clin. Biochem.* **2001,** *38*, 633-651.

152. Stevenson, R.; Ingram, A.; Leung, H.; McMillan, D. C.; Graham, D. *Analyst* **2009,** *134* (5), 842-844.

153. McKeating, K. S.; Graham, D.; Faulds, K. *Chem. Commun.* **2013,** *49* (31), 3206-3208.

154. Jv, Y.; Li, B.; Cao, R. *Chem. Commun.* **2010,** *46* (42), 8017-8019.

155. Wang, S.; Chen, W.; Liu, A. L.; Hong, L.; Deng, H. H.; Lin, X. H. *ChemPhysChem* **2012,** *13* (5), 1199-1204.

156. Gul, O.; Calay, E.; Sezerman, U.; Basaga, H.; Gurbuz, Y. *Sens. Actuators, B* **2007,** *125* (2), 581-588.

157. Jenison, R.; La, H.; Haeberli, A.; Ostroff, R.; Polisky, B. *Clin. Chem.* **2001,** *47* (10), 1894-1900.

158. Kusnezow, W.; Jacob, A.; Walijew, A.; Diehl, F.; Hoheisel, J. D. *Proteomics* **2003,** *3* (3), 254-264.

159. Irvine, E. J. Fabricating Protein Arrays Using Dip-Pen Nanolithography Techniques For Improved Sensitivity of Biomarker Detection. University of Strathclyde, Glasgow, 2012.
160. Gershoni, J. M.; Palade, G. E. *Anal. Biochem.* **1983,** *131* (1), 1-15.
161. Yin, L. T.; Hu, C. Y.; Chang, C. H. *Sens. Actuators, B* **2008,** *130* (1), 374-378.
162. Stillman, B. A.; Tonkinson, J. L. *BioTechniques* **2000,** *29* (3), 630-635.
163. Borrebaeck, C. A. K.; Wingren, C. *J. Proteomics* **2009,** *72* (6), 928-935.
164. Hook, A. L.; Voelcker, N. H.; Thissen, H. *Acta Biomater.* **2009,** *5* (7), 2350-2370.
165. Kopecek, J. *Biomaterials* **2007,** *28* (34), 5185-5192.
166. Lee, K. Y.; Mooney, D. J. *Chem. Rev.* **2001,** *101* (7), 1869-1879.
167. Molina, I.; Li, S. M.; Martinez, M. B.; Vert, M. *Biomaterials* **2001,** *22* (4), 363-369.
168. Wang, B. Q.; Li, B.; Deng, Q.; Dong, S. J. *Anal. Chem.* **1998,** *70* (15), 3170-3174.
169. Zhou, M.; Smith, A. M.; Das, A. K.; Hodson, N. W.; Collins, R. F.; Ulijn, R. V.; Gough, J. E. *Biomaterials* **2009,** *30* (13), 2523-2530.
170. Eddington, D. T.; Beebe, D. J. *Adv. Drug Del. Rev.* **2004,** *56* (2), 199-210.
171. Drury, J. L.; Mooney, D. J. *Biomaterials* **2003,** *24* (24), 4337-4351.
172. Dulong, V.; Le Cerf, D.; Picton, L.; Muller, G. *Colloids Surf., A* **2006,** *274* (1-3), 163-169.
173. Graziano, G. *Int. J. Biol. Macromol.* **2000,** *27* (1), 89-97.
174. Lee, H. I.; Wu, W.; Oh, J. K.; Mueller, L.; Sherwood, G.; Peteanu, L.; Kowalewski, T.; Matyjaszewski, K. *Angew. Chem. Int. Ed.* **2007,** *46* (14), 2453-2457.
175. Kumar, A.; Galaev, I. Y.; Mattiasson, B. *Biotechnol. Bioeng.* **1998,** *59* (6), 695-704.
176. Shiga, T., Deformation and viscoelastic behavior of polymer gels in electric fields. In *Neutron Spin Echo Spectroscopy Viscoelasticity Rheology*, 1997; Vol. 134, pp 131-163.
177. Dusek, K.; Patterso.D *J. Polym. Sci., Part A-2* **1968,** *6* (7PA2), 1209-1216.

178. Tanaka, T.; Nishio, I.; Sun, S. T.; Uenonishio, S. *Science* **1982,** *218* (4571), 467-469.

179. Tanaka, T. *Phys. Rev. Lett.* **1978,** *40* (12), 820-823.

180. Tanaka, T.; Fillmore, D.; Sun, S. T.; Nishio, I.; Swislow, G.; Shah, A. *Phys. Rev. Lett.* **1980,** *45* (20), 1636-1639.

181. Ohmine, I.; Tanaka, T. *J. Chem. Phys.* **1982,** *77* (11), 5725-5729.

182. Suzuki, A.; Tanaka, T. *Nature* **1990,** *346* (6282), 345-347.

183. Brun-Graeppi, A. K. A. S.; Richard, C.; Bessodes, M.; Scherman, D.; Merten, O.-W. *Prog. Polym. Sci.* **2010,** *35* (11), 1311-1324.

184. Schmaljohann, D. *Adv. Drug Del. Rev.* **2006,** *58* (15), 1655-1670.

185. Otake, K.; Inomata, H.; Konno, M.; Saito, S. *Macromolecules* **1990,** *23* (1), 283-289.

186. Lin, S. Y.; Chen, K. S.; Liang, R. C. *Polymer* **1999,** *40* (10), 2619-2624.

187. Dumitriu, R. P.; Mitchell, G. R.; Vasile, C. *Polym. Int.* **2011,** *60* (2), 222-233.

188. Okano, T.; Yamada, N.; Okuhara, M.; Sakai, H.; Sakurai, Y. *Biomaterials* **1995,** *16* (4), 297-303.

189. Kushida, A.; Yamato, M.; Konno, C.; Kikuchi, A.; Sakurai, Y.; Okano, T. *J. Biomed. Mater. Res.* **1999,** *45* (4), 355-362.

190. Nagase, K.; Kobayashi, J.; Kikuchi, A.; Akiyama, Y.; Kanazawa, H.; Okano, T. *Langmuir* **2007,** *23* (18), 9409-9415.

191. Canavan, H. E.; Cheng, X. H.; Graham, D. J.; Ratner, B. D.; Castner, D. G. *Langmuir* **2005,** *21* (5), 1949-1955.

192. Zhang, R.; Mjoseng, H. K.; Hoeve, M. A.; Bauer, N. G.; Pells, S.; Besseling, R.; Velugotla, S.; Tourniaire, G.; Kishen, R. E. B.; Tsenkina, Y.; Armit, C.; Duffy, C. R. E.; Helfen, M.; Edenhofer, F.; de Sousa, P. A.; Bradley, M. *Nat. Commun.* **2013,** *4*, 1335-1335.

193. Kavanagh, C. A.; Rochev, Y. A.; Gallagher, W. A.; Dawson, K. A.; Keenan, A. K. *Pharmacol. Ther.* **2004,** *102* (1), 1-15.

194. Ma, D.; Chen, H.; Shi, D.; Li, Z.; Wang, J. *J. Colloid Interface Sci.* **2009,** *332* (1), 85-90.

195. Okano, T.; Bae, Y. H.; Jacobs, H.; Kim, S. W. *J. Controlled Release* **1990,** *11* (1-3), 255-265.

196. Malmstadt, N.; Yager, P.; Hoffman, A. S.; Stayton, P. S. *Anal. Chem.* **2003,** *75* (13), 2943-2949.

197. Suzuki, H. *J. Intell. Mater. Syst. Struct.* **2006,** *17* (12), 1091-1097.

198. Sershen, S. R.; Mensing, G. A.; Ng, M.; Halas, N. J.; Beebe, D. J.; West, J. L. *Adv. Mater.* **2005,** *17* (11), 1366-1368.

199. Yamada, N.; Okano, T.; Sakai, H.; Karikusa, F.; Sawasaki, Y.; Sakurai, Y. *Makromol. Chem., Rapid Commun.* **1990,** *11* (11), 571-576.

200. Canavan, H. E.; Cheng, X. H.; Graham, D. J.; Ratner, B. D.; Castner, D. G. *J. Biomed. Mater. Res. A* **2005,** *75A* (1), 1-13.

201. Yamato, M.; Kwon, O. H.; Hirose, M.; Kikuchi, A.; Okano, T. *J. Biomed. Mater. Res.* **2001,** *55* (1), 137-140.

202. Yamato, M.; Konno, C.; Utsumi, M.; Kikuchi, A.; Okano, T. *Biomaterials* **2002,** *23* (2), 561-567.

203. Yamato, M.; Utsumi, M.; Kushida, A.; Konno, C.; Kikuchi, A.; Okano, T. *Tissue Eng.* **2001,** *7* (4), 473-480.

204. Harimoto, M.; Yamato, M.; Hirose, M.; Takahashi, C.; Isoi, Y.; Kikuchi, A.; Okano, T. *J. Biomed. Mater. Res.* **2002,** *62* (3), 464-470.

205. Shimizu, T.; Yamoto, M.; Kikuchi, A.; Okano, T. *Tissue Eng.* **2001,** *7* (2), 141-151.

206. Matsuda, T. *J. Biomater. Sci., Polym. Ed.* **2004,** *15* (7), 947-955.

207. Bohanon, T.; Elender, G.; Knoll, W.; Koberle, P.; Lee, J. S.; Offenhausser, A.; Ringsdorf, H.; Sackmann, E.; Simon, J.; Tovar, G.; Winnik, F. M. *J. Biomater. Sci., Polym. Ed.* **1996,** *8* (1), 19-39.

208. Jones, D. M.; Huck, W. T. S. *Adv. Mater.* **2001,** *13* (16), 1256-1259.

209. Ahn, S. J.; Kaholek, M.; Lee, W. K.; LaMattina, B.; LaBean, T. H.; Zauscher, S. *Adv. Mater.* **2004,** *16* (23-24), 2141-2145.

210. He, Q.; Kueller, A.; Schilp, S.; Leisten, F.; Kolb, H.-A.; Grunze, M.; Li, J. *Small* **2007,** *3* (11), 1860-1865.

211. Kaholek, M.; Lee, W. K.; LaMattina, B.; Caster, K. C.; Zauscher, S. *Nano Lett.* **2004,** *4* (2), 373-376.

212. Lee, W.-K.; Whitman, L. J.; Lee, J.; King, W. P.; Sheehan, P. E. *Soft Matter* **2008,** *4* (9), 1844-1847.

213. Forney, B. S.; Guymon, C. A. *Macromol. Rapid Commun.* **2011,** *32* (9-10), 765-769.

214. Agut, W.; Brulet, A.; Taton, D.; Lecommandoux, S. *Langmuir* **2007,** *23* (23), 11526-11533.

215. Mocanu, G.; Mihai, D.; Dulong, V.; Picton, L.; Le Cerf, D. *Carbohydr. Polym.* **2012,** *87* (2), 1440-1446.

216. Schmidt, P.; Dybal, J.; Rodriguez-Cabello, J. C.; Reboto, V. *Biomacromolecules* **2005,** *6* (2), 697-706.

217. Dybal, J.; Trchova, M.; Schmidt, P. *Vib. Spectrosc* **2009,** *51* (1), 44-51.

218. Praprotnik, M.; Janezic, D.; Mavri, J. *J. Phys. Chem. A* **2004,** *108* (50), 11056-11062.

219. Singhvi, R.; Stephanopoulos, G.; Wang, D. I. C. *Biotechnol. Bioeng.* **1994,** *43* (8), 764-771.

220. Bettinger, C. J.; Langer, R.; Borenstein, J. T. *Angew. Chem. Int. Ed.* **2009,** *48* (30), 5406-5415.

8. Appendix: Publications

- “Quantitative Detection of Human Tumor Necrosis Factor alpha by a Resonance Raman Enzyme-linked Immunosorbent Assay”, S. Laing, A. Hernandez-Santana, J. Saßmannshausen, D.L. Asquith, I.B. McInnes, K. Faulds, D. Graham. Anal. Chem. 2011, 83 (1), 297-302.

- “Immunoassay Arrays Fabricated by Dip-Pen Nanolithography with Resonance Raman Detection”, S. Laing, E.J. Irvine, A. Hernandez-Santana, W.E. Smith, K. Faulds, D. Graham. Anal. Chem. 2013, 85 (12), 5617-5621.

- “Thermoresponsive Polymer Micropatterns Fabricated by Dip-Pen Nanolithography”, S. Laing,* R. Suriano,* D.A. Lamprou, S. Mabbott, M. Levi, S. Turri, K. Faulds, D. Graham. (in preparation)